

**MICROMACHINED TUNABLE VCSELS FOR
WAVELENGTH DIVISION MULTIPLEXING
SYSTEMS**

A DISSERTATION

SUBMITTED TO THE DEPARTMENT OF

ELECTRICAL ENGINEERING

AND THE COMMITTEE ON GRADUATE STUDIES

OF STANFORD UNIVERSITY

IN PARTIAL FULFILLMENT OF THE REQUIREMENTS

FOR THE DEGREE OF

DOCTOR OF PHILOSOPHY

Wayne Alan Martin

June 2001

© Copyright by Wayne Alan Martin 2001
All Rights Reserved

I certify that I have read this dissertation and that in my opinion it is fully adequate, in scope and quality, as a dissertation for the degree of Doctor of Philosophy.

James S. Harris, Jr. (Principal Advisor)

I certify that I have read this dissertation and that in my opinion it is fully adequate, in scope and quality, as a dissertation for the degree of Doctor of Philosophy.

David A. B. Miller

I certify that I have read this dissertation and that in my opinion it is fully adequate, in scope and quality, as a dissertation for the degree of Doctor of Philosophy.

Tom H. Lee

Approved for the University Committee on Graduate Studies:

Abstract

Continued exponential increases in the computer usage and processing power have caused phenomenal growth in data traffic over the last five years and current networks are struggling to keep up with the demand. Optical Wavelength Division Multiplexing technology is now being deployed to exploit the enormous bandwidth potential of optical fiber, but the cost and power requirements for WDM systems are high. Micromachined Tunable VCSELs (MTVCSELs) can reduce both the cost and power needed to implement WDM systems. The MTVCSSEL uses an electrostatically controlled membrane for tuning. This tuning method requires much less power than temperature tuning methods. Tunable devices reduce the cost of system redundancy by allowing one tunable device to replace an entire rack of fixed wavelength backup lasers. Additionally, VCSELs emit a circular beam that is easier to couple into fibers than the highly elliptical beam produced by edge-emitting lasers.

One of the key challenges facing WDM systems is controlling the wavelength of the lasers in the system. Arrayed Waveguide Gratings (AWGs) have been demonstrated with 256 channels in a single device, 25 GHz channel spacings and 30 dB of isolation. Since AWGs are fabricated in a bulk semiconductor process it is easy to produce many devices of the same design with closely matched characteristics. This makes them the ideal device

to serve as a channel standard in WDM systems. Each laser must be tuned to transmit on a different channel of the AWG to prevent crosstalk. This work demonstrates a novel method of wavelength control using an MTVCSSEL that can be used with any wavelength selective element such as an AWG.

In this work, MTVCSSELS have been fabricated and improvements to the fabrication process have been demonstrated. Additionally, frequency locking by dithering the output of the MTVCSSEL has been demonstrated and shown to track changes in the center wavelength of a channel up to 11 nm. The frequency locking system can compensate for differences and drift in the MTVCSSEL characteristics and also select different channels as needed in wavelength routing systems. The linewidth and stability of transmitting laser is also important for reliable communications. The linewidth of the MTVCSSEL has been measured to be 2 GHz with excellent short-term stability.

Acknowledgments

Research into a device as complicated as the Micromachined Tunable VCSEL can not be accomplished without the efforts of many people. I am forever indebted to Professor Harris for the research environment he has provided his students with. He has allowed me the freedom to pursue my own interests and provided the infrastructure needed to support them. He has helped me with both the technical challenges I faced and with my personal struggles to complete the research. Thanks Coach.

I am very thankful that Professor Antony Fraser-Smith was willing to serve as my orals chairman and that he was available during the limited time available to get the exam scheduled before graduation. He also provided valuable advice about how to improve my oral defense presentation.

I appreciate Professor David Miller serving as my associate advisor, on my orals committee and reading my dissertation. He has also advised me about how to pursue my research efforts and has shared his detailed knowledge of optoelectronic devices in many fruitful discussions.

I am lucky and grateful that Professor Glenn Solomon was available to fill in as my fourth orals committee member. As a former MBE guru he has worked long hours to

maintain our MBE efforts and is still willing to lend his knowledge and hands when needed in the lab.

Professor Tom Lee served as my third reader and has shared his love and knowledge of analog RF electronics with me. I have really enjoyed your teaching and the conversations we have had about electronics and the joys of experimenting.

Of course none of this could have been accomplished without the idea that Bardia Pezeshki had for developing a Micromachined Tunable VCSEL and the pioneering efforts of Michael Larson and Fred Sugihwo in developing the fabrication technology needed to realize the dream of a widely, continuously tunable semiconductor laser.

Chien-chung Lin has been my partner in the MBE growth and the device processing efforts of Micromachined Tunable VCSEL fabrication. He has worked tirelessly to maintain MBE system I and organized the move of our MBE lab into the new CISX building. He has grown many wafers for me and helped with the development of our micromachining process. I wish him the best of luck with his further efforts on micromachining of tunable vertical cavity devices.

Gail Chun-Creech has helped all of us in the Harris Group many times over the years. I especially appreciate her calm efforts during the last minute stresses of proposal deadlines. She has also been willing to lend an ear when I have had a bad day in cleanroom. Your kind cheerful words and efforts are greatly appreciated.

I need to thank the many current and former members of the Harris Group. Chris Col-dren, Chris Ebert and Sylvia Spruytte have done an excellent job of maintaining the rest of the MBE lab and sharing their knowledge of crystal growth. Vijit Sabnis helped me rebuild and get control of the AlAs oxidation system that would not have been available without the prior work of Alan Massengale. Barbara Paldus moved the optics lab and helped me build the electronics needed for the MBEs. Ken Bacher was the former MBE computer Guru who computerized systems 1 and 2 and gave me helpful advice as I tried to fulfil that role in the new lab.

Some members of the CIS cleanroom staff have done an outstanding job of maintaining the facility and helping me with processing equipment. Len Booth has done an amazing job of being in charge of all of the plasma-etching equipment in the lab. Elaheh Sigari, Chris Storment, and Tony Flannery helped with PECVD questions and guided me in my cleanroom efforts. Professor James McVittie has been available to answer my many questions about plasma processing.

Kevin Yu and Joe Little helped me many times with Solaris questions. Joe put in an incredible effort rebuilding the CIS computer networks. Members of the Kovacs and Lee Research groups helped me with several semiconductor processing and analog design questions.

I would have had much less fun at Stanford without the company of many friends, including, Robert and Lisa Johnson, Brian and Kelly Armstrong, Sameer and Deepali Halepete, Esin and Janis Terzioglu, Derrick and Debbie Shaeffer, Martin and Ivana Gander, Jarek Baryeka, Michael Drexler, Scott and Shana Ballard, Thorsten Hesjedal and Tonia Stengelin, Matt and Jill Rogge, and Tamara Ahrens.

I would never have gone this far without the inspiration of my parents who provided an educational environment from an early age and supported my sometimes expensive learning efforts. Finally I am very thankful for the patience and support of my wife Kristen who finally gets to start her MBA this fall.

The work for this dissertation was funded by the Advanced Research Project Agency through the Optical Materials Center under contract #MDA972-98-1-0002, and the Air Force Office of Scientific Research under contract #F49620-1-0021. I also received a National Science Foundation Fellowship to help with the costs of graduate education.

Table of Contents

Abstract	v
Acknowledgments	vii
List of Figures	xv
Chapter 1 Introduction	1
1.1 Wavelength Division Multiplexing	1
1.2 Micromachined Tunable VCSELs	4
1.3 Wavelength Control	5
1.4 Outline	5
Chapter 2 Semiconductor Lasers: modeling and materials	7
2.1 Optical resonators	7
2.1.1 General Fabry-Perot etalon equations	8
2.1.2 Round trip gain and laser threshold	10
2.2 Semiconductor laser materials	12
2.2.1 Semiconductor bandgap	12
2.2.2 Photon absorption and emission in semiconductors	15
2.2.2.1 Absorption	15
2.2.2.2 Stimulated Emission	17
2.2.2.3 Optical Gain	17
2.2.2.4 Spontaneous emission	19
2.2.3 Other recombination processes in semiconductors	20

2.2.4	Refractive Index.....	20
2.2.4.1	Al _x Ga _{1-x} As	21
2.2.4.2	In _x Ga _{1-x} As.....	21
2.3	Semiconductor laser rate equations	22
2.4	Current, Voltage and Output Power of semiconductor lasers	25
2.5	Types of semiconductor lasers	27
2.6	Distributed Bragg Reflectors and thin film modeling of lasers	29
Chapter 3	Micromachined Membranes and VCSEL Tuning	39
3.1	Membrane displacement	40
3.1.1	Electrostatic and Elastic Forces	41
3.1.2	Effective Spring Constant	44
3.1.3	Rigid central region with thin flexible legs under tension.....	44
3.2	Membrane tuning of VCSELs	46
3.2.1	Tuning rate analysis	47
3.2.2	Tuning Range.....	52
Chapter 4	Fabrication of MTVCSLEs	55
4.1	Fabrication Procedure	56
4.1.1	Step 1: MBE Growth	56
4.1.2	Step 2: PECVD of top mirror and backside AR coating	57
4.1.3	Step 3: Current confinement etch and oxidation.....	57
4.1.4	Step 4: Backside N ⁺ Ohmic Contact	59
4.1.5	Step 5: Membrane Center Etching.....	59
4.1.6	Step 6: Membrane Adhesion and Top Mirror Layer Deposition	61
4.1.7	Step 7: Membrane Etch.....	63
4.1.8	Step 8: Membrane Post Recess Etch.....	64
4.1.9	Step 9: Cavity P ⁺ Ohmic Contact.....	65
4.1.10	Step 10: Membrane Release.....	66
4.2	Process Development.....	69
4.2.1	Oxidation of AlGaAs layers	69
4.2.1.1	Oxidation System.....	70
4.2.1.2	Oxidation Rate	74
4.2.2	Stress control in PECVD Silicon Nitride and Silicon Dioxide.....	78
4.2.2.1	Silicon Nitride.....	79
4.2.2.2	Silicon Dioxide	81

Chapter 5	Micromachined Tunable VCSELs	83
5.1	Design	83
5.1.1	Aperture	83
5.1.2	Optical and Epitaxial Layers.....	86
5.2	Results.....	89
5.2.1	Output Power, Voltage, Current.....	89
5.2.2	Tuning	90
5.2.3	Linewidth.....	94
Chapter 6	Frequency Locked Loops for WDM systems	99
6.1	FLL Concept.....	99
6.2	Linear FLL.....	101
6.2.1	Design	101
6.2.2	Simulation.....	102
6.3	Nonlinear FLL	106
6.3.1	Design	106
6.3.2	Simulation.....	107
6.3.3	Quantitative Feedback Theory.....	111
6.4	Results.....	115
Chapter 7	Summary and Future Work	119
7.1	Summary.....	119
7.2	Future Work	120
7.2.1	Membrane Design.....	120
7.2.2	Alternative Wavelengths.....	121
7.2.3	Systems Demonstrations.....	121
7.2.4	Reliability.....	121
Bibliography		123

List of Figures

Figure 1.1:	Progress in the Bandwidth of a Single Communications Link [3].	2
Figure 1.2:	WDM Point to Point interconnection.	3
Figure 2.1:	Schematic of a Fabry-Perot etalon.....	8
Figure 2.2:	Circulating (Top), Reflected (Middle), and Transmitted (Bottom) intensity for a Fabry-Perot etalon, $R_1=R_2=R$	11
Figure 2.3:	Electronic energy vs. momentum diagram for a direct bandgap semiconductor showing a transition from valence band (E1) to conduction band (E2). The lowest energy state in the conduction band is E_c and valence band is E_v	14
Figure 2.4:	Radiative electronic transitions between the conduction and the valence bands of a semiconductor [23]. Absorption (Left), Stimulated Emission (Center), Spontaneous Emission (Right).	15
Figure 2.5:	Calculated TE gain spectrum vs. carrier density in $\text{In}_{0.2}\text{Ga}_{0.8}\text{As}/\text{GaAs}$ 80\AA QW. Indicated values are the sheet carrier densities: $\times 10^{12}\text{cm}^{-2}$ [23].....	18
Figure 2.6:	Output power (Left) and diode voltage (Right) vs. current for a typical diode laser.	26
Figure 2.7:	Schematic representation of an edge-emitting laser. The corresponding coordinate system is also shown.	27
Figure 2.8:	Schematic diagram of a VCSEL showing various epitaxial layers. .	28
Figure 2.9:	Schematic diagram of a normal plane wave incidence on a plane dielectric boundary [32].....	30

Figure 2.10:	Reflections in a thin film.	31
Figure 2.11:	Plot of mirror reflectance and phase versus wavelength for 20 pairs of alternating AlAs/GaAs DBR centered near 970nm. The dotted line shows the corresponding phase.....	36
Figure 2.12:	Schematic of a DBR mirror and an ideal mirror at the phase depth approximating the DBR mirror.	36
Figure 3.1:	Cavity axial modes shown as arrows and the optical gain of quantum wells shown as a curve for Edge-Emitters and VCSELs.....	40
Figure 3.2:	Side view of electrostatic membrane displacement.	41
Figure 3.3:	Elastic restoring force (dashed lines) and electrostatic force (solid curves) for four different applied biases as a function of membrane displacement.	43
Figure 3.4:	Free body diagram of membrane.	45
Figure 3.5:	Schematic showing transformation from a fixed wavelength VCSEL to a wavelength tunable VCSEL.....	46
Figure 3.6:	The three cavity configurations for micromachined wavelength tunable VCSELs showing the air gap and the semiconductor cavity thickness: (a) Air coupled cavity (ACC), (b) Extended cavity (EC), (c) Semiconductor coupled cavity (SCC), and (d) conventional VCSEL.	47
Figure 3.7:	Resonant wavelength vs. air gap thickness variation near center wavelength for ACC, SCC, and EC cavity configurations. The center wavelength air gap thickness for ACC and EC is l and for SCC is $3l/4$ [8].....	50
Figure 3.8:	Threshold material gain vs. wavelength for ACC, SCC, and EC cavity configurations [8].....	51
Figure 3.9:	Resonant wavelength vs. air gap thickness. Shown on dotted lines are the resulting wavelength tuning range for different starting air gap thickness [8].....	52
Figure 4.1:	Schematic drawing of the MTVCSEL.....	56
Figure 4.2:	MTVCSEL after current mask etching.....	58
Figure 4.3:	MTVCSEL current aperture.	58
Figure 4.4:	MTVCSEL after center mask etching.	60
Figure 4.5:	MTVCSEL after membrane adhesion layer deposition.....	62
Figure 4.6:	MTVCSEL after top mirror layer deposition.	62
Figure 4.7:	MTVCSEL after membrane etch.....	64
Figure 4.8:	MTVCSEL after cavity contact.	66
Figure 4.9:	MTVCSEL before release etch.....	67

Figure 4.10:	Schematic of a tunable VCSEL with thicker central reflector and thinner membrane legs.	67
Figure 4.11:	SEM image of a tunable VCSEL.	68
Figure 4.12:	MTVCSEL after cavity contact.	68
Figure 4.13:	Schematic drawing of a typical AlGaAs oxidation furnace.	70
Figure 4.14:	Furnace temperature versus position.	71
Figure 4.15:	Oxidation distance versus carrier gas flow rate.	72
Figure 4.16:	Oxidized Samples of AlGaAs, Diffusion Limited (Left), Reaction Limited (Right).	73
Figure 4.17:	Oxidation rate for a 500 nm layer of Al _{0.97} Ga _{0.03} As at 440oC.	75
Figure 4.18:	Activation energy versus layer thickness.	76
Figure 4.19:	Reaction rate coefficient versus layer thickness.	76
Figure 4.20:	Oxidation rate in Al _{0.97} Ga _{0.03} As.	77
Figure 4.21:	Growth regions in PECVD Silicon Nitride [68].	80
Figure 5.1:	Aperture at a node in the standing wave pattern [76].	84
Figure 5.2:	Aperture at an antinode in the standing wave pattern [76].	84
Figure 5.3:	Difference in threshold gain between the fundamental mode and the next higher order mode for a 5 mm in diameter aperture [76].	85
Figure 5.4:	Threshold gain for an oxide aperture at a node [76].	86
Figure 5.5:	Optical layers in the MTVCEL.	87
Figure 5.6:	Standing wave simulation of the MTVCEL.	89
Figure 5.7:	L I V data for MTVCEL.	90
Figure 5.8:	Optical Spectra of the MTVCEL at different membrane biases. ...	91
Figure 5.9:	Lasing wavelength versus membrane bias.	92
Figure 5.10:	Side Mode Suppression Ratio.	93
Figure 5.11:	Wavelength tuning versus time [7].	94
Figure 5.12:	Lasing linewidth.	95
Figure 5.13:	Linewidth and Wavelength stability.	95
Figure 5.14:	Linewidth versus output power.	96
Figure 6.1:	FLL Concept.	100
Figure 6.2:	Linear FLL.	102
Figure 6.3:	Linear FLL, Vc	103
Figure 6.4:	Linear FLL, Wavelength.	103
Figure 6.5:	Linear FLL, Power.	104
Figure 6.6:	Linear FLL, Vc, gain ³ 10.	105

Figure 6.7:	Linear FLL, Vc, gain ¥ 5.	105
Figure 6.8:	Linear FLL, Vc, gain ¥ 10.	106
Figure 6.9:	Adaptive Gain Nonlinear FLL.	107
Figure 6.10:	Nonlinear FLL, Vc.	108
Figure 6.11:	Nonlinear FLL, Wavelength.	108
Figure 6.12:	Nonlinear FLL, Power.	109
Figure 6.13:	Nonlinear FLL, Vc, gain ³ 100.	109
Figure 6.14:	Nonlinear FLL, Power, gain ³ 100.	110
Figure 6.15:	Nonlinear FLL, Vc, gain ¥ 100.	110
Figure 6.16:	Nonlinear FLL, Power, gain ¥ 100.	111
Figure 6.17:	Nonlinear FLL gain blocks.	112
Figure 6.18:	QFT for the nonlinear FLL.	114
Figure 6.19:	Schematic of FLL measurement setup.	116
Figure 6.20:	Measured Vc of FLL for different wavelength settings.	117

Chapter
1

Introduction

This thesis covers my work in developing improved process flows for the Micromachined Tunable VCSELs (MTVCSELs), characterization of the resulting devices for their use in Wavelength Division Multiplexing (WDM) systems, and frequency locking them to external wavelength references. After developing a high yield process flow for device fabrication, several measurements of laser performance were carried out and a technique was developed for controlling the wavelength of the tunable lasers.

1.1 Wavelength Division Multiplexing

Advances in technology can often be described by an S-curve, slow initial growth followed by exponential improvements and eventual saturation when some limit is reached. The progress of technology in computing power as predicted by Moore's [1] Law is unprecedented in history, doubling every 18 months starting in 1959 and is predicted to continue till around 2010 to 2015 [2]. Since about 1990 the bandwidth of a single optical fiber communications link as shown in Figure 1.1 has been doubling every 16 months [3] and the cross-sectional backbone capacity of the national fiber optical network is tripling every 12 months [4].

One of the main driving forces behind Moore's Law is the scaling of transistor sizes. Every new generation of CMOS requires fewer electrons per bit of information than the last. Information is carried by photons in optical communications systems. The size of a photon is defined by its wavelength that is usually chosen to match the loss minimum in silica fibers at 1.5 μm . Therefore wavelength does not scale and the only way to get more

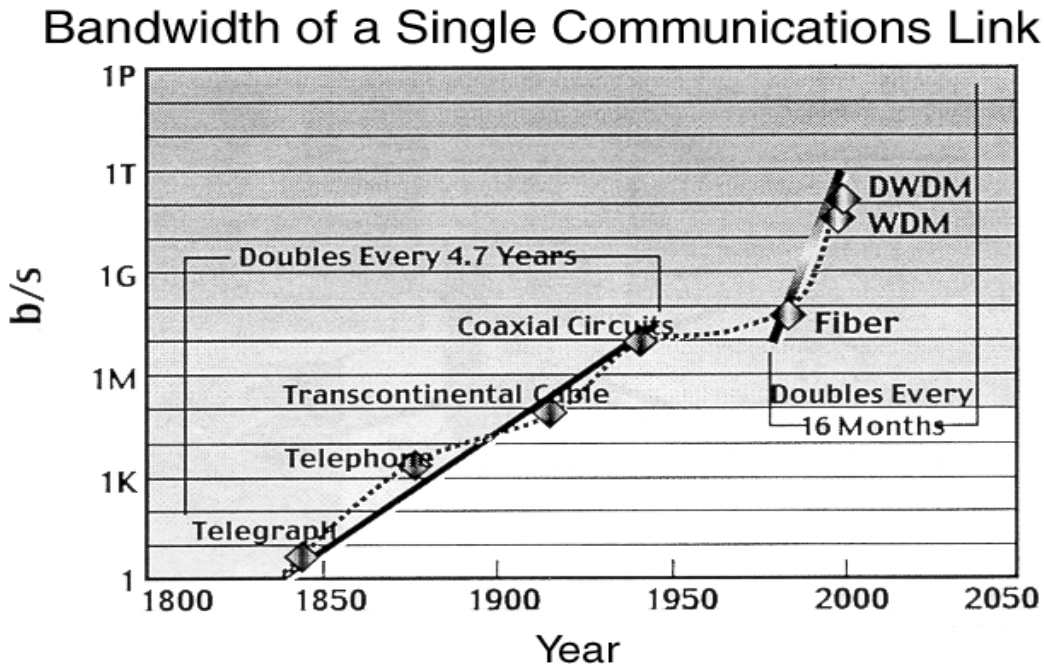


Figure 1.1: Progress in the Bandwidth of a Single Communications Link [3].

information down a given cross-sectional area of fiber is to send more photons and more information on each photon.

More photons can be sent by increasing the increasing the transmitted power of a given channel which allows for higher modulation rates or by adding more channels at different wavelengths. Electronic limitations in the design of lasers, modulators and photodiodes make it difficult and expensive to operate a single channel above a few tens of GHz [5]. Since the low loss transmission window of silica fiber is tens of THz wide [6], WDM can greatly increase the information carried per fiber. The same electronic speed limitations that make it expensive to operate a channel above a few tens of GHz also make it hard to build the signal processing systems needed to encode more information on each photon. So WDM is presently the best way to increase fiber capacity.

An example system for a point to point WDM interconnection is shown in Figure 1.2. Lasers operating at different wavelengths are combined into one optical fiber using an Arrayed Waveguide Grating (AWG) which has a channel for each laser. After traversing

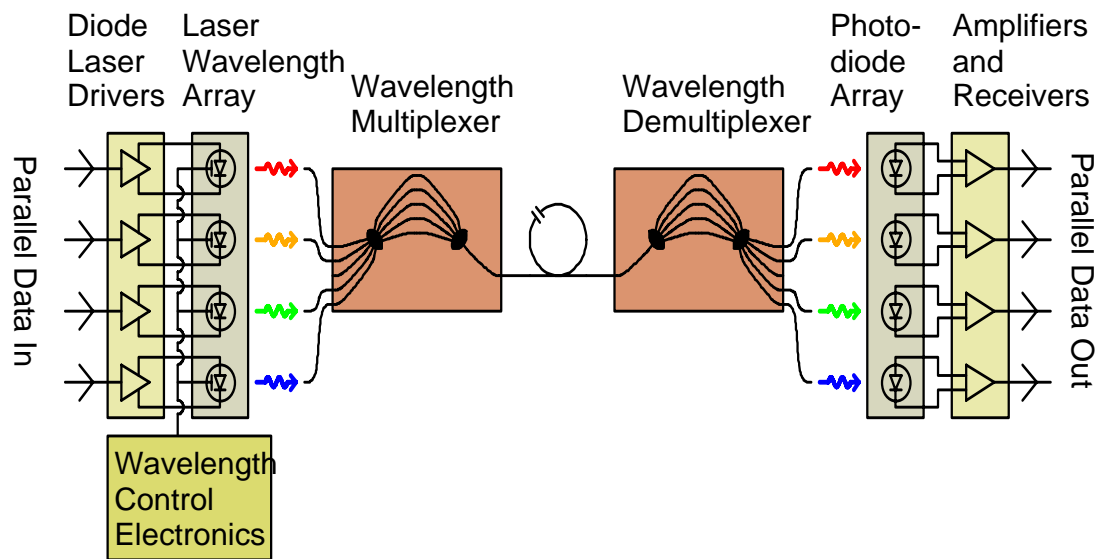


Figure 1.2: WDM Point to Point interconnection.

the fiber the channels are separated by a second AWG and detected with photodiodes. Since optical radiation at different wavelengths does not interact significantly in linear optical media such as silica fibers, crosstalk is not a problem. In such a system it is important to insure that the wavelength of each laser stays within the range allowed by the channel spacing in the AWG or both crosstalk and attenuation will occur.

Presently the wavelength of lasers in WDM systems is controlled by thermally tuning the bandgap of the quantum wells. This has several disadvantages including: slow tuning rates < 1 kHz, large power consumption in the thermoelectric cooler, and a limited tuning range, typically a few nanometers. The worst from a cost point of view may be the limited tuning range. If system redundancy is required an entire additional set of lasers is needed to provide backups. The inability to integrate the lasers caused by the thermal requirements and impossibility of doing wavelength routing caused by the limited tuning range and slow tuning rate are also significant barriers to building WDM networks.

1.2 Micromachined Tunable VCSELs

This work focuses on the MTVCSEL which provides a solution to all of these problems by offering a wide tuning range (tens of nanometers), a high tuning rate (> 1 MHz), and a low power electrostatic tuning method [7][8]. They are based on the Vertical Cavity Surface Emitting Laser (VCSEL) structure which has a number of advantages over edge-emitting devices, particularly for tunable lasers. Since VCSELs are very short they have only one axial mode within the gain bandwidth of the quantum wells. A short tunable laser does not require the complicated and hard to fabricate intracavity structures needed for mode control in an edge-emitter to enable a wide wavelength tuning range[9]. Wavelength tuning in an MTVCSEL is inherently a continuous process, whereas non-thermally tunable edge-emitting devices such as those with Sampled Grating Distributed Bragg Reflectors (SGDBRs) have regions of mode hopping even when great efforts are taken to control their behavior [10]. VCSELs emit a circular beam which is easier to couple into fibers than the highly elliptical beam from edge-emitters. Yield, ease of fabrication and integration are better in VCSELs because light is emitted perpendicular to the wafer surface which enables on wafer probing, eliminates the difficult yield-killing cleaving step needed for edge-emitter fabrication and allows for flip-chip bonding into optical systems. Density and efficiency can be high in VCSEL devices because both the active area and the entire structure is smaller than for edge-emitters [11][12].

MTVCSELs use a top mirror fabricated from a hybrid materials system suspended above an air gap on a deformable micromachined membrane. The position of the membrane is electrostatically actuated, which changes the effective cavity length and wavelength of laser emission. The membrane can be pulled down approximately $1/3$ of the original air gap thickness which allows the wavelength to be varied over 25 nm [8].

1.3 Wavelength Control

Control of the lasing wavelength is needed to prevent crosstalk in WDM systems. The control system must be robust against environmental and system induced variations. Since athermal AWGs have been demonstrated with a 0.05 nm wavelength variation over the 0 to 85° C temperature range [13] they can serve as effective channel standards. A frequency locked loop (FLL) can stabilize the MTVCSSEL by keeping it tuned to the transmission peak of a channel in the AWG.

1.4 Outline

This thesis covers my work on fabricating the MTVCSSEL structures, characterization of the devices as needed for WDM systems and development of a technique for controlling the lasing wavelength. Chapter 2 gives the background laser fundamentals needed for designing MTVCSSELS including semiconductor rate equations and numerical modeling of thin film structures. Wavelength tunability is discussed in Chapter 3 and issues of tuning range as a function of cavity design are presented. The exacting fabrication process is reviewed in Chapter 4. The work includes some new measurements of oxidation rates in 97% Al AlGaAs and the development of stress controlled recipes for Silicon Dioxide and Silicon Nitride in an STS dual frequency PECVD system. After fabricating the devices they are characterized in Chapter 5. In Chapter 6, the novel application of a frequency locked loop to provide wavelength control in these devices is discussed and measurements of frequency locking and tracking are presented. Chapter 7 concludes by summarizing the work and offers suggestions for future research efforts.

Chapter
2

Semiconductor Lasers: modeling and materials

The basic concepts of laser oscillation are covered in this chapter. First, we present the fundamental equations for optical resonators and show how gain can be used to achieve oscillation. Next, will we discuss gain and recombination processes in semiconductor materials and review the equations needed to analyze semiconductor lasers. Then the basic types of semiconductor lasers, edge-emitter and vertical-cavity are reviewed. Finally, the mathematical formalism needed to model thin-film multilayer structures such as Distributed Bragg Reflector mirrors (DBRs) and VCSELs is presented and methods of improving the calculation speed are suggested.

2.1 Optical resonators

The laser is a light oscillator and as such it needs gain and feedback. Optical gain will be covered in section 2.2.2 and feedback is covered here. The required optical feedback is provided by a resonator. The simplest type of optical resonator is a pair of parallel mirrors first described by Fabry and Perot in 1899 [14] and known as the Fabry-Perot etalon. A side view of a typical etalon is shown in Figure 2.1 with a pair of thin mirrors represented by the crosshatched regions and the electrical field vectors drawn for illustration. The space between the mirrors is the cavity of the Fabry-Perot device and can be filled with air, a dielectric, or in the case of a laser an optical gain producing media.

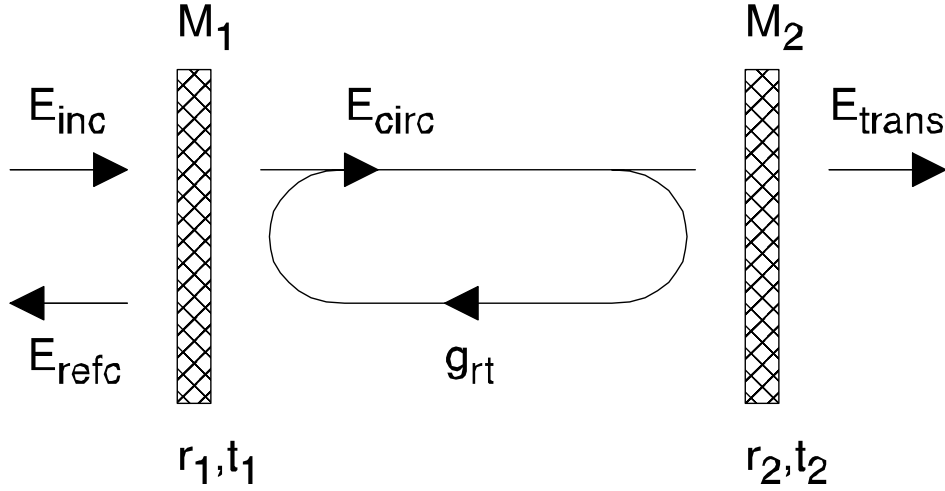


Figure 2.1: Schematic of a Fabry-Perot etalon.

2.1.1 General Fabry-Perot etalon equations

The optical characteristics of the Fabry-Perot etalon will be analyzed assuming a plane wave approximation [15]. In Figure 2.1 E_{inc} is the incoming electric field, E_{refc} is the reflected field, E_{trans} is the transmitted field and E_{circ} is the field inside the cavity. The electric field is represented in phasor notation by

$$E(z, t) = \text{Re} \left\{ \frac{E}{\sqrt{n}} \exp[j(\omega t - \beta z)] \right\} \quad (2.1)$$

where E is the phasor amplitude of the plane wave, n is the refractive index of the media, and β is the propagation constant given by $\beta = \omega n/c$ where c is the speed of light in vacuum. The electric field has been normalized to represent the square root of optical power which allows a mirror to be characterized by its amplitude reflection coefficient or reflectivity r , which is the ratio between the amplitude of the reflected wave and the incident wave and by a transmission coefficient or transmissivity t , which is the ratio between the amplitude of the transmitted wave and the incident wave. This normalization also allows direct comparisons of the optical power in the wave.

In the Fabry-Perot etalon from Figure 2.1 the round trip gain in the cavity is

$$g_{rt}(\omega) = r_1 r_2 \times \exp\left[\left[(g - \alpha_0)L\right] - j2\omega \frac{nL}{c}\right] \quad (2.2)$$

where r_1 and r_2 represent the reflectivities of mirror 1 and 2, α_0 is the optical intensity loss, g is the optical intensity gain and n is the refractive index of the cavity media. Note that g and α_0 represent a power loss which has twice the value of that for an amplitude loss. Since it is customary to quote loss and gain in intensity units we will use that convention. In semiconductors the values of g and α_0 depend on the frequency of the optical field ω and can also depend on the intensity of the field as well as external influences as will be discussed in section 2.2.2. The reflected, transmitted and circulating fields can then be related to the incident field by

$$\frac{E_{\text{refl}}}{E_{\text{inc}}} = \frac{1}{r_1} \times \frac{r_1^2 - g_{rt}(\omega)}{1 - g_{rt}(\omega)} \quad (2.3)$$

$$\frac{E_{\text{trans}}}{E_{\text{inc}}} = -\frac{t_1 t_2}{\sqrt{r_1 r_2}} \times \frac{\sqrt{g_{rt}(\omega)}}{1 - g_{rt}(\omega)} \quad (2.4)$$

$$\frac{E_{\text{circ}}}{E_{\text{inc}}} = \frac{jt_1}{1 - g_{rt}(\omega)} \quad (2.5)$$

where t_1 and t_2 are the transmissivities of mirror 1 and 2. Taking the square of the absolute values of those equations gives the intensity ratios

$$\frac{I_{\text{refl}}}{I_{\text{inc}}} = \left| \frac{E_{\text{refl}}}{E_{\text{inc}}} \right|^2 = \frac{R_1 + R_2' - 2\sqrt{R_1 R_2'} \cos \phi_{rt}}{1 + R_1 R_2' - 2\sqrt{R_1 R_2'} \cos \phi_{rt}} \quad (2.6)$$

$$\frac{I_{\text{trans}}}{I_{\text{inc}}} = \left| \frac{E_{\text{trans}}}{E_{\text{inc}}} \right|^2 = \frac{T_1 T_2 \exp(-\alpha_0 L)}{1 + R_1 R_2' - 2\sqrt{R_1 R_2'} \cos \phi_{rt}} \quad (2.7)$$

$$\frac{I_{\text{circ}}}{I_{\text{inc}}} = \left| \frac{E_{\text{circ}}}{E_{\text{inc}}} \right|^2 = \frac{T_1}{1 + R_1 R_2' - 2\sqrt{R_1 R_2'} \cos \phi_{rt}} \quad (2.8)$$

where $\phi_{rt} = 2\omega nL/c$ and $R'_2 = R_2 \exp(-2(g - \alpha_o)L)$. In Figure 2.2 we plot the reflected, transmitted and circulating intensities versus frequency for mirror reflectances $R_1=R_2=0.3, 0.9$ and 0.99 in a cavity with no gain or loss.

A resonant mode can be clearly seen in Figure 2.2 and is caused by the $1 - g_{rt}(\omega)$ term in the denominator of all of the equations. The denominator has a minimum when the round trip phase is a multiple of 2π . The physical cause of the minimum is that the circulating wave constructively interferes with itself and generates resonant enhancement of its amplitude. This also creates the transmission peak and reflectivity minima. The spacing between resonances is called the axial mode spacing and is given by

$$\Delta\omega_{ax} \equiv \omega_{q+1} - \omega_q = \frac{\pi c}{nL} . \quad (2.9)$$

In a typical edge-emitter $L=200 \mu\text{m}$ long with $n=3$, the axial mode spacing is $\Delta f_{ax}=500$ GHz, in a typical VCSEL, L is approximately $2 \mu\text{m}$ and $\Delta f_{ax}=2.5$ THz. The larger spacing between axial modes allows the VCSEL to be tuned over a larger range.

2.1.2 Round trip gain and laser threshold

All of the Fabry-Perot equations have a factor of $1-g_{rt}$ in the denominator. If the value of gain in the g_{rt} is increased the difference $1-g_{rt}$ decreases causing the peaks in the reflected, transmitted and circulating power over incident power curves to narrow. When $1-g_{rt}$ reaches zero the peaks diverge indicating that lasing has started. Setting $g_{rt}=1$ gives

$$g_{rt}(\omega) = r_1 r_2 \times \exp\left[-(\alpha_0 - g(\omega))L - j2\omega \frac{nL}{c}\right] = 1 \quad (2.10)$$

as the condition for laser threshold. Since the g_{rt} term is complex the equation can be split into 2 parts. A gain equation from the real terms

$$r_1 r_2 \times \exp[-(\alpha_0 - g(\omega))L] = 1 \quad (2.11)$$

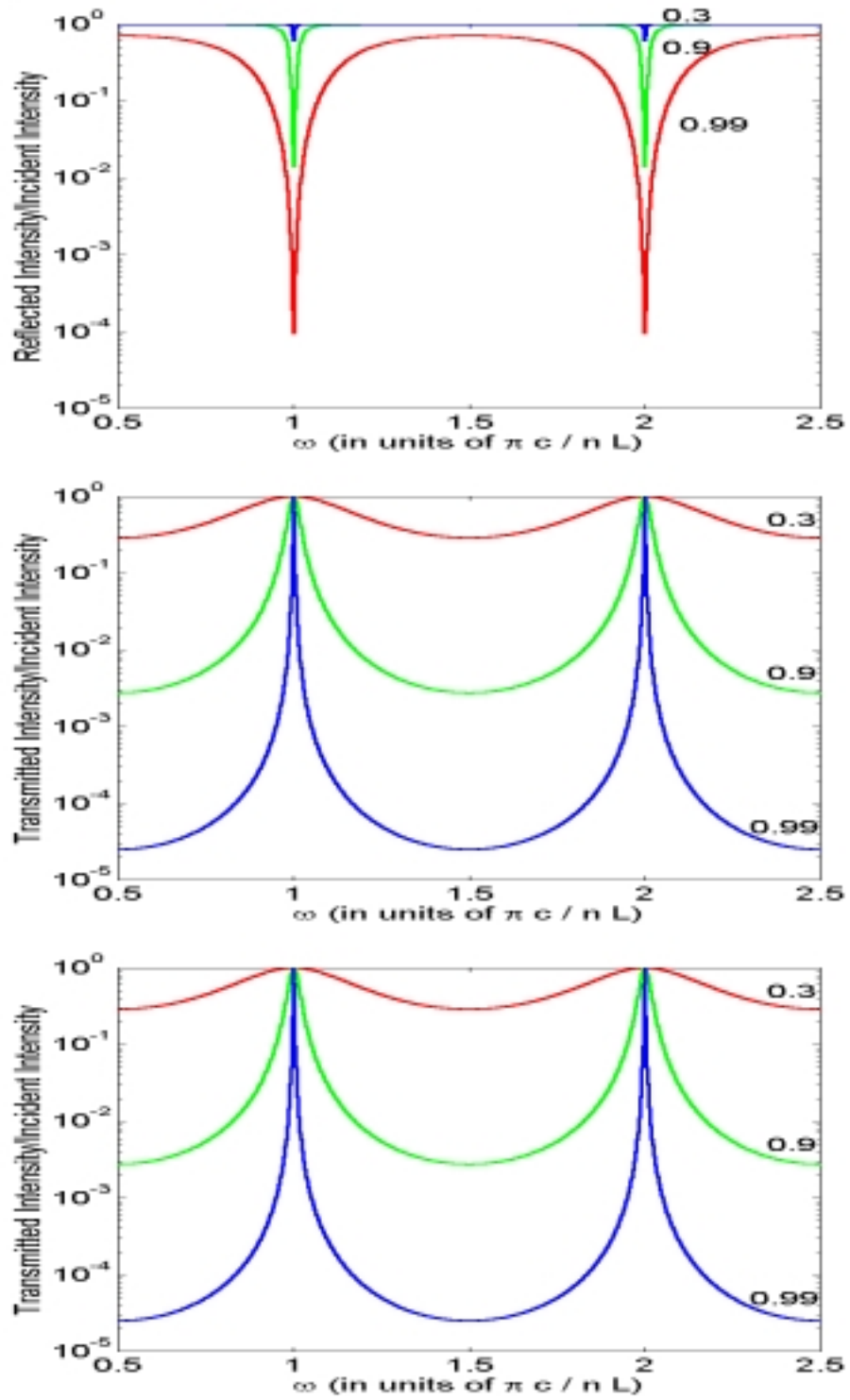


Figure 2.2: Circulating (Top), Reflected (Middle), and Transmitted (Bottom) intensity for a Fabry-Perot etalon, $R_1=R_2=R$.

which is usually represented as

$$\Gamma g = \alpha_0 + \left(\frac{1}{2L}\right) \ln\left(\frac{1}{R_1 R_2}\right) \quad (2.12)$$

where Γ is a structure dependant constant needed to account optical confinement.

And a phase equation from the complex terms

$$\exp\left[-j2\omega\frac{nL}{c}\right] = 0 \quad (2.13)$$

which can be simplified to

$$2\omega\frac{nL}{c} = q2\pi \quad (2.14)$$

where q is any integer. These are the two conditions that need to be fulfilled to produce a light oscillator or laser.

2.2 Semiconductor laser materials

Now that we have derived the equations for basic laser operations it is time to consider what kinds of materials are needed to build semiconductor laser. The optical properties and generation of optical gain in semiconductor materials are discussed and the basic semiconductor laser equations are presented.

2.2.1 Semiconductor bandgap

A semiconductor is a material whose electrical conductivity can be controlled over several orders of magnitude by adding small amounts of an appropriate doping material. They typically have an electronic bandgap between the highest occupied level and the first excited states of approximately 1 eV. The bandgap is large enough to prevent conductivity of the pure material at room temperature, but small enough to allow conductivity in a suitably doped sample. The existence of a bandgap produces many phenomena important for semiconductor devices. The ones we consider here are the optical properties of the band-

gap. Since there are no electronic states within a bandgap there will be no absorption of photons that have an energy less than the bandgap. Additionally, when excited carriers recombine they can release photons with approximately the same energy as the bandgap.

In order to have efficient generation of photons from the recombination of excited carriers the semiconductor must have a direct bandgap. Having a direct bandgap means that the minimum energy in the conduction band occurs at the zero momentum point. The valence band maximum is always occurs at the zero momentum point, but the location of the conduction band minimum depends on the material. Since the photon is a massless particle with very little momentum on the scale of that involved in semiconductor band energy versus momentum characteristics and the total momentum must be conserved in any carrier process, only carriers with approximately equal momentums near the band edge of a direct gap semiconductor have a high probability of radiatively recombining. Silicon cannot be used to provide optical gain because it does not have a direct bandgap. We use alloys of $\text{Al}_x\text{Ga}_{1-x}\text{As}$ and $\text{In}_x\text{Ga}_{1-x}\text{As}$ in the fabrication of the MTVCSEL laser devices because they have a direct bandgap in the wavelength range where optical gain is needed and because they are relatively easy to grow using a mature growth technology. A schematic picture of the bandgap energy versus carrier momentum in a direct gap semiconductor is shown in Figure 2.3.

The bandgap of $\text{Al}_x\text{Ga}_{1-x}\text{As}$ is given by

$$E_g(x) = 1.424 + 1.155x + 0.37x^2 \quad \text{for} \quad x < 0.45 \quad (2.15)$$

where the material has a direct bandgap [16]. Above an Al content of 0.45 the bandgap becomes indirect and is given by

$$E_g(x) = 1.9 + 0.125x + 0.143x^2 \quad \text{for} \quad x > 0.45. \quad (2.16)$$

The bandgap of bulk $\text{In}_x\text{Ga}_{1-x}\text{As}$ is given by

$$E_g(x) = 0.324 + 0.7(1 - x) + 0.4(1 - x)^2 \quad (2.17)$$

for bulk material [18]. The lattice constant of $\text{In}_x\text{Ga}_{1-x}\text{As}$ is different than that of $\text{Al}_x\text{Ga}_{1-x}\text{As}$ and varies with In content. The growth $\text{In}_x\text{Ga}_{1-x}\text{As}$ on a GaAs substrate

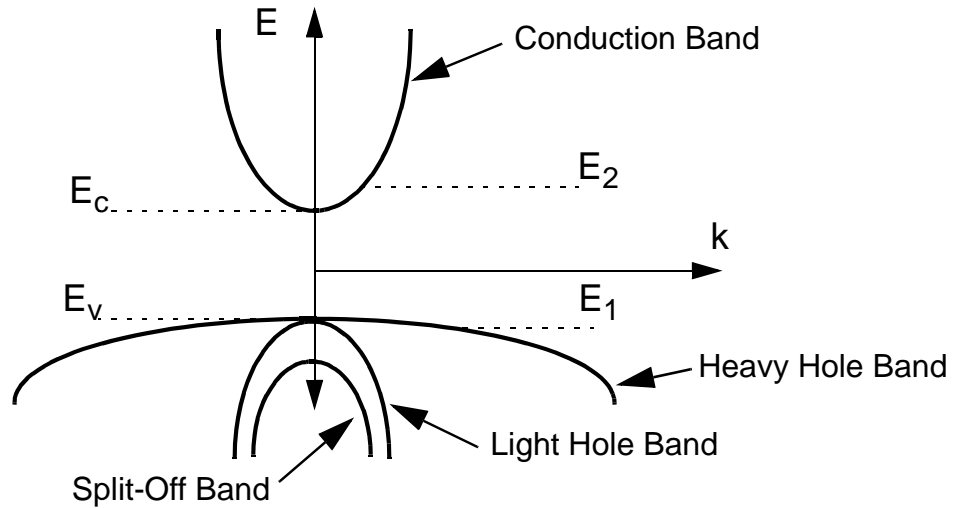


Figure 2.3: Electronic energy vs. momentum diagram for a direct bandgap semiconductor showing a transition from valence band (E_1) to conduction band (E_2). The lowest energy state in the conduction band is E_c and valence band is E_v .

results in strain. As long as the strain energy is below that needed to form a dislocation in the material, layers with low defect densities can be grown. This limits the composition and thickness of $\text{In}_x\text{Ga}_{1-x}\text{As}$ layers that can be grown on a GaAs substrate [19]. Further addition of strain modifies the bandgap energy by

$$\Delta E_g(x) = 0.4484x - 0.3573x^2 + 0.02168x^3 \quad (2.18)$$

for a pseudomorphically strained layer [18].

Another important factor in the design of heterojunctions and quantum wells is the alignment of the bandgaps between the 2 materials. $\text{Al}_x\text{Ga}_{1-x}\text{As}$ and $\text{In}_x\text{Ga}_{1-x}\text{As}$ have type I band alignments, meaning that when going from the lower bandgap material to the higher the energy of the conduction band increases and the valence band decreases. Approximately 60% of the difference in bandgap energy occurs in the conduction band offset and 40% in the valence band offset. A common way of doing band alignment is based on electron affinity, but it is not correct and the appropriate band offsets have to be determined for the materials system in use [20].

2.2.2 Photon absorption and emission in semiconductors

Optical absorption and gain in semiconductors are the result of three processes: absorption, spontaneous emission, and stimulated emission. All three processes can be described by rate equations giving the number of events per second. Figure 2.4 shows a schematic diagram of each process.

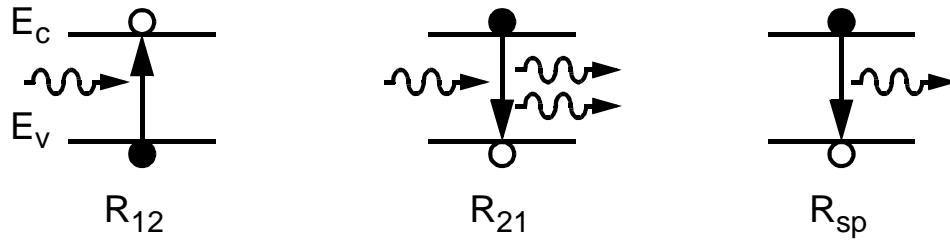


Figure 2.4: Radiative electronic transitions between the conduction and the valence bands of a semiconductor [23]. Absorption (Left), Stimulated Emission (Center), Spontaneous Emission (Right).

2.2.2.1 Absorption

Absorption occurs when a photon with an energy larger than the bandgap is dissipated through exciting an electron from the valence band to the conduction band as shown on the left of Figure 2.4. The rate of absorption is R_r times the probability of finding an electron in the valence band f_1 , times the probability of find an empty state in the conduction band $(1-f_2)$

$$R_{12} = R_r \cdot f_1(1 - f_2) \quad (2.19)$$

where R_r is the rate if all states are available for radiative transitions. Note that only photons with energies greater than the bandgap are absorbed in this process.

R_r is determined from Fermi's Golden Rule [23]

$$R_r = \frac{2\pi}{\hbar} |H_{21}|^2 \rho_f(E_{21}) \quad (2.20)$$

where H_{21} is the dipole matrix element given by

$$H_{21} \equiv \langle \psi_2 | H(r) | \psi_1 \rangle \quad (2.21)$$

where ψ_1 and ψ_2 are the initial and the final electron wavefunctions. $H(r)$ is the electronic field perturbation caused by the incident photon and ρ_f is the density of available states for transitions at a given energy.

R_r can also be related to Einstein's stimulated rate constant, B_{21} as [23]

$$R_r = B_{21} h^2 \nu_0 N_p \rho_r \quad (2.22)$$

where ν_0 is frequency of the photon and N_p is the photon density.

The probability of having an electron in the conduction band, f_1 , or in the valance band, f_2 , are given by Fermi-Dirac statistics. The probability of having an electron at E_2 and a hole at E_1 is given by

$$f_1 = \frac{1}{e^{(E_1 - E_{fv})/(kT)} + 1} \quad \text{and} \quad (2.23)$$

$$f_2 = \frac{1}{e^{(E_2 - E_{fc})/(kT)} + 1} \quad (2.24)$$

the Fermi-Dirac equations [24] where E_{fc} and E_{fv} are the quasi-Fermi levels for the conduction and valance bands. When a semiconductor is not being pumped by an external energy source the quasi-Fermi levels are equal and that is called the equilibrium Fermi level. When a current flows through the semiconductor or when photons with an energy greater than the bandgap are incident on the it, the number of electrons in the conduction band increases and the number of electrons in the valance band decreases. In either case the electron and hole populations are different than in thermal equilibrium and are each quantified by a quasi-Fermi level.

2.2.2.2 Simulated Emission

Simulated emission occurs when the field from a passing photon causes an electron from the conduction band to recombine with a hole from the valence band releasing a second photon in phase with the first as shown in the center of Figure 2.4. Both photons have an energy greater than the bandgap. The rate of simulated emission is R_r times the probability of finding an electron in the conduction band f_2 , times the probability of finding an empty state in the conduction band $(1-f_1)$

$$R_{21} = R_r \cdot f_2(1 - f_1) . \quad (2.25)$$

Simulated emission is the heart of what allows laser oscillation to occur. In order to have coherent oscillation a coherent gain mechanism is needed to replace the photons lost due to absorption or through the mirrors as output power.

2.2.2.3 Optical Gain

Finally we can determine the optical gain of a semiconductor. Gain is simply the difference between the stimulated emission rate and the absorption rate

$$R_{st} = R_{21} - R_{12} = R_r \cdot (f_2 - f_1) . \quad (2.26)$$

The minimum amount of pump energy needed to have optical gain can be determined by setting $R_{st}=0$ which gives $E_{fc}-E_{fv}=E_2-E_1$ which means the difference between the quasi-fermi levels for electrons and holes must be greater than the bandgap energy. This means that there are more electrons excited into the conduction band than are left in the valence band, a condition known as population inversion assuming an equal density of states for the two bands. This requires a fairly high carrier density which is often produced using a double-heterostructure quantum well.

The use of quantum wells solves several problems with exciting that many carriers in a semiconductor and the thermal problems that entails. Carrier density is higher in a narrower bandgap material surrounded by wider bandgap materials due to carrier confinement, so a lower pump energy density is needed to reach population inversion. By

localizing the gain to a small region in the device less energy is needed to pump the smaller volume. InGaAs quantum wells on GaAs are strained, which lifts the light hole heavy hole degeneracy and reduces the density of states. The lower density of states means that the quasi-fermi level separation is larger for the same pump energy density. Finally since the quantum well has the smallest bandgap of any material in the laser the photons we have worked so hard to generate will not be absorbed in an other unpumped layers.

The optical gain per unit length is then given by

$$g = \frac{1}{N_p} \frac{dN_p}{dz} = \frac{1}{v_g N_p} \frac{dN_p}{dt} = \frac{1}{v_g N_p} (R_{21} - R_{12}). \quad (2.27)$$

where v_g is the group velocity for light. The optical gain versus wavelength for 8 nm $\text{In}_{0.2}\text{Ga}_{0.8}\text{As}$ / GaAs quantum wells grown pseudomorphically on a GaAs substrate at various pumping levels is shown in Figure 2.5.

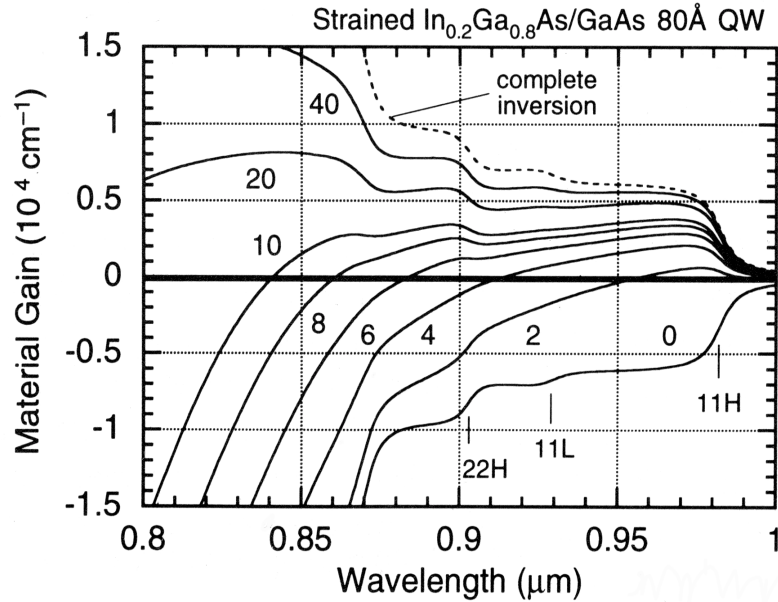


Figure 2.5: Calculated TE gain spectrum vs. carrier density in $\text{In}_{0.2}\text{Ga}_{0.8}\text{As}/\text{GaAs}$ 80Å QW. Indicated values are the sheet carrier densities: $\times 10^{12} \text{cm}^{-2}$ [23].

2.2.2.4 Spontaneous emission

Spontaneous emission occurs when an electron and hole recombine and release a photon without the presence of a stimulating photon as shown on the right of Figure 2.4. The energy of the emitted photon is given by the difference in energy between the electron in the conduction band E_2 and the hole in the valence band E_1 . The emitted photon has a random phase and is not coherent with the laser oscillation. Spontaneous emission is a source of noise in the laser oscillator and is usually the dominant noise source in well designed systems.

The spontaneous emission rate per unit energy per unit active volume, R_{sp} , is related to the gain by [23]

$$R_{sp}^{21} = \frac{1}{h} \rho_o(\nu_{21}) \cdot \nu_g n_{sp} g \quad (2.28)$$

where n_{sp} is the population inversion factor, ρ_o is the optical mode density and g is the optical gain. The population inversion factor is related to how hard the semiconductor is being pumped and is defined as

$$n_{sp} = \frac{f_2(1 - f_1)}{f_2 - f_1} = \frac{1}{1 - e^{(E_{21} - \Delta E_f)/kT}} \quad (2.29)$$

The population inversion factor will be used again when we discuss laser linewidth.

Since R_{sp} is proportional to the product of electron and hole concentration and $N_e = N_v$ in an undoped region the rate can be written empirically as

$$R_{sp} \approx B N_e N_h = B N_e^2 \quad (2.30)$$

where $B = 10^{-10} \text{ cm}^3/\text{s}$ for most direct bandgap III-V semiconductors. This simplification is useful when solving the laser rate equations.

2.2.3 Other recombination processes in semiconductors

In addition to the optical processes mentioned above recombination of electrons can occur through trap states and in a three particle process called Auger recombination. Shockley-Read-Hall theory give the recombination rate through trap states as

$$R_{nr} = \frac{NP - N_i^2}{(N^* + N)\tau_h + (P^* + P)\tau_e} \quad (2.31)$$

where N , P , N_i are the electron, hole, and intrinsic carrier densities. N^* and P^* are numerical factors equal to the electron and hole densities when the Fermi level is equal to the trap energy level and τ_h and τ_e are the hole and electron capture times. For the case of an updoped highly pumped quantum well where $N=P \gg$ than N_i , N^* and P^* this simplifies to

$$R_{nr} = \frac{N}{\tau_h + \tau_e} = AN \quad (2.32)$$

where A is a constant that depends on the doping and material quality of the semiconductor. Auger recombination is a three particle process where the energy of an electron hole recombination excites a third carrier. The rate is given by

$$R_{nr} = CN^3 \quad (2.33)$$

where C is $\sim 5 \cdot 10^{-30} \text{ cm}^6/\text{s}$ for GaAs [23].

2.2.4 Refractive Index

Now that we have quantified the effects of semiconductor materials on the real part of the propagation constant, the imaginary part must be considered. The optical phase for acquired when passing through a unit length of semiconductor material is $\omega n/c$. The index of refraction is a property of the semiconductor and can be related to the optical absorption by the Kramers Kroenig transformation [25]

$$n(E) = 1 + P \int_0^{\infty} \frac{\alpha(E')}{E'^2 - E^2} dE' . \quad (2.34)$$

The result shows that a narrower bandgap semiconductor generally has a larger refractive index for a given photon energy.

The refractive index will depend on the material composition and the wavelength of the propagating photon. Over a large wavelength range the dependence of refractive index can be quite complex, however over smaller ranges particularly below the bandgap it can be described by a relatively simple model dielectric function.

2.2.4.1 $\text{Al}_x\text{Ga}_{1-x}\text{As}$

The index versus photon energy characteristics in a semiconductor have been well fit by the Adachi model dielectric function technique for the $\text{Al}_x\text{Ga}_{1-x}\text{As}$ alloys [16]. The general equations are

$$\epsilon_1(\omega, x) = A_o \left\{ f(\chi) + \frac{1}{2} \left[\frac{E_o}{E_o + \Delta_o} \right]^{3/2} f(\chi_{so}) \right\} + B_o \quad (2.35)$$

with

$$f(\chi) = \chi^{-2} [2 - (1 + \chi)^{1/2} - (1 - \chi)^{1/2}] \quad (2.36)$$

$$\chi = \frac{\hbar\omega}{2\pi E_o} \quad E_o(x) = 1.425 + 1.155x + 0.37x^2 \quad (2.37)$$

$$\chi_{so} = \frac{\hbar\omega}{2\pi(E_o + \Delta_o)} \quad E_o + \Delta_o(x) = 1.765 + 1.115x + 0.37x^2 \quad (2.38)$$

$$A_o = 6.3 + 19x \quad B_o(x) = 9.4 - 10.2x \quad (2.39)$$

for all compositions $0 \leq x \leq 1$ and for photon energies less than the bandgap energy E_o .

2.2.4.2 $\text{In}_x\text{Ga}_{1-x}\text{As}$

There is much less information available for $\text{In}_x\text{Ga}_{1-x}\text{As}$ alloys and the data is from bulk material, not the pseudomorphically strained layers grown on GaAs [18]. Neverthe-

less a reasonable fit has been produced by a simpler method from Afromowitz [26] to interpolate between the GaAs and InAs binary data. We use the equation

$$n(\omega, x) = \sqrt{1 + \frac{E_0 E_d}{E_0^2 - E^2}} \quad (2.40)$$

with

$$E_0 = 4.7 - 3.2x \quad E_d = 33.65 - 17.45x \quad (2.41)$$

to determine the refractive index of $\text{In}_x\text{Ga}_{1-x}\text{As}$. Since only thin $\text{In}_x\text{Ga}_{1-x}\text{As}$ layers can be grown and they are used only in the quantum well of our devices the influence of any inaccuracy in our estimate of the index for $\text{In}_x\text{Ga}_{1-x}\text{As}$ is fairly small.

2.3 Semiconductor laser rate equations

The semiconductor laser rate equations are used to describe the number of electrons in the quantum well active region and the number of photons in the lasing mode. This results in two coupled differential equations, one for the electron population and one for the photon population.

In electrically pumped semiconductor diode lasers the quantum well is pumped by the carriers that flow in the intrinsic region of a PiN structure. The number of electrons generated in the quantum well active region of volume V due to a current I per unit of time is

$$R_{\text{gen}} = \frac{\eta_i I}{qV} \quad (2.42)$$

where η_i is an empirical factoring measuring injection efficiency which is close to unity in well designed structures.

The electron recombination rate is the sum of the spontaneous emission rate, photon generation rate, the nonradiative recombination and a leakage rate which is another empirical factor to account for carriers escaping from the quantum well. The equations for all

but the carrier leakage rate over the barriers R_l have been presented and the total recombination rate is

$$R_{\text{rec}} = R_{\text{sp}} + R_{\text{nr}} + R_l + R_{\text{st}} . \quad (2.43)$$

The carrier leakage rate over the barriers is close to zero in a well designed quantum well system such as InGaAs/GaAs so we will assume that term is very small. Using equations (2.30), (2.32) and (2.33) we can determine the recombination rate as a function carrier density N giving

$$R_{\text{rec}} = BN^2 + (AN + CN^3) + R_{\text{st}} . \quad (2.44)$$

where carrier leakage rate has been set to zero. This result is useful when numerically solving the electron rate equation. The electron rate equation is

$$\frac{dN}{dt} = R_{\text{gen}} - R_{\text{rec}} \quad (2.45)$$

where the rate of change in the number of electrons is equal to the generation rate minus the recombination rate. Inserting Equations (2.42) and (2.43) allows us to write

$$\frac{dN}{dt} = \frac{\eta_i I}{qV} - (R_{\text{sp}} + R_{\text{nr}} + R_{\text{st}}) . \quad (2.46)$$

Finally including Equations (2.27) and (2.44) we get the standard form for the electron rate equation

$$\frac{dN}{dt} = \frac{\eta_i I}{qV} - (BN^2 + AN + CN^3 + g v_g N_p) . \quad (2.47)$$

The photon rate equation relates the rate of change in photon number to the optical gain and loss rates. The photons are confined by a waveguide structure to a volume V_p . The confinement is not nearly as good as the confinement in the quantum wells of the electrons so $V_p > V$. Assuming that the photons are confined to a region of V_p the photon rate equation is

$$\frac{dN_p}{dt} = \frac{V}{V_p} g v_g N_p + \frac{V}{V_p} \beta_{\text{sp}} R_{\text{sp}} - \frac{N_p}{\tau_p} . \quad (2.48)$$

V is just the volume of the quantum wells in the laser active region, but V_p is the harder to calculate effective overlap volume of the photons with the quantum wells which also includes a factor for standing wave enhancement. We simplify the rate equations by defining an optical confinement factor $\Gamma=V/V_p$. We then have to calculate the confinement factor Γ as the integral of the photon electronic field integrated over the active region volume divided by the same field integrated over the entire laser

$$\Gamma = \frac{\int_{-\frac{w}{2}}^{\frac{w}{2}} |U|^2 dv}{\int |U|^2 dv} \quad (2.49)$$

In VCSELs the confinement factor can easily be separated into two parts $\Gamma=\Gamma_{xy}\Gamma_z$ where Γ_{xy} is the transverse confinement factor which is typically ~ 1 and Γ_z is the axial confinement factor. The axial confinement factor Γ_z is given by the following equation [23]

$$\Gamma_z = \frac{L_a}{L} \left[1 + \frac{\sin \beta L_a}{\beta L_a} \right] \quad (2.50)$$

where L_a is the length of active region and $\beta=2\pi n/\lambda$ is the real part of the propagation constant. The axial confinement can be separated into a fill factor, L_a/L , and an enhancement factor $\left[1 + \frac{\sin \beta L_a}{\beta L_a} \right]$. The enhancement factor can be as large as two, but it can also be zero, showing how important growth accuracy is for VCSELs.

There are two factors in Equation (2.48) we have not mentioned, β_{sp} and τ_p . β_{sp} is the spontaneous emission factor, it relates the coupling of the spontaneous emission to the lasing mode and is given by

$$\beta_{sp} = \frac{q}{I_{th} \tau_p} \left[\frac{n_{sp}}{\eta_i \eta_r} \right]_{th} \quad (2.51)$$

where the subscript th indicates the value measured at laser threshold and $\eta_r = R_{sp}/(R_{sp} + R_{nr})$. τ_p is the photon lifetime defined by the loss rate of photons due to absorption in the cavity and transmission through the mirrors as given by

$$\frac{1}{\tau_p} = v_g \left(\frac{1}{L_{eff}} \ln \left(\frac{1}{r_1 r_2} \right) + \langle \alpha_i \rangle \right) \quad (2.52)$$

where L_{eff} is the effective length of the laser cavity, r_1 and r_2 are the mirror reflectivities, and $\langle \alpha_i \rangle$ is the average of any internal losses in the cavity.

With these equations we can now model semiconductor lasers.

2.4 Current, Voltage and Output Power of semiconductor lasers

As we start to pump current into a semiconductor laser the device will first start to emit incoherent light before it reaches the lasing threshold. Since we are below threshold we can simplify Equation (2.46) by removing the stimulated emission term in the DC case we have

$$\frac{\eta_i I}{qV} = \frac{R_{sp}}{\eta_{rad}} \quad (2.53)$$

where η_{rad} is the radiative recombination efficiency and is defined as $R_{sp}/(R_{sp} + R_{nr} + R_l)$. We can derive the Light Emitting Diode (LED) output as [23]

$$P_{LED} = hvVR_{sp} = \eta_{rad}\eta_i\eta_c I \frac{hv}{q} \quad (2.54)$$

where η_c is the fraction of light emitted into a cone of angles that allow it to escape from total internal reflection.

As the current is increased the optical gain g increases and the round trip gain in equation (2.10) approaches unity. Once the round trip gain reaches unity laser oscillation starts the gain becomes clamped at its threshold value. The clamping occurs because an increase in gain will cause an increase in the number of photons depleting the electron population

and that returns the gain to its threshold value. Increases in pumping current above the threshold value produce a linear increase in the laser output power as shown on the left of Figure 2.6. Since the gain clamping limits the number of carriers in the diode we would also expect the voltage across the diode active region to be clamped. The measured diode voltage also includes the resistive inactive regions and contact resistances resulting in a continued increase in diode voltage, but at a reduced slope as shown on the right of Figure 2.6.

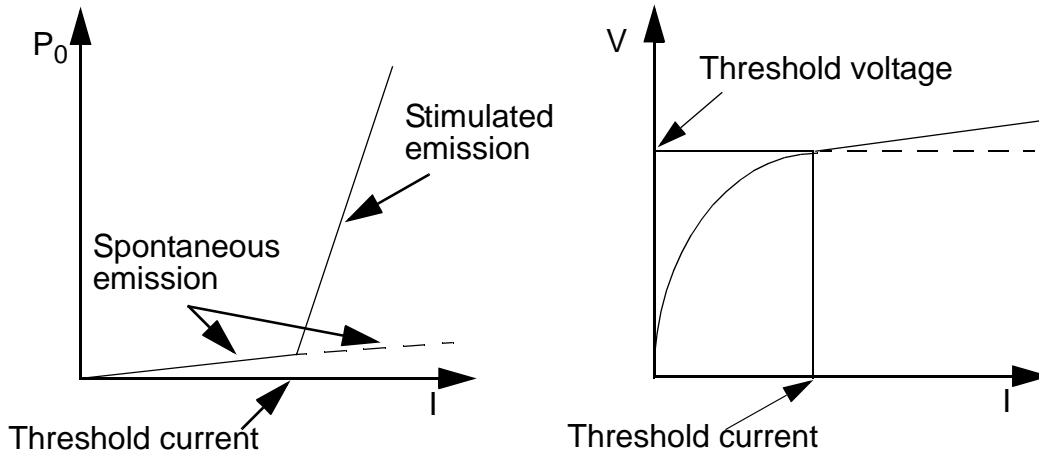


Figure 2.6: Output power (Left) and diode voltage (Right) vs. current for a typical diode laser.

The output power when lasing is also derived from Equation (2.46). First the threshold current needed for the quantum well optical gain to be equal to the mirror and internal losses must be subtracted from the pump current. Knowing that the stimulated emission rate will be much larger than the other recombination rates in an efficient laser and is equal to $v_g g N_p$ we can determine the number of photons in the cavity for a given pump current. Knowing the output coupling of the mirrors the number of photons can be converted into an output power which results in

$$P_{\text{Laser}} = \eta_i \left(\frac{\alpha_m}{\alpha_i + \alpha_m} \right) \frac{h\nu}{q} (I - I_{\text{th}}) = \eta_d \frac{h\nu}{q} (I - I_{\text{th}}) \quad (2.55)$$

where α_m is the mirror output coupling, α_i is the internal loss in the cavity and η_d is the differential quantum efficiency of the device.

2.5 Types of semiconductor lasers

There are two main types of semiconductor lasers, edge-emitting devices and vertical cavity devices. Edge-emitting lasers as shown in Figure 2.7 are fairly long devices, typically a few hundred microns that emit in the plane of the wafer through a cleaved edge hence the name edge-emitter. Since the gain region is long the optical gain can be large which compensates for the relatively low reflectance from the cleaved mirrors of approximately 30%. The electrons and photons are confined in the vertical direction by the heterostructure of the laser. Lateral confinement can be achieved with oxidation, ion-implantation, epitaxial regrowth or Impurity Induced Layers Disorder (IILD) [23]. The optical mode of the device is usually $3\mu\text{m}$ wide or wider, but is usually less than 1 micron high. This produces a highly elliptical output beam which can be difficult to couple into optical fibers.

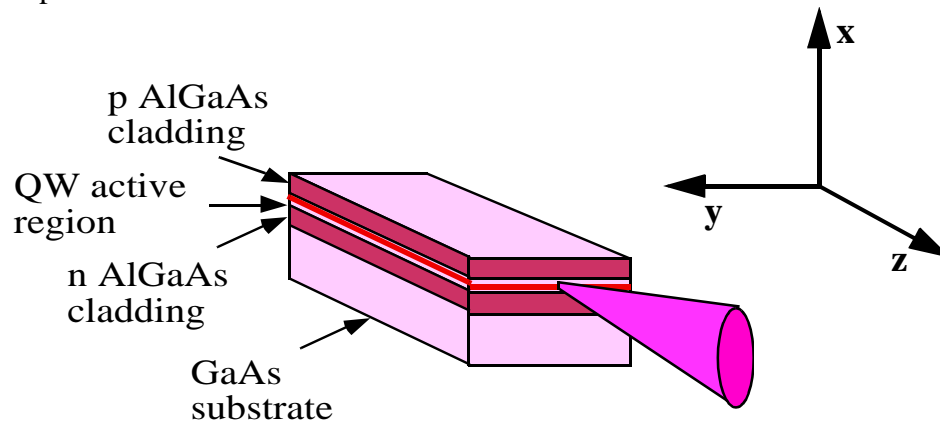


Figure 2.7: Schematic representation of an edge-emitting laser. The corresponding coordinate system is also shown.

Vertical-cavity surface-emitting laser (VCSELs) get their name from the fact that the laser cavity is orientated perpendicular to the plane of the wafer and the laser emission exits through the wafer surface.

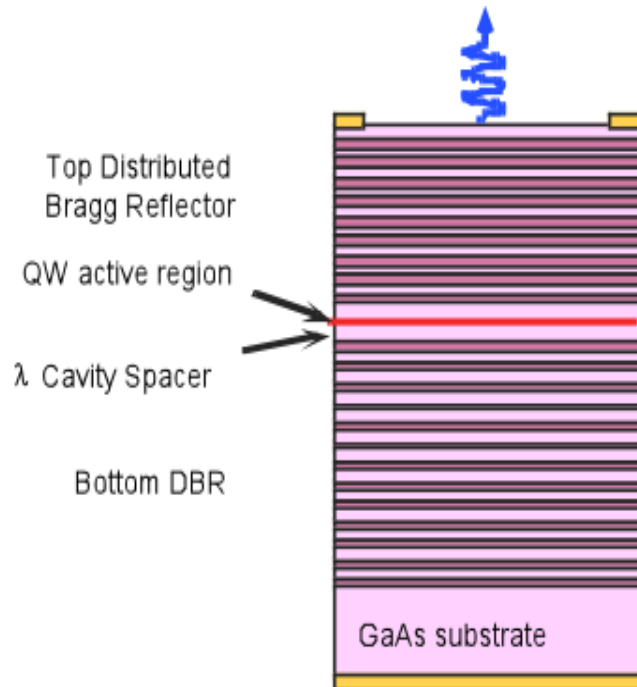


Figure 2.8: Schematic diagram of a VCSEL showing various epitaxial layers.

The first VCSELs were demonstrated by Iga et. al. [27]. Jewel et. al. [28] grew high quality DBR based devices and outlined many of the significant improvements possible in beam shape, scalability, array fabrication and integration possible with the VCSEL structure.

In a VCSEL the gain region is very short, only the width of the quantum wells, so the mirror reflectances have to be very high, usually 99.9% or higher, which requires the use of Distributed Bragg Reflectors (DBRs). Vertical confinement of the electrons is done by the quantum wells. The photons are vertically confined by the DBRs and the cavity. Lateral confinement can be done by the same methods as for edge-emitters, but oxidation based confinement produces devices with significantly higher efficiencies [30]. The out-

put beam from a VCSEL is circular and is therefore much easier to couple into fibers than the highly elliptical beam produced by an edge-emitter.

2.6 Distributed Bragg Reflectors and thin film modeling of lasers

A Distributed Bragg Reflector is a stack of alternating high and low index layers that are one quarter of an optical wave thick. The quarter wave thickness causes the reflectance from both interfaces to add in phase producing a higher reflectance for each additional layer. In theory a reflectance arbitrarily close to unity can be achieved with a thick enough stack. Practically, the reflectivity is limited by absorption but, absorption is very low in epitaxial materials $< 5 \text{ cm}^{-1}$ and the reflectivities can be on the order of 99.99%.

In order to fully understand DBR design we must consider the mathematics needed to model the reflectivity from a series of thin film layers. For an electromagnetic wave normally incident on a plane where the refractive index changes as shown in Figure 2.9 the tangential components of the electric and magnetic field are continuous across the boundary as required by Maxwell's law and are given by

$$E_{\text{inc}} + E_{\text{refl}} = E_{\text{trans}} \quad \text{and} \quad (2.56)$$

$$H_{\text{inc}} - H_{\text{refl}} = H_{\text{trans}} \Rightarrow y_1(E_{\text{inc}} - E_{\text{refl}}) = y_2 E_{\text{trans}} \quad (2.57)$$

where y is the admittance of the medium, subscripts 1 and 2 refer to the left and right regions, and the subscripts *inc*, *refl*, and *trans* refer to incident, reflected, and transmitted fields, respectively. A quantity called the admittance of a medium can be defined by

$$y = \frac{E}{H} = \frac{1}{\eta} = \sqrt{\frac{\epsilon_r \epsilon_0}{\mu_0}} \quad (2.58)$$

where η is the impedance of the medium and is equal to the ratio of electric field component divided by the magnetic field component.

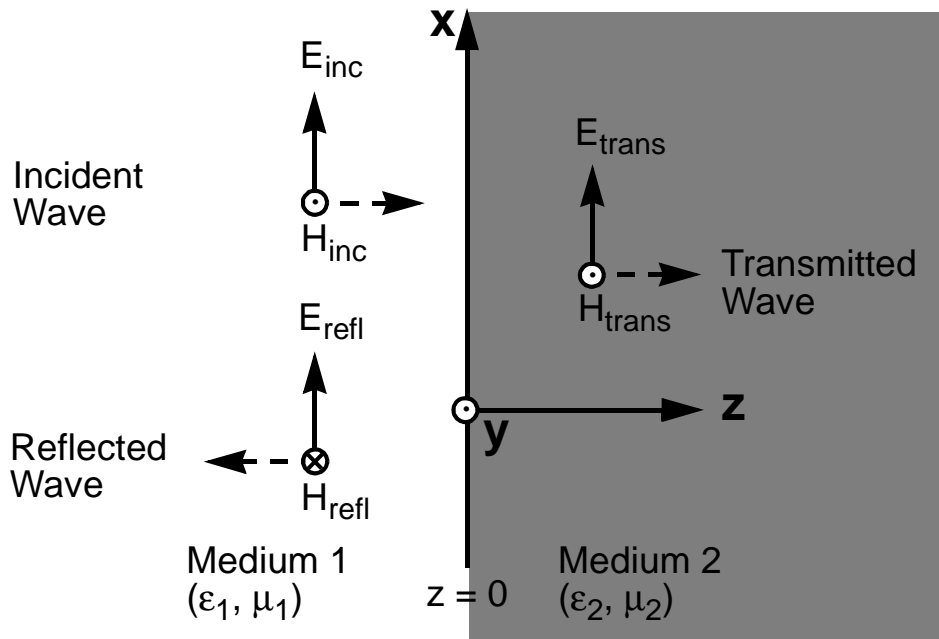


Figure 2.9: Schematic diagram of a normal plane wave incidence on a plane dielectric boundary [32].

The amplitude coefficient of interface reflection, ρ , going from medium one to medium two, is given by

$$\rho = \frac{\eta_2 - \eta_1}{\eta_2 + \eta_1} = \frac{n_1 - n_2}{n_1 + n_2} \quad (2.59)$$

where n_1 and n_2 are the refractive indices of the two media and are given by

$$n = \sqrt{\epsilon_r} . \quad (2.60)$$

The amplitude coefficient of interface transmission, τ , is given by

$$\tau = 1 + \rho = \frac{2\eta_2}{\eta_2 + \eta_1} = \frac{2n_1}{n_1 + n_2} . \quad (2.61)$$

The power reflectance and transmittance of the interface can be calculated as [31]

$$R = \rho^2 = \left| \frac{n_1 - n_2}{n_1 + n_2} \right|^2, \text{ and} \quad (2.62)$$

$$T = \frac{y_2}{y_1} \tau^2 = \frac{\sqrt{\epsilon_2} \left| \frac{2n_1}{n_1 + n_2} \right|^2}{\sqrt{\epsilon_1}}. \quad (2.63)$$

To analyze the reflectance from a stack of thin layers we have to consider the multiple reflections from both surfaces of each layer as shown in Figure 2.10. The admittance approach developed by MacLeod [31] greatly simplifies the calculations needed. Analyzing multiple thin film layers then becomes a simple task of multiplying the admittances of the layers. From the final optical admittance of the structure, reflection and transmission of the structure can be determined. To derive the admittance matrix formalism we will first analyze a single film.

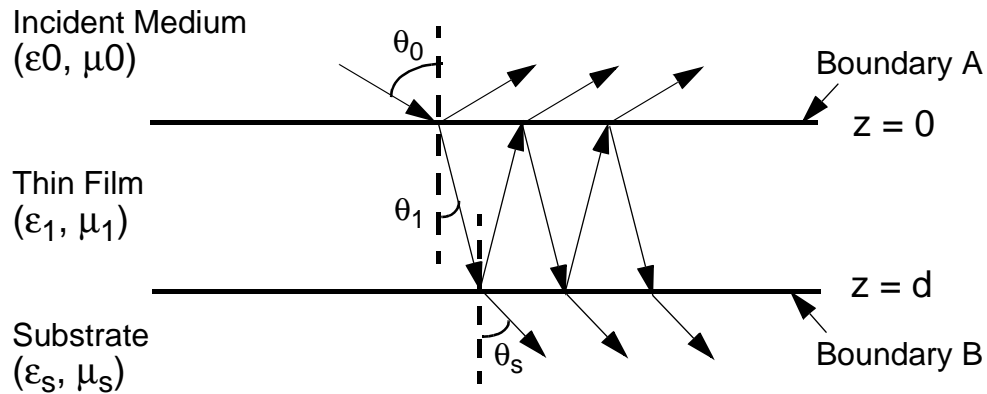


Figure 2.10: Reflections in a thin film.

The expressions for multiple reflections as a sum of forward and backward travelling waves in each medium are written. Since there is no backward travelling wave in the substrate (assuming an infinite thickness), the analysis is simpler starting from the substrate

(boundary B) and ending at the surface (boundary A) rather than the other way around.

Summing these components at boundary B in medium 1, we obtain [31]

$$E_B = E_{1B}^+ + E_{1B}^- \quad \text{and} \quad (2.64)$$

$$H_B = H_{1B}^+ + H_{1B}^- = \eta_1(E_{1B}^+ - E_{1B}^-) \quad (2.65)$$

where subscript + and - are for forward and backward propagating waves.

Solving for the forward and backward term we produce

$$E_{1B}^+ = \frac{1}{2}(E_B + H_B/\eta_1) , \quad (2.66)$$

$$E_{1B}^- = \frac{1}{2}(E_B - H_B/\eta_1) , \quad (2.67)$$

$$H_{1B}^+ = \frac{1}{2}(\eta_1 E_B + H_B) , \quad \text{and} \quad (2.68)$$

$$H_{1B}^- = \frac{1}{2}(-\eta_1 E_B + H_B) . \quad (2.69)$$

Relating these equations to those at interface A allows us to write

$$E_{1A}^+ = E_{1B}^+ \exp(-i\delta) , \quad (2.70)$$

$$E_{1A}^- = E_{1B}^- \exp(i\delta) , \quad (2.71)$$

$$H_{1A}^+ = H_{1B}^+ \exp(-i\delta) , \quad (2.72)$$

$$H_{1A}^- = H_{1B}^- \exp(i\delta) , \quad (2.73)$$

where

$$\delta = 2\pi N_1 d \frac{\cos\theta_1}{\lambda} . \quad (2.74)$$

N_1 is the complex refractive index of medium 1 and can be separated into real and imaginary parts as

$$N = n - ik . \quad (2.75)$$

By writing Equations (2.66) to (2.73) in matrix form, we can relate the electric and magnetic field at boundary A to the electric field at boundary B by [31]

$$\begin{bmatrix} E_A \\ H_A \end{bmatrix} = \begin{bmatrix} \cos \delta & -\frac{i \sin \delta}{\eta_1} \\ -i\eta_1 \sin \delta & \cos \delta \end{bmatrix} \begin{bmatrix} 1 \\ \eta_2 \end{bmatrix} E_B . \quad (2.76)$$

Using the admittance notation, we can write this as

$$\begin{bmatrix} 1 \\ Y_A \end{bmatrix} = \begin{bmatrix} \cos \delta & -\frac{i \sin \delta}{\eta_1} \\ -i\eta_1 \sin \delta & \cos \delta \end{bmatrix} \begin{bmatrix} 1 \\ \eta_2 \end{bmatrix} . \quad (2.77)$$

For a stack of thin films, we can find the admittance of the stack by simply multiplying the admittances of individual layers as [31]

$$\begin{bmatrix} 1 \\ Y \end{bmatrix} = \begin{bmatrix} B \\ C \end{bmatrix} = \left(\prod_{r=1}^m \begin{bmatrix} \cos \delta_r & -\frac{i \sin \delta_r}{\eta_r} \\ -i\eta_r \sin \delta_r & \cos \delta_r \end{bmatrix} \right) \begin{bmatrix} 1 \\ \eta_s \end{bmatrix} . \quad (2.78)$$

Note $\eta_r = N \cos \theta_r$ for TE waves and $N / \cos \theta_r$ for TM waves. θ_r is related θ_0 to by Snell's law

$$n_0 \sin \theta_0 = n_r \sin \theta_r . \quad (2.79)$$

The reflectivity of the stack can be calculated as

$$\rho = \frac{\eta_0 - Y}{\eta_0 + Y} \text{ and} \quad (2.80)$$

the power reflectance is given by [31]

$$R = \left(\frac{\eta_0 - Y}{\eta_0 + Y} \right) \left(\frac{\eta_0 - Y}{\eta_0 + Y} \right)^* = \left(\frac{\eta_0 B - C}{\eta_0 B + C} \right) \left(\frac{\eta_0 B - C}{\eta_0 B + C} \right)^* \quad (2.81)$$

where * denotes the complex conjugate. Similarly, transmission and absorption can be calculated from the admittance matrix

$$T = \frac{4\eta_0 \operatorname{Re}(\eta_s)}{(\eta_0 B + C)(\eta_0 B + C)^*} \text{ and} \quad (2.82)$$

$$A = \frac{4\eta_0 \operatorname{Re}(BC^* - \eta_s)}{(\eta_0 B + C)(\eta_0 B + C)^*} . \quad (2.83)$$

In the special case of normal incidence on exactly quarter wave thick dielectric mirror stacks, we can write the matrix of a quarter wave layer as

$$M = \begin{bmatrix} 0 & -i/\eta \\ -i\eta & 0 \end{bmatrix}, \quad (2.84)$$

which for a matrix of a high (H) and low (L) index layers becomes

$$M = \begin{bmatrix} 0 & -i/\eta_H \\ -i\eta_H & 0 \end{bmatrix} \begin{bmatrix} 0 & -i/\eta_L \\ -i\eta_L & 0 \end{bmatrix} = \begin{bmatrix} \frac{\eta_L}{\eta_H} & 0 \\ 0 & -\frac{\eta_H}{\eta_L} \end{bmatrix}, \quad (2.85)$$

and the matrix of m of those pairs is

$$M = \begin{bmatrix} \left(-\frac{\eta_L}{\eta_H}\right)^m & 0 \\ 0 & \left(-\frac{\eta_H}{\eta_L}\right)^m \end{bmatrix}. \quad (2.86)$$

For this special case, power reflectivity can then be calculated from Equation (2.81) and has a closed form solution [33]

$$R = \left[\frac{1 - \frac{n_s}{n_0} \left(\frac{n_H}{n_L} \right)^{2m}}{1 + \frac{n_s}{n_0} \left(\frac{n_H}{n_L} \right)^{2m}} \right]^2 \quad (2.87)$$

where n_s and n_0 are the substrate and incident medium refractive indices.

Equation (2.87) is only valid for normal incidence on symmetric quarter wave layer stacks at their design wavelength. For all other cases, reflectance at other wavelengths and off normal incidence, have to be evaluated numerically. An optical simulation of normal incidence reflectivity from a DBR made of 20 pairs of alternating GaAs (H) and AlAs (L) layers on a GaAs substrate is shown in Figure 2.11. The bandwidth of the high reflectance is related to the center wavelength by [23]

$$\frac{\Delta\lambda}{\lambda} \cong \frac{4}{\pi} \sin^{-1} \frac{1 - n_L/n_H}{1 + n_L/n_H} . \quad (2.88)$$

For a GaAs/AlAs DBR at 970nm, this gives ~11% bandwidth or ~110nm.

Since a DBR is made of a stack of weakly reflecting mirror pairs, there is considerable penetration depth of the optical field into the mirror stack. Therefore, the DBR can be modeled as a ideal mirror with reflectance R and phase ϕ at a distance L_{eff} from the original interface as shown schematically in Figure 2.12.

The change in the reflected phase as a function of wavelength is approximately

$$\frac{d\phi_m}{d\lambda} = -\frac{\pi n_H n_L}{n_c (n_H - n_L) \lambda} \quad (2.89)$$

where n_c is the refractive index of the cavity [23]. The effective length is then given by

$$L_{\text{eff}} = -\frac{1}{2} \frac{d\phi_m}{d\beta} = \frac{n_H n_L \lambda}{4 n_c (n_H - n_L)} . \quad (2.90)$$

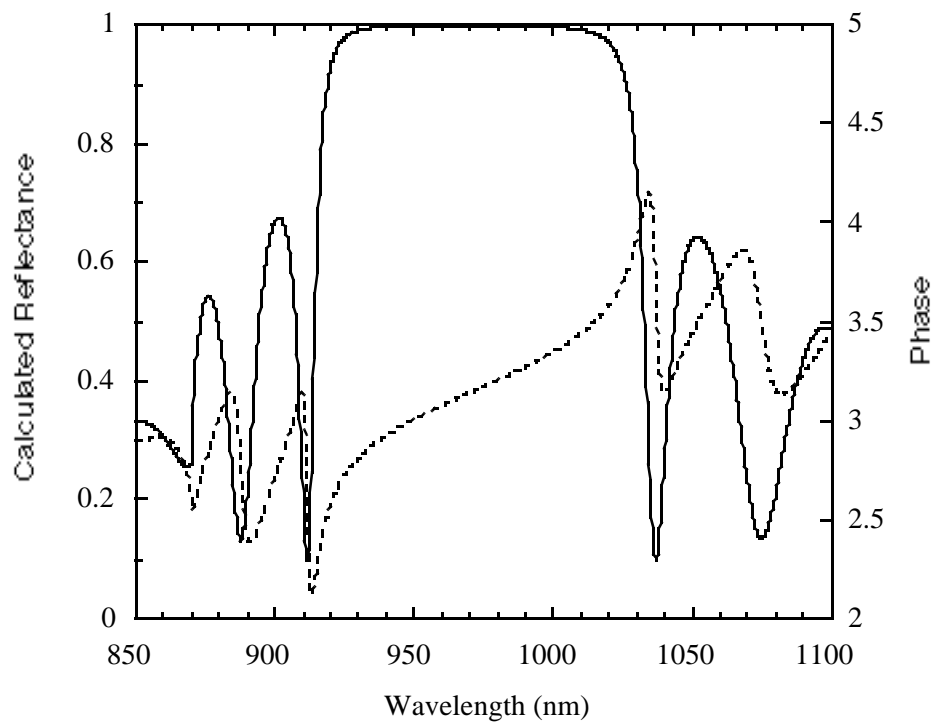


Figure 2.11: Plot of mirror reflectance and phase versus wavelength for 20 pairs of alternating AlAs/GaAs DBR centered near 970nm. The dotted line shows the corresponding phase.

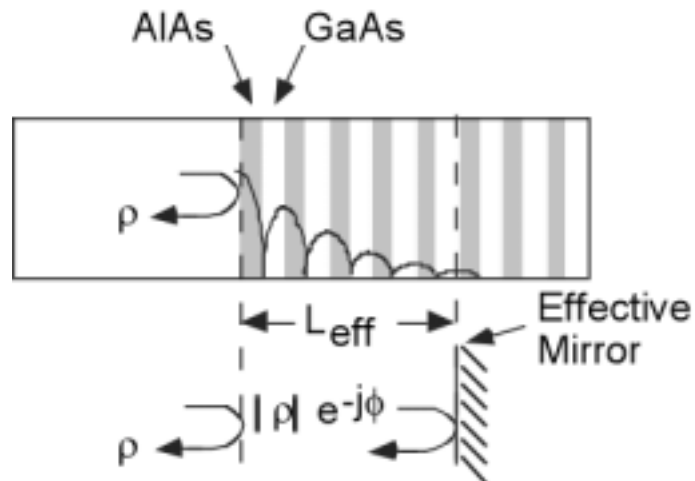


Figure 2.12: Schematic of a DBR mirror and an ideal mirror at the phase depth approximating the DBR mirror.

For the 16 pair AlAs/GaAs DBR near 970nm, L_{eff} is $\sim 1.3\lambda_0$ or $1.26\mu\text{m}$ compared to the physical length of a half wavelength cavity which is $0.27\mu\text{m}$.

A computer program can quickly evaluate the reflectance properties of a stack of thin films including the effects of index dispersion which is important in semiconductor materials. For my work I wrote a thin film solver based on MacLeod's method to assist in the design of VCSELs. The program reads in a structure file and produces a reflectivity spectrum. The calculation speed of a spectrum can be improved by doing the complete range of wavelengths at each layer, rather than looping through the structure multiple times for each wavelength in the spectrum as some intermediate results do not have to be recalculated for each new wavelength, but in a new layer everything must be recalculated. By starting the calculation at the transmitted layer each layer can be solved for by multiplying a 2×2 matrix times a 2×1 vector. If the calculation is started in the incident/reflected layer, each layer requires multiplying a 2×2 matrix times another 2×2 matrix, which requires twice as many operations. The VCSEL usually is made of a periodic structure and a loop statement has been added to the structure file grammar to reduce execution time and to organize the layer structure file.

The thin film code can also be adapted to determine the lasing wavelength and threshold gain for a VCSEL. Since a VCSELs wavelength is defined by the cavity, a search can easily be done in wavelength space to determine the cavity resonance. Once the resonance is found the gain of the quantum wells can be increased and the resonance wavelength refined in alternating steps until the reflectivity becomes infinite which signifies the onset of lasing. Mathematically the search looks for a zero in the denominator of Equation (2.81). A third program plots the standing wave profile inside the VCSEL to insure that the quantum wells are properly aligned with antinodes in the optical field. This set of tools allows VCSEL designs to be designed and modeled quickly and efficiently.

Chapter

3

Micromachined Membranes and VCSEL Tuning

The VCSEL has a very short cavity compared to other semiconductor lasers, in fact the physical cavity can be as short as $1/2$ of a wavelength or $0.27 \mu\text{m}$ for a 980 nm GaAs cavity design. However the effective length of the top and bottom DBRs due to phase of the reflection must also be considered when calculating the axial mode spacing. For GaAs/AlAs DBRs at 980 nanometers the effective length due to the reflection phase is $1.26 \mu\text{m}$, so the effective cavity length for a VCSEL is approximately $3 \mu\text{m}$. This extremely short cavity length allows the axial mode spacing from Equation (2.9) to be a very large $\sim 100 \text{ nm}$ which is larger than the optical gain bandwidth of the quantum wells. Since there is only one axial mode which overlaps the region where optical gain is larger than the optical loss, the wavelength of the VCSEL can be easily tuned by changing the length of the cavity. In an edge-emitting laser the cavity is at least $100 \mu\text{m}$ long giving an axial mode spacing of at most a few tenths of a nm . If one were to try to tune an edge-emitting laser by changing the cavity length the wavelength would shift at most the axial mode spacing before another mode was closer to the gain peak of the quantum wells. When a new mode has a higher gain than the current lasing mode, more photons will be emitted into the new mode and the laser will start oscillating on the new mode. This happens very quickly, typically in a few nanoseconds and is called mode hopping. A plot comparing the axial mode spacing in edge-emitters and VCSELs is shown in Figure 3.1.

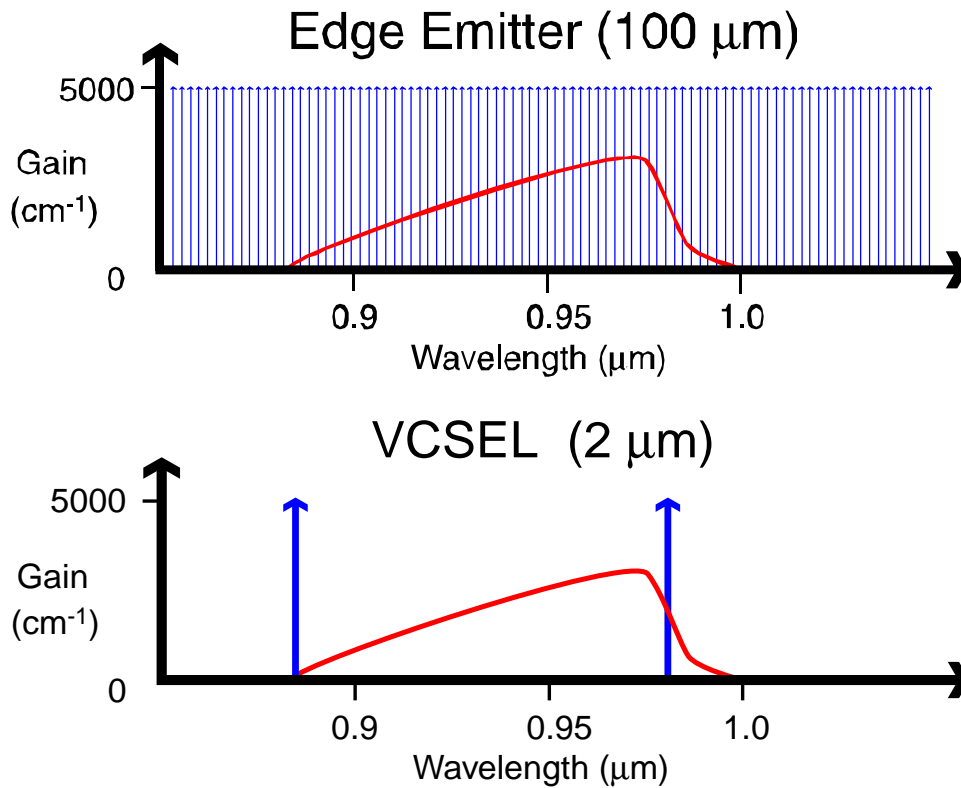


Figure 3.1: Cavity axial modes shown as arrows and the optical gain of quantum wells shown as a curve for Edge-Emitters and VCSELs.

3.1 Membrane displacement

Figure 3.2 shows a schematic cross sectional view of the MTVCSSEL. The left side of the figure shows the membrane in the equilibrium condition with no bias voltage applied. The right side shows a membrane where the electrostatic attraction from an applied bias has pulled the membrane shortening the laser cavity.

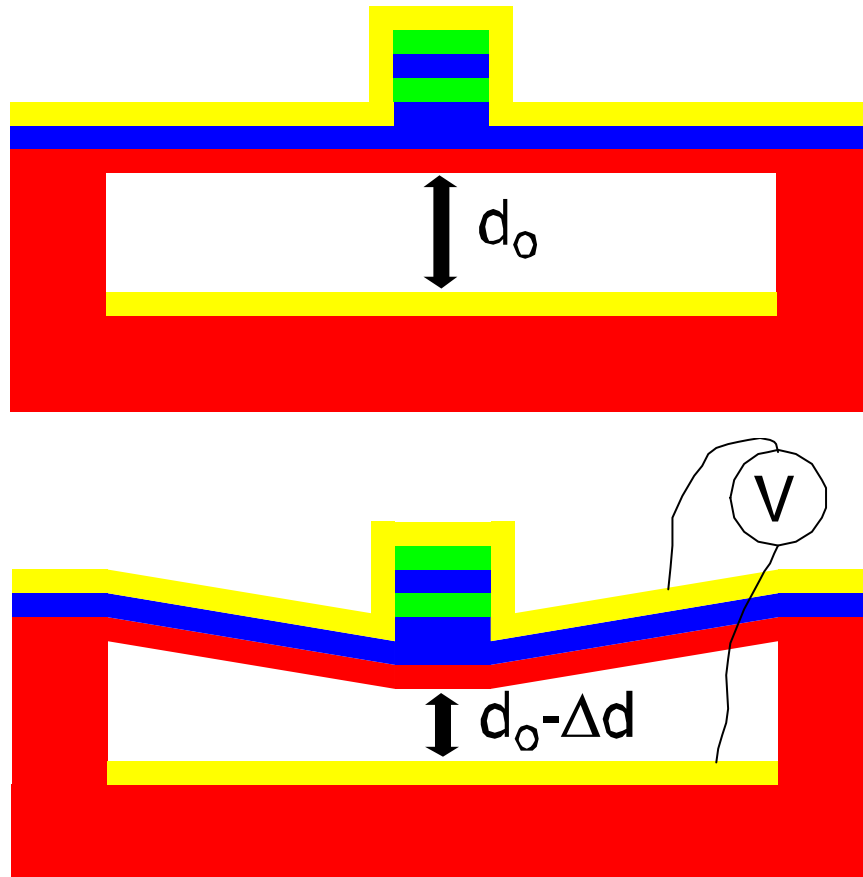


Figure 3.2: Side view of electrostatic membrane displacement.

3.1.1 Electrostatic and Elastic Forces

The displacement of the membrane is controlled by the balance between the electrostatic attraction force and the elastic restoring force in the membrane legs. The metal layer on top of the membrane and the P+ contact layer can be modeled as the two surfaces of a parallel plate capacitor. The electrostatic force, F_{es} , between the plates can be calculated

by differentiating the energy stored in the capacitor, U , with respect to the gap thickness, L_g .

$$F_{es} = \frac{dU}{dL_g} = \frac{d}{dL_g} \left(\frac{1}{2} CV^2 \right) \quad (3.1)$$

Solving for the present structure results in

$$F_{es} = -\frac{\epsilon_o AV^2}{2(L_d/\epsilon_d + L_g)^2} \quad (3.2)$$

where L_d and ϵ_d are the length and dielectric constant of any dielectric layers in gap between the plates.

The restoring force can be modeled as a linear elastic spring for small displacements

$$F_r = k_{eff} \Delta L_g = k_{eff} (L_{g,o} - L_g) \quad (3.3)$$

where k_{eff} is the linear spring constant and $L_{g,o}$ is the equilibrium gap thickness with no bias. By equating Equations (3.2) and (3.3) we produce an equation for the gap thickness.

$$L_g = L_{g,o} - \frac{\epsilon_o AV^2}{2k_{eff}(L_d/\epsilon_d + L_g)^2} \quad (3.4)$$

The gap thickness can be graphically calculated by plotting both the electrostatic and restoring forces as a function of gap thickness and finding the intersection of the lines. A typical example is shown in Figure 3.3.

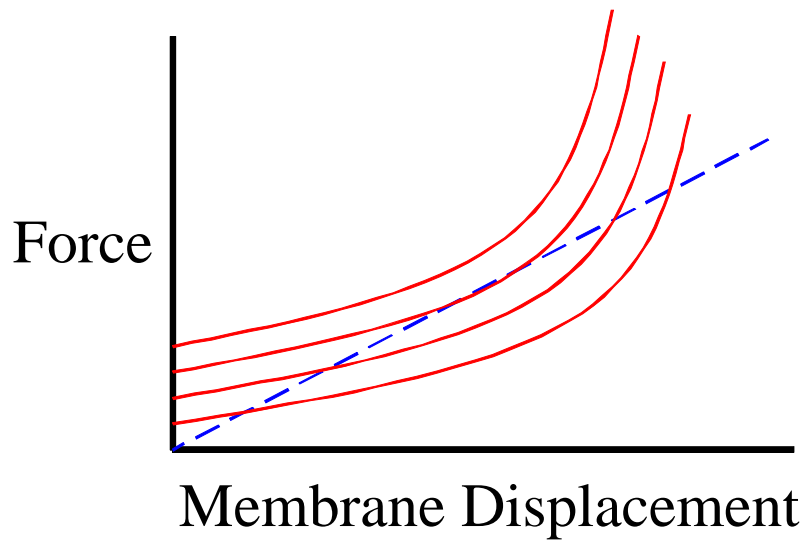


Figure 3.3: Elastic restoring force (dashed lines) and electrostatic force (solid curves) for four different applied biases as a function of membrane displacement.

The linear restoring force is plotted as a dashed line. The electrostatic force has been plotted for 4 applied biases. At the lowest three biases the curves intersect indicating that a stable membrane displacement can be achieved. In fact they intersect at two points showing that there are two stable operating points for those applied voltages which can cause hysteresis in the tuning characteristics. At the highest voltage the curves no longer intersect, in this case the membrane will be pulled down to the substrate. This causes two problems. The first problem is that the typical largest distance that the membrane can be pulled down before collapse is about 1/3 of the original gap [35]. The second problem occurs when the membrane hits the substrate. The membrane and the substrate are defined by wet etching and are very smooth as needed for a high quality optical surfaces. If they come into contact they have a high probability of sticking together due to Van der Waals forces. Once they are stuck together it is nearly impossible to separate them and the membrane is permanently fixed in one position, which prevents tuning. The problem of stiction has been solved in some MEMs devices adding a texture to one or both of the surfaces

[35], but this is not possible in the MTVSEL because both surfaces need to be of a high optical quality and therefore very smooth.

3.1.2 Effective Spring Constant

The effective spring constant of the membrane can be approximated by a straightforward one-dimensional beam analysis. There are a large variety of effects to consider and the modeling can be done to different levels of precision [35]. The most basic model assumes that the central region is rigid, the legs are thin, flexible and under tension. Corrections for semirigid legs under tension and even rigid pillars can be calculated [7][35].

However the three-dimensional nature of the problem limits the accuracy of these methods and requires a finite element simulation to produce an accurate value for the effective spring constant. There are several conditions that the one-dimensional model cannot account for, such as the following examples. The spring constant will increase and become nonlinear at large membrane deflections. The central region of the membrane is not rigid and will bend. The membrane is made of different layers that have different mechanical properties including widely different values for their intrinsic biaxial stress levels.

Even with all of these variations the results from simulations, one-dimensional calculations, and measured results typically match within 10% to 20% [36]. In fact the intrinsic biaxial stress can usually only be measured to a 10% accuracy [37]. So the accuracy of the one-dimensional model is probably as good as can be expected without more precise knowledge of the characteristics of the structure.

3.1.3 Rigid central region with thin flexible legs under tension

We are going to assume that all of the electrostatic force is concentrated onto a completely rigid central region, which is supported by flexible legs of length l , width b , and thickness h . The legs are in a state of biaxial stress σ that is calculated by averaging the stress in the different layers over the thickness of the membrane. We will assume that the

legs are thin enough such that the biaxial stress is much larger the stress induced from bending in the legs. This is often the case for micromachined membranes [36]. The free body diagram for that condition is shown in Figure 3.4 were the rigid central region has been displaced by an amount δ vertically down. The vertical component of the tension

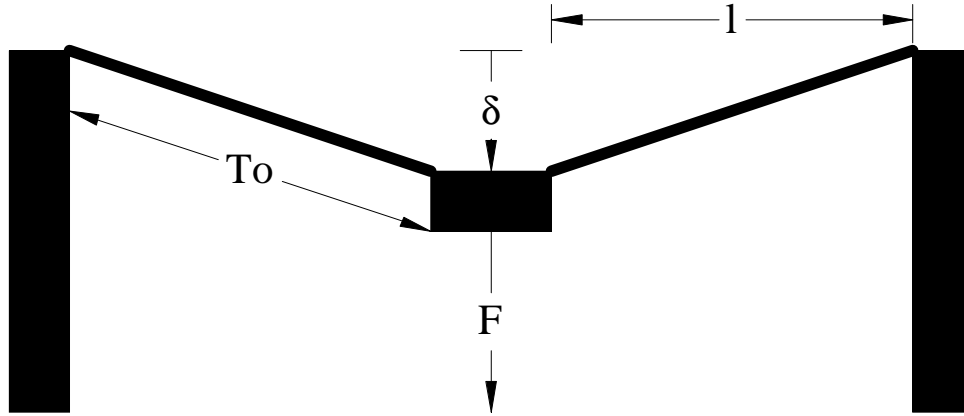


Figure 3.4: Free body diagram of membrane.

($T_0 = N_1 b h \sigma$) in the membrane legs produces a restoring force given by

$$F = N_1 b h \sigma \frac{\delta}{\sqrt{l^2 + \delta^2}} \cong N_1 \frac{b h}{l} \sigma \delta \quad (3.5)$$

where N_1 is the number of legs. The spring constant is then

$$k_{\text{eff}} = \frac{N_1 b h \sigma}{l}. \quad (3.6)$$

From a process development point of view, given a mask set which defines the lateral dimensions of the structure the only control we have over the spring constant is the thickness of the layer and the intrinsic stress level. The layer thickness is fixed to a given amount plus any multiple of a half wavelength by the optical requirements for the structure, since a half wavelength layer is almost transparent optically. However, the intrinsic stress levels can be manipulated by varying the process used to deposit the layer.

3.2 Membrane tuning of VCSELs

Figure 3.5 shows a picture of a plain vanilla VCSEL on the left and an approximation of the structure with hard mirrors spaced back by the effective length of the DBR mirrors on the right.

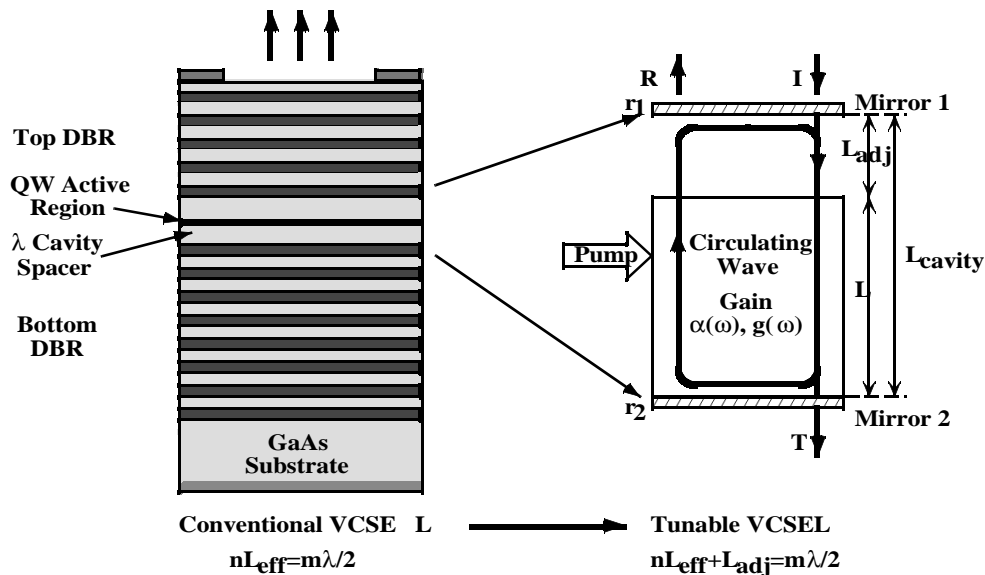


Figure 3.5: Schematic showing transformation from a fixed wavelength VCSEL to a wavelength tunable VCSEL.

As shown on the right of Figure 3.5 wavelength tuning is accomplished by moving the top mirror that is mounted on a micromachined membrane up and down. This concept was first patented by Pezeshki and Harris in 1992 [38] and was demonstrated by Larson in 1994 [39], and has been developed into a product by Core-Tek [40]. The combination of an air gap and a semiconductor cavity can be used to produce three different cavity designs, the air coupled cavity (ACC), the extended cavity (EC), and the semiconductor coupled cavity (SCC) as shown in Figure 3.6.

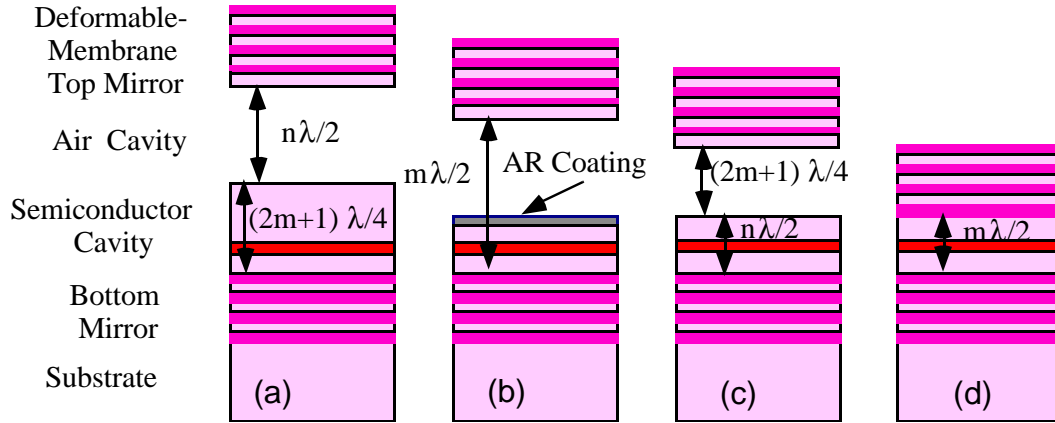


Figure 3.6: The three cavity configurations for micromachined wavelength tunable VCSELs showing the air gap and the semiconductor cavity thickness: (a) Air coupled cavity (ACC), (b) Extended cavity (EC), (c) Semiconductor coupled cavity (SCC), and (d) conventional VCSEL.

3.2.1 Tuning rate analysis

In a basic Fabry-Perot cavity with two DBR mirrors and an air gap with a thickness which is a multiple of $\lambda/2$, the wavelength shift produced by changing the cavity thickness is

$$\frac{\Delta\lambda}{\lambda} = \frac{\Delta d}{L_{\text{eff}}} \quad (3.7)$$

where L_{eff} is the total effective cavity length, which is the sum of $L_{\text{airgap}} + L_{\text{eff}}(\text{mirror 1}) + L_{\text{eff}}(\text{mirror 2})$. $L_{\text{eff}}(\text{mirror})$ is the effective length of the mirror and can be calculated using Equation (2.90). The wavelength tuning rate $\Delta\lambda/\Delta d$ is λ/L_{eff} .

In the case where there are two cavity sections, a semiconductor cavity and an air gap, a closed form solution can also be found for a few simple cases. The air gap and the top mirror can be modeled as a cavity with a tunable phase shift. Using the formulas from [7] we set R_1 equal to R_c , the interface reflectance between the air gap and the semiconductor

cavity, and we set R_2 equal to R_m , the top mirror reflectance. The reflectance and phase for the model cavity are given by

$$R_{\text{eff}} = \frac{R_c + R_m + 2\sqrt{R_c R_m} \cos(\pi + \phi_g)}{1 + R_c R_m + 2\sqrt{R_c R_m} \cos(\pi + \phi_g)} \quad (3.8)$$

$$\phi_{\text{eff}} = \tan^{-1} \frac{\sqrt{R_m}(1 - R_c) \sin(\pi + \phi_g)}{\sqrt{R_c}(1 + R_m) + \sqrt{R_m}(1 + R_c) \cos(\pi + \phi_g)} \quad (3.9)$$

where ϕ_g is the round trip phase in the air gap. ϕ_g is equal to $2\beta L_g + 2(\beta - \beta_0)L_m$, where $\beta = 2\pi/\lambda$, L_g is the air gap thickness, and L_m is the effective length of the top mirror. If we assume $R_m = 1$ (which is approximately true in all VCSELs), the phase coupling factor, $\gamma_\phi = d\phi_{\text{eff}}/d\phi_g$ is given by

$$\gamma_\phi = \frac{(1 - R_c)[1 + R_c + 2\sqrt{R_c} \cos(\pi + \phi_g)]}{4R_c + 4\sqrt{R_c}(1 + R_c) \cos(\pi + \phi_g) + 1 + R_c^2 + 2R_c \cos 2\phi_g} \quad (3.10)$$

At designed resonance wavelength γ_ϕ can be simplified for the Air Coupled Cavity and Semiconductor Coupled Cavity to,

$$\text{For SCC} \quad \gamma_\phi = \frac{1 - \sqrt{R_c}}{1 + \sqrt{R_c}} \quad \text{and} \quad (3.11)$$

$$\text{For ACC} \quad \gamma_\phi = \frac{1 + \sqrt{R_c}}{1 - \sqrt{R_c}} \quad (3.12)$$

The GaAs to air interface has an $R_c \sim 0.3$ which gives $\gamma_\phi = 0.292$ and 3.422 for SCC and ACC respectively.

The round trip phase inside the cavity is given by summing the phase contributions from various components making up the tunable VCSEL structure and is

$$2(\beta - \beta_0)L_b + 2\beta L_c + \phi_{\text{eff}} = 2\pi m \quad (3.13)$$

where L_b is the effective length of bottom mirror, L_c is the length of the cavity, and m is an integer. Substituting into Equation (3.9) and by going through some algebra, it can be shown that tuning rate near the perfect resonant wavelength is given by [7]

$$\text{For ACC} \quad \frac{\Delta\lambda}{\lambda_0} = \frac{\Delta L_g}{L_g + L_m + \gamma_\phi^{-1}(L_b + L_c)} \quad \text{and} \quad (3.14)$$

$$\text{For SCC} \quad \frac{\Delta\lambda}{\lambda_0} = \frac{\gamma_\phi \Delta L_g}{L_b + L_c + \gamma_\phi(L_g + L_m)} \quad . \quad (3.15)$$

Equations (3.14) and (3.15) are valid for tuning near the center wavelength. Due to mirror dispersion, the tuning rate changes as the wavelength moves away for the designed resonant wavelength of the DBR. The only method of determining the tuning rate across a broadband range is an optical thin film simulation based on the optical scattering matrix discussed in Section 2.6. Such a simulation is done to determine the lasing wavelength at many wavelengths and the tuning rate is calculated from the slope of the resonance wavelength vs. air gap thickness graph.

To make a fair comparison between the designs the number of DBR pairs have been adjusted to give each mirror design approximately a 99.99% reflectivity at the design wavelength. The designs all use a 2 wavelength cavity with an $\text{Al}_{0.3}\text{Ga}_{0.7}\text{As}$ spacer and two 6 nm $\text{In}_{0.2}\text{Ga}_{0.8}\text{As}$ quantum wells with 10 nm GaAs barriers. Figure 3.7 shows a calculated tuning rate versus wavelength for the three different cavity designs.

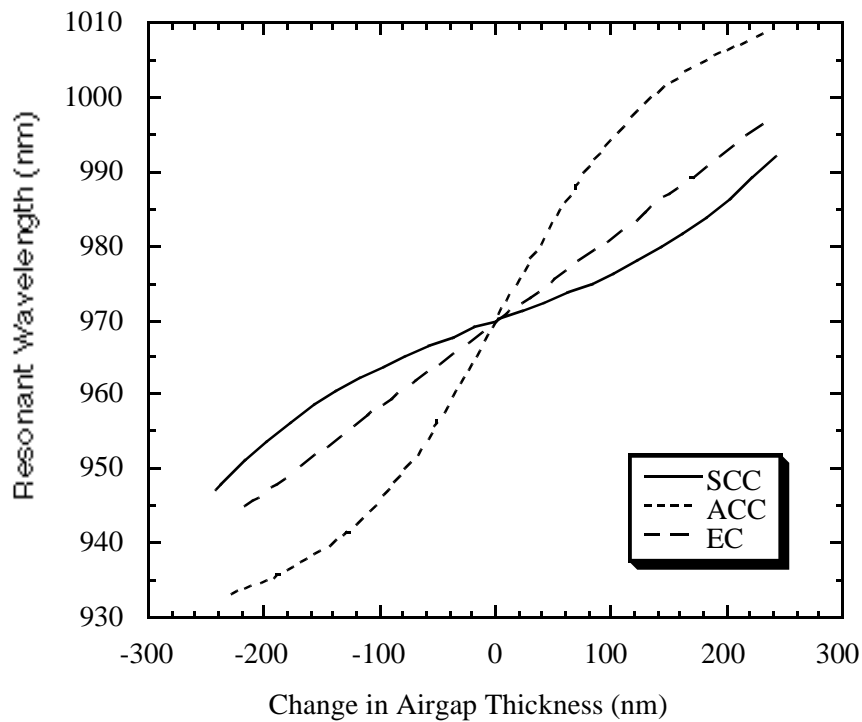


Figure 3.7: Resonant wavelength vs. air gap thickness variation near center wavelength for ACC, SCC, and EC cavity configurations. The center wavelength air gap thickness for ACC and EC is λ and for SCC is $3\lambda/4$ [8].

While the ACC has a high tuning rate and a wider tuning range there is a price to be paid. The overlap of the optical field with the quantum wells is much lower and the threshold gain is much higher. Figure 3.8 shows the required threshold gain versus tuning for the three cavity designs.

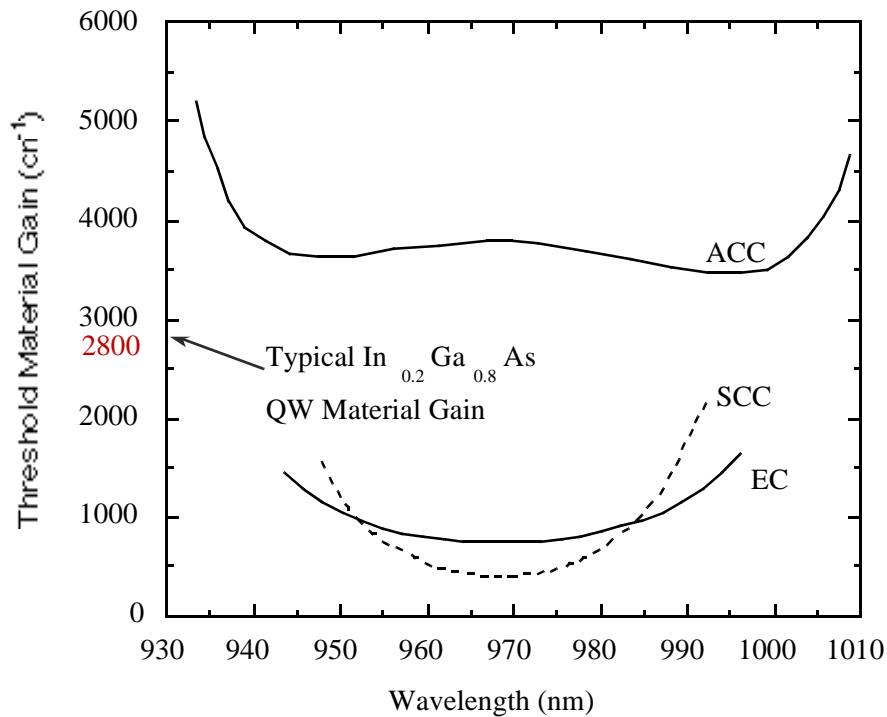


Figure 3.8: Threshold material gain vs. wavelength for ACC, SCC, and EC cavity configurations [8].

For a typical $\text{In}_{0.2}\text{Ga}_{0.8}\text{As}$ quantum well we can reliably get 2800 cm^{-1} of gain before thermal problems with excessive pump energy start to limit the performance [8]. So the ACC is not a practical design for use in the current materials system. It is also impossible to grow an antireflection layer needed in the EC design. However various compromise designs can be developed [8]. This work is focused on building larger systems using the MTVCSSEL, not simply improving device performance. So it was decided to use the SCC cavity design which has the lowest requirements for threshold gain and mirror reflectivity to get the highest fabrication yield.

3.2.2 Tuning Range

Micromachined membranes can only be pulled down 1/3 of the original gap thickness before they become unstable and collapse [35]. From that assumption and the tuning rate just calculated we can determine the tuning range for our MTVCSLS. Figure 3.9 shows the tuning range for an SCC MTVCSLS with an air cavity thickness of 1/4, 3/4 and 5/4 of a wavelength. The cavities are actually slightly thicker by a small amount, δ , so that even if the fabrication is slightly off we can tune the device to its designed resonance to reach the lowest possible threshold gain for testing.

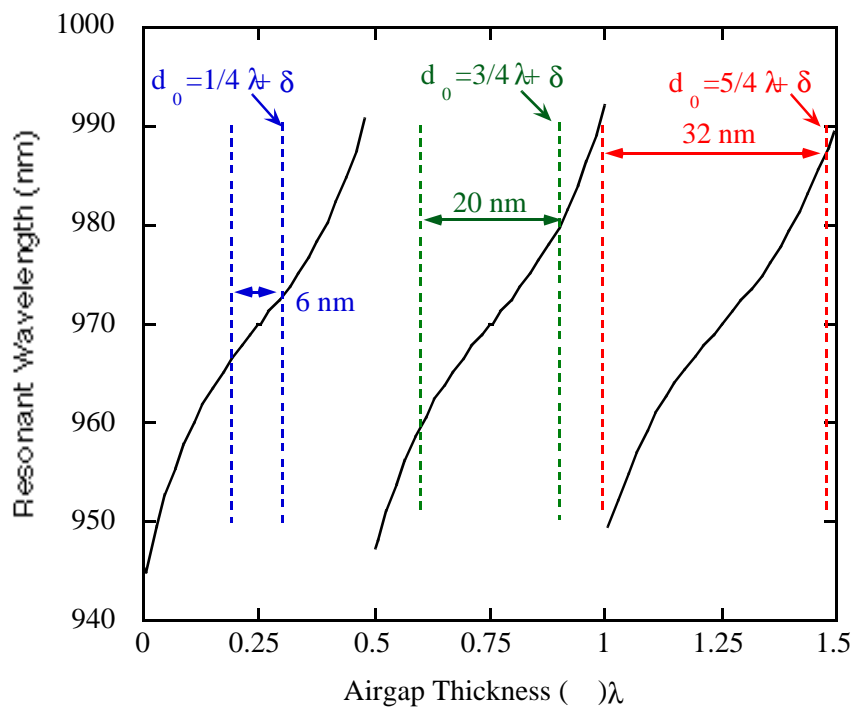


Figure 3.9: Resonant wavelength vs. air gap thickness. Shown on dotted lines are the resulting wavelength tuning range for different starting air gap thickness [8].

The chart shows that as the air gap thickness is increased the tuning range increases. It seems desirable to use the thickest gap possible, however as the total cavity length

increases the axial mode spacing decreases and eventually the tuning range will be limited by the axial mode spacing. Fabrication experience with $3/4$ wavelength cavities and concerns about excessively long growth times for longer devices caused us to choose a $3/4$ wavelength cavity for the MTVCSSELs. Additional experiments latter suggested that $5/4$ and perhaps $7/4$ wavelength devices can be fabricated with careful control of the etching procedures [44].

Chapter
4

Fabrication of MTVCSELs

Fabrication of the MTVCSSEL is a demanding process that requires a large range of equipment and technologies including: a Molecular Beam Epitaxy (MBE) system to grow the quantum wells, a wet thermal oxidation process to form the current isolation layer, a dual-frequency PECVD for depositing stress controlled dielectric layers and a MEMs technology to produce the membrane. In this chapter we will discuss the device fabrication and review some developments that were needed to achieve a high device yield. In particular we will review work on stress control in PECVD films and improvements in the design of the wet thermal oxidation system.

A schematic drawing of the MTVCSSEL is shown in Figure 4.1. The laser cavity is formed between the bottom DBR mirror and the top hybrid mirror mounted on a membrane suspended above the cavity. Inside the cavity there are a pair of quantum wells to provide the needed optical gain and an oxidation aperture to funnel the current through the lateral center of the device as aligned to the top mirror. The laser diode has the required P-contact on the surface below the air gap and N-contact on the backside of the wafer. Light is emitted through the bottom of the wafer, so the back of the wafer is antireflection coated to prevent excessive reflections from disturbing the laser operation [45].

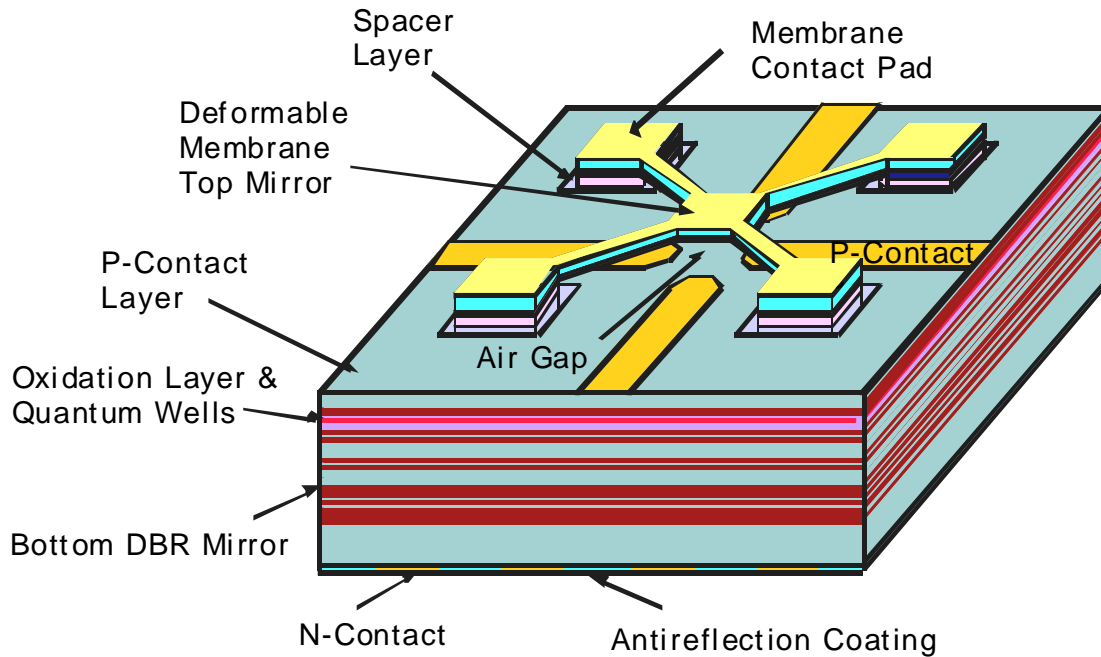


Figure 4.1: Schematic drawing of the MTVCSSEL.

4.1 Fabrication Procedure

The following section will describe the fabrication of the MTVCSSEL.

4.1.1 Step 1: MBE Growth

The first step in fabrication is the MBE growth of what amounts to a VCSEL with the top mirror replaced by a sacrificial layer for the membrane release etch and a quarter wave GaAs layer needed as an etch stop layer. The first layers grown are 22.5 pairs of an AlAs/GaAs DBR that form the bottom mirror. Then the laser cavity including two $\text{In}_{0.2}\text{Ga}_{0.8}\text{As}$ quantum wells and a $\text{Al}_{0.98}\text{Ga}_{0.02}\text{As}$ oxidation layer are grown. Finally a sacrificial layer that is slightly thicker than $3/4$ wavelength of $\text{Al}_{0.85}\text{Ga}_{0.15}\text{As}$ and a quar-

ter wavelength thick GaAs layer are grown. The top GaAs layer forms part of the membrane as well as serving as an etch stop.

4.1.2 Step 2: PECVD of top mirror and backside AR coating

The second step in the process is to deposit top mirror made of a $1/2$ wavelength mechanical layer of Silicon Nitride and a 1.5 pair Silicon Dioxide/Silicon Nitride DBR. Since the top mirror is on a membrane the layers need to be in tensile stress. The Silicon Nitride layers are grown from a special high tensile stress recipe and the Silicon Dioxide is grown from a special low compressive stress recipe. After that a quarter wave layer of low stress Silicon Nitride is grown on the backside of the wafer to serve as an antireflection coating. The details of the stress control in PECVD films will be discussed in Section 4.2.2.

4.1.3 Step 3: Current confinement etch and oxidation

During the third step a Freon 23 (CHF_3) based RIE dry etch (for the dielectric layers) and a $\text{H}_2\text{SO}_4:\text{H}_2\text{O}_2:\text{H}_2\text{O}$ 1:8:40 nonselective wet etch (for the AlGaAs layers) are used to expose the $\text{Al}_{0.98}\text{Ga}_{0.02}\text{As}$ oxidation layer using the Current Mask. The Freon 23 based dry etch is performed in a Dry-Tek 400 dry etcher. The etch uses 20 sccm of Freon 23 with 5 sccm of O_2 added to prevent scumming and runs at 100 mT where approximately 100 Watts of RF power are applied to produce a 250 Volt wafer bias. The power level is set to achieve the same wafer bias to provide improved control of the etch rate [46]. Figure 4.2 shows a schematic drawing of the MTVCSSEL after etching. The $\text{Al}_{0.98}\text{Ga}_{0.02}\text{As}$ layer is then oxidized in a steam furnace at 440°C for approximately 1 hour to leave a 5 micron

unoxidized aperture that confines current flow to the center of the device. Figure 4.3 shows an oxidized current aperture.

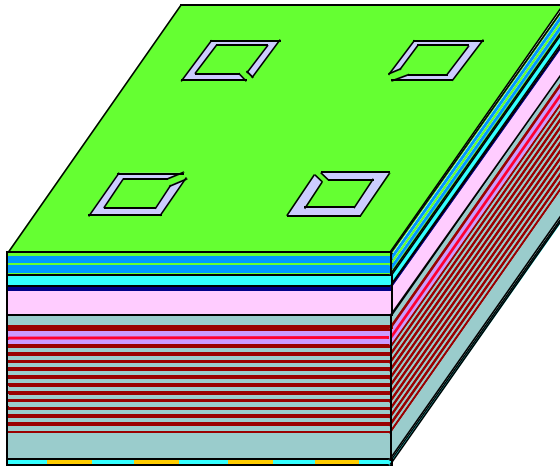


Figure 4.2: MTVCSSEL after current mask etching.

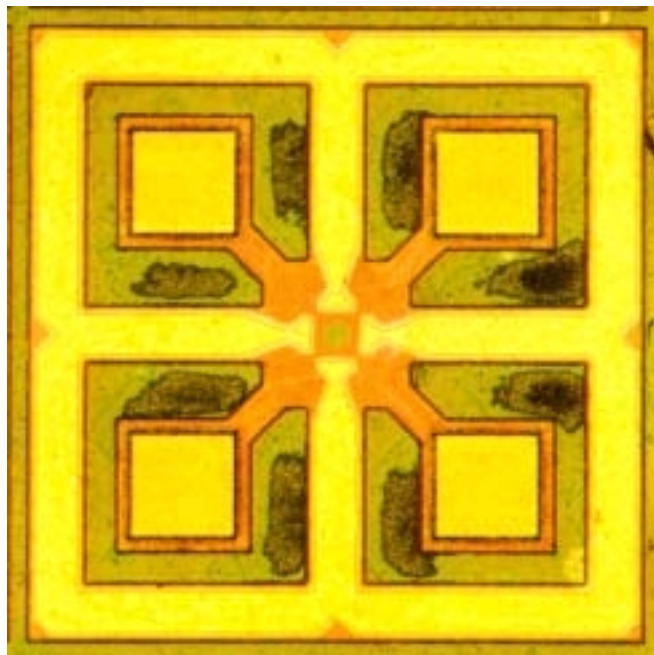


Figure 4.3: MTVCSSEL current aperture.

4.1.4 Step 4: Backside N+ Ohmic Contact

We use a simple but effective backside alignment process. First a microscope slide that is patterned with a grid of lines by exposing the Backside Contact Mask rotating it 90 degrees and exposing again. The grid is then etched for a couple of hours in 20:1 Buffered Oxide Etch to provide grooves that will accelerate the removal of the slide later. The top side of the wafer is then attached to the grooved side of the microscope slide using photoresist. After a hard bake at 120 C for 10 minutes the backside of the wafer is coated with photoresist. The Backside Contact Mask is placed upside down under a microscope and the slide is used as a handle to place the wafer with the backside down on the mask. After carefully aligning the now visible top side of the wafer with the mask, the slide is taped to the mask to prevent movement. The whole collection is then flipped over again and photoresist is exposed. The tape is removed and the slide/wafer assembly is developed. After development the same Freon 23 based dry etch is used to remove the Silicon Nitride AR layer. The sample is dipped into a 10:1 H₂O/HCl wet etch to remove any surface oxide from the GaAs wafer. The sample is then loaded into the vacuum chamber of an e-beam evaporator. An N+ contact is formed from the following series of depositions: 108 Å of Ge, 102 Å of Au, 63 Å of Ge, 236 Å of Au, 100 Å of Ni and 2000 Å Au. After a slow ramp up from room temperature (~50° C / minute) the contact is annealed for 1 minute at 405° C in an RTA and then slowly cooled back down to room temperature.

4.1.5 Step 5: Membrane Center Etching

The stiffness in the top mirror membrane is produced primarily by the tensile stress in the layers in the same manner that a trampoline is supported. Since the Silicon Dioxide layer is compressively stressed it reduces the net tensile stress in the entire membrane. Membranes that are compressively stressed have a tendency to bow. The bowing combined with the external stress of the release etch can cause the membrane to collapse and remain stuck to the wafer surface by Van der Waals forces. Therefore it is desirable to

maximize the tensile stress in the membrane by removing the compressive layers except where they are needed to form a mirror in the center of the device.

To remove the Silicon Dioxide from the membrane legs the center part of the membrane top mirror is protected with photoresist. Then the previously discussed Freon 23 based dry etch is used to remove the Silicon Dioxide layers along with the Silicon Nitride layer between them from the legs. The etch selectivity for Silicon Nitride over Silicon Dioxide is approximately three to one in this etch chemistry. Therefore the etch is interrupted regularly to measure its progress on the Dek-tek step height gauge. It is easy to overetch the structure if you do not do careful accounting for the differences in etch rate for the various layers. A Sulfur Hexafluoride etch chemistry that can give 10:1 selectivity for Silicon Nitride is available, but we lack a chemistry such as a Freon 318 (C_4F_8) that will etch Silicon Dioxide faster than Silicon Nitride. A suggested starting point might be a pressure of 40 mT with 25 sccm of Freon 318 and 200 sccm of Argon to reduce scumming and an RF power of at least 300 W. It may be necessary to add a small amount of oxygen to reduce scumming but that may increase the nitride etch rate which will reduce the selectivity. The addition of Nitrogen may improve the selectivity [46]. A schematic drawing of the structure after etching is shown in Figure 4.4.

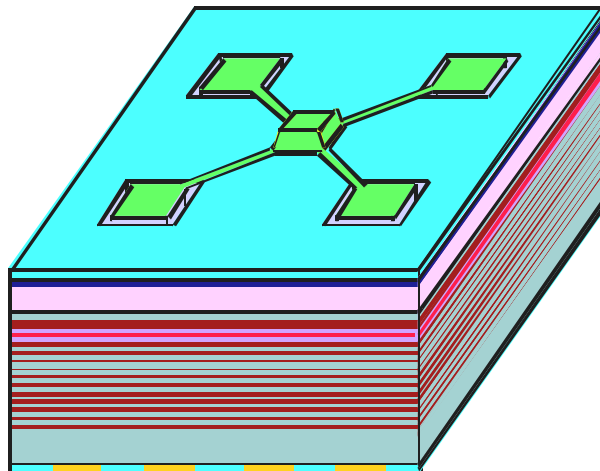


Figure 4.4: MTVCSSEL after center mask etching.

4.1.6 Step 6: Membrane Adhesion and Top Mirror Layer Deposition

Gold has a high reflectivity in the near infrared that can be greater than 99%. So by using a Gold top layer on the top mirror we get a high starting reflectance to which we add the reflectance from each DBR interface. In reality the actual reflectance of Gold depends on the thickness and deposition conditions. It is preferable to deposit a thick film of Gold $>0.25 \mu\text{m}$ at a low rate in a clean chamber to get the highest reflectivity [7]. And the reflectivity of a VCSEL mirror still needs to be significantly higher than 99% which is why we have deposited the 1.5 pairs of a Silicon Nitride/Silicon Dioxide DBR. When designing the hybrid mirror structure it is desirable to get the highest index contrast possible at each interface. The largest index contrast occurs between Gold and Silicon Dioxide, so the Gold is deposited onto a silicon dioxide layer in the mirror. However, Gold does not adhere well to most dielectrics including Silicon Dioxide.

The only certain method of obtaining reliable adhesion in deposited Gold films is to deposit it onto another metal preferably one that doesn't tarnish such as Gold. Therefore a membrane adhesion layer is deposited before the Gold top mirror layer. The membrane adhesion layer is made of a layer of Titanium to provide adhesion and a layer of Gold deposited immediately afterwards in the same vacuum chamber to prevent tarnishing of the Titanium surface.

However Titanium has a much lower reflectivity than Gold. Our technique for getting a high reflectivity from the Gold is to leave a window in the membrane adhesion layer in the center of the top mirror where the high reflectivity is needed. The width of the window is only 18 microns so the Gold in the center of the frame sticks to the dielectric and provides the needed high reflectivity.

To form the membrane adhesion layer we use an e-beam system to deposit 5 nm of Titanium and 5 nm of Gold. Figure 4.5 shows the structure after the deposition.

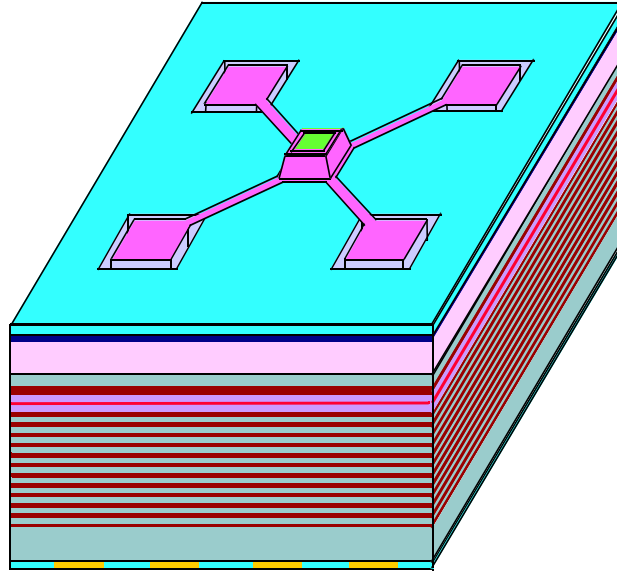


Figure 4.5: MTVCSSEL after membrane adhesion layer deposition.

The top mirror layer is 250 nm of e-beam deposited Gold. Figure 4.6 shows the structure after the deposition.

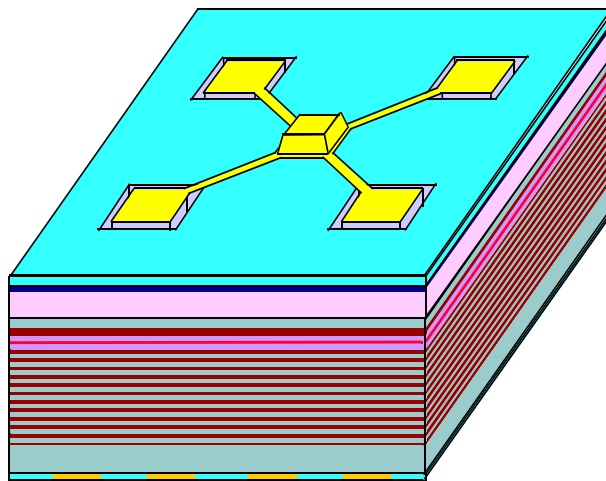


Figure 4.6: MTVCSSEL after top mirror layer deposition.

4.1.7 Step 7: Membrane Etch

The membrane is etched away to expose the sacrificial layer that will be removed in a later step to release the membrane. In fact it is desirable to etch part way through the sacrificial layer so that the photoresist will form a scaffolding to help support the membrane during the release etch step [7]. Based on some experiments it appears for the current design it is optimal to etch through the sacrificial layer until only about 300 nm are left [44].

The first step is to etch away the remaining dielectric layers with the Freon 23 dry etch mentioned above. The next step is to dry etch the GaAs top mirror layer and part of the $\text{Al}_{0.85}\text{Ga}_{0.15}\text{As}$ sacrificial layer in a Plasma-Quest ECR-RIE chamber. It is desirable for this etch to be as anisotropic as possible and the best recipe after several experiments [47] consists of gas flows of 75 sccm Argon, 50 sccm of BCl_3 , 5 sccm Cl_2 , with 400W of microwave power, 50W of chuck RF power, with a process pressure of 5mT and a chuck temperature of 20°C. The etch has an initiation time that varies between 20 and 40 seconds for the top surface. The etch rates for the GaAs and the AlGaAs layers are slightly different. This makes timing and measuring the etch rate critical. It is necessary to stop the etch at least twice to determine the etch rate. The first time to stop the etch must be after the random initiation delay and the top layer of GaAs have been etched away. The second time is usually 1 minute later. After determining the etch rate it is desirable to etch 90% of the remaining distance and then stop to recalibrate the etch rate and prevent over etching. The total etch time is about 5 minutes and the photoresist etches at a rate of 1200 nm per minute. This requires a thick layer of photoresist in order to protect the Gold top mirror layer. During some process runs depending on the thickness of the dielectric layers that have to be etched in this step it is necessary to strip the photoresist after the dielectric etch and pattern a fresh layer before the GaAs/AlGaAs etch step. Figure 4.7 shows the MTVCSSEL after the membrane etch.

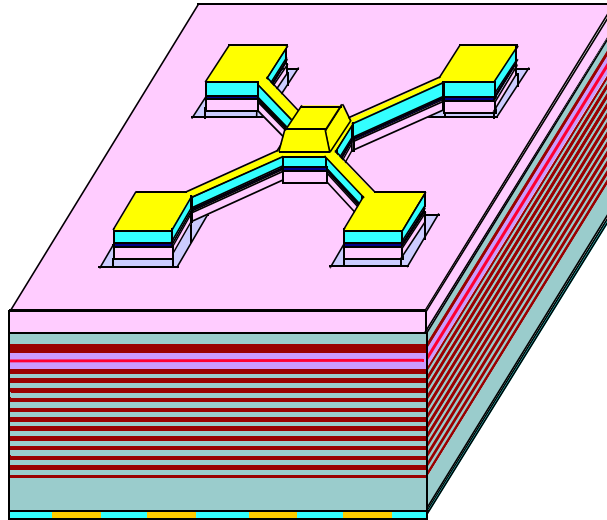


Figure 4.7: MTVCSSEL after membrane etch.

The etch process was not hard to control, but taking that many measurements was time consuming. A better solution would be to use optical emission spectroscopy to determine when the etch reached different layers. Some experiments of this type were performed on a series of dummy samples. The Gallium emission line at 417.2 nm was visible, but the Aluminum line at 396.1 nm did not appear so it was not possible to use optical emission spectroscopy as a reliable diagnostic for this etch. There is an ultraviolet emission line from AlCl_3 , but the Pyrex window was absorbed it. A quartz window was ordered and installed to look for the AlCl_3 line, but the window did not arrive until after the processing was done.

4.1.8 Step 8: Membrane Post Recess Etch

The $\text{Al}_{0.85}\text{Ga}_{0.15}\text{As}$ sacrificial layer will be removed from under the membrane during the release etch. However it will still form part of the membrane post. A photoresist layer is used to protect the $\text{Al}_{0.85}\text{Ga}_{0.15}\text{As}$ layer that makes up the membrane post during the release etch. It is necessary to prevent undercut during the release etch from etching the

$\text{Al}_{0.85}\text{Ga}_{0.15}\text{As}$ layer in the post. To do this a trench is etched next to the post for approximately 100 nm into the cavity so that the $\text{Al}_{0.85}\text{Ga}_{0.15}\text{As}$ layer in the post will be completely covered with photoresist during the release etch and not exposed to the etchant solution. The trench is etched with the same Plasma-Quest ECR-RIE process used in the membrane etch step above and with the same precautions as above when measuring the etch rate.

4.1.9 Step 9: Cavity P+ Ohmic Contact

A P+ contact must be placed on the top of the cavity. After lithography with the cavity contact mask a highly selective wet etch is used to etch through the $\text{Al}_{0.85}\text{Ga}_{0.15}\text{As}$ sacrificial layer and stop on the GaAs which forms the top layer of the cavity. The etchant is a 1:1 solution of HCl and H_2O heated to 40°C inside a beaker placed on a silicon foam pad in an heated ultrasonic water bath. The silicon foam pad is used to damp the vibrations from the ultrasonic bath which are too powerful even on the lowest setting. To perform the etch the wafer is placed in the bath and the ultrasonics are turned on for 5 seconds and then for 1 second every 10 seconds until the etch is completed approximately 2 minutes later. The completeness of the etch can be assessed under a microscope by viewing the region of the cavity contact and assuring that the surface is smooth and clean. After rinsing and drying a P+ ohmic contact consisting of 15 nm of Titanium and 150 nm of Gold are deposited by e-beam evaporation. Figure 4.8 shows the MTVCSSEL after the cavity contact deposition.

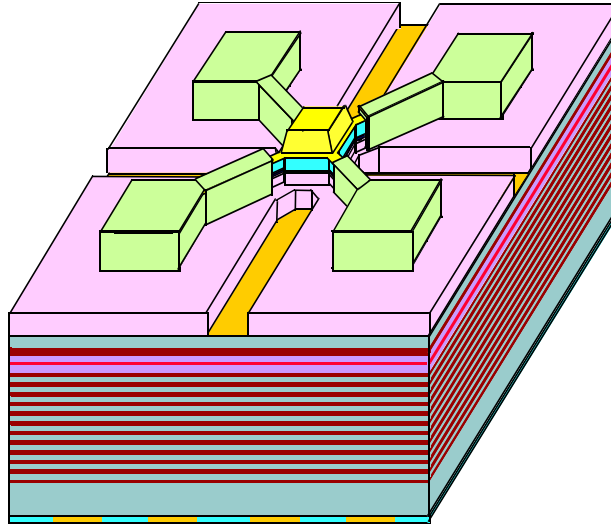


Figure 4.9: MTVCSEL before release etch.

Figure 4.11 shows a schematic diagram of the MTVCSEL after processing is complete.

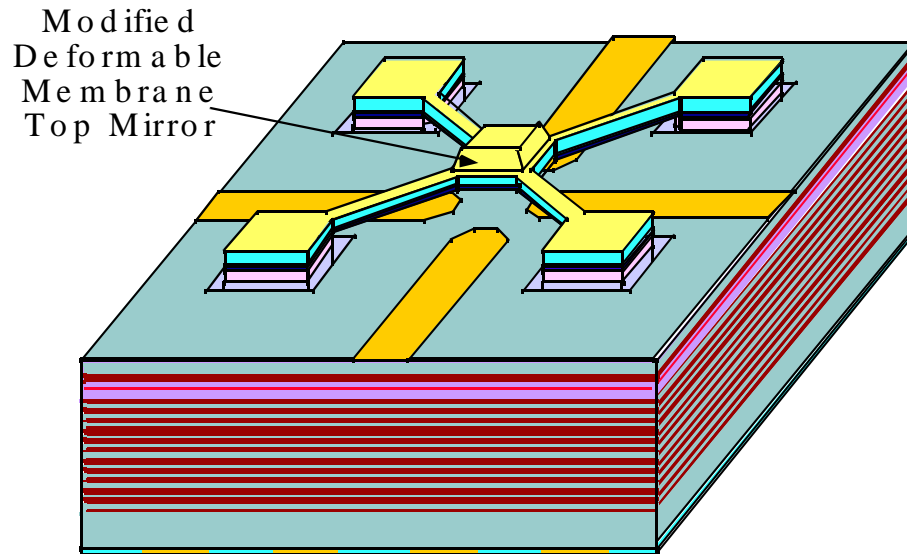


Figure 4.10: Schematic of a tunable VCSEL with thicker central reflector and thinner membrane legs.

Figure 4.11 shows an SEM photograph of a release MTVCSSEL and Figure 4.12 shows a microscope photograph of the completed device.

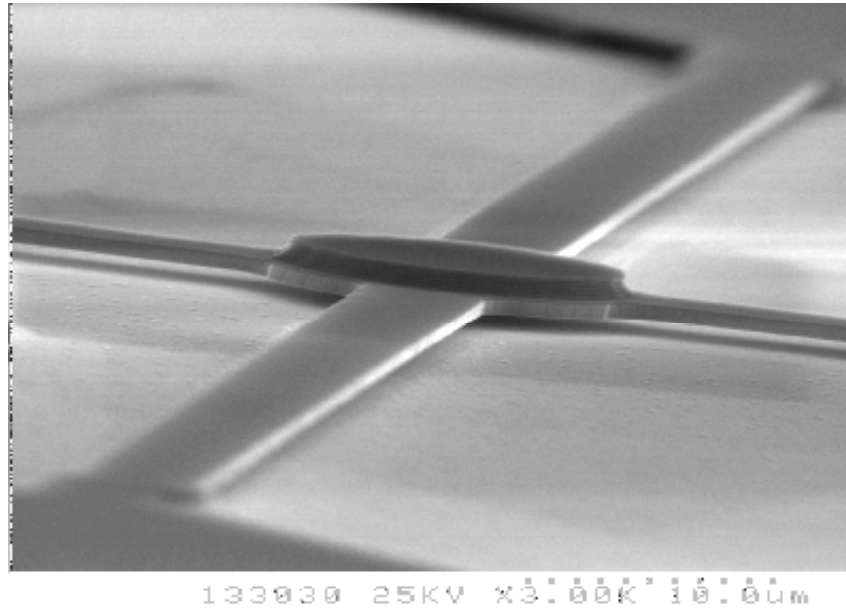


Figure 4.11: SEM image of a tunable VCSEL.

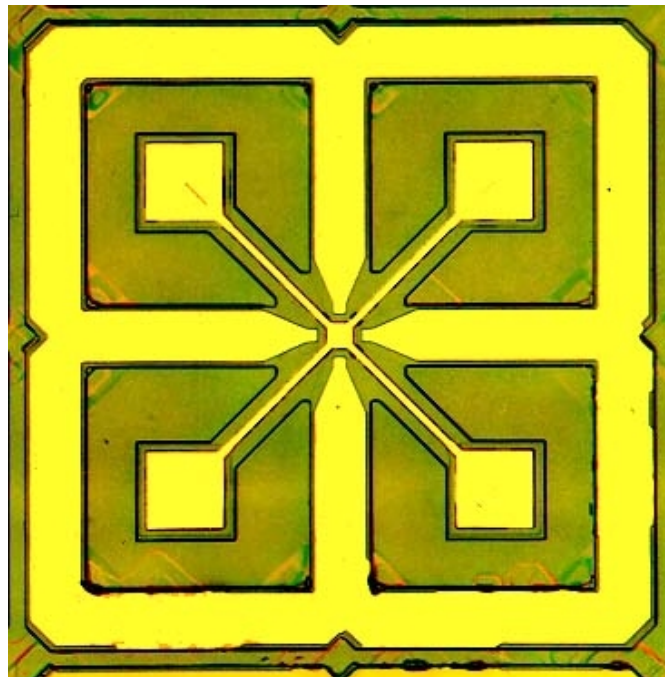


Figure 4.12: MTVCSSEL after cavity contact.

4.2 Process Development

In order to successfully fabricate MTVCSLS with a high device yield several improvements had to be made to the process flow as described in a previous work at Stanford [8]. In that work an oxidized AlAs layer was used to form the current aperture. Oxidized AlAs is known to be unstable to subsequent thermal processing, but adding a small fraction of Ga to the layer allows the device to survive additional thermal processing [48]. Section 4.2.1 details the development of AlGaAs oxidized apertures. The device also relies on tensile stress in the membrane to prevent collapse during the wet etch membrane release. The measured tensile stress in the Silicon Nitride layers was below 100 MPa and the compressive stress in the Silicon Dioxide layers was above 400 MPa which prevented the design of an effective strain balanced DBR. Section 4.2.2 details the development of PECVD recipes need for stress control in Silicon Nitride and Silicon Dioxide films.

4.2.1 Oxidation of AlGaAs layers

Holynak and coworkers accidentally discovered that AlAs would oxidize rapidly in a high temperature water vapor environment during their studies of degradation in AlGaAs caused by atmospheric water vapor [49]. The original intention of their study was to measure the degradation rate at elevated temperatures in order to determine an activation energy for the atmospheric hydrolyzation process that often destroys AlAs layers. The oxide they produced from formed a smooth surface instead of the cracked layers that were formed by atmospheric degradation. The work has been repeated by many groups and the process and materials issues relating oxidized AlGaAs layers have received a large amount of study [48].

The performance of VCSELs has been significantly improved by oxidation since it provides two benefits; the oxide layer forms an aperture which confines current flow to the center of the VCSEL reducing leakage and surface recombination currents, the oxide layer also forms an intracavity lens which decreases the scattering losses of the optical mode. Oxide aperture VCSELs have achieved greater than 50% wall plug efficiency and

single mode operation for several milliwatts of output power[59]. There are several other devices that can benefit from an oxidation isolation process e.g. high frequency transistors [60].

4.2.1.1 Oxidation System

Figure 4.13 shows a typical oxidation setup. A carrier gas, in this case nitrogen, is passed through a bubbler filled with DI water and into a wafer furnace where the oxidation reaction occurs. The bubbler is placed in a heated water bath to maintain a constant high temperature. The rate of nitrogen flow is controlled with a standard MFC and the line between the bubbler and the furnace is heated to prevent condensation of the saturated vapor.

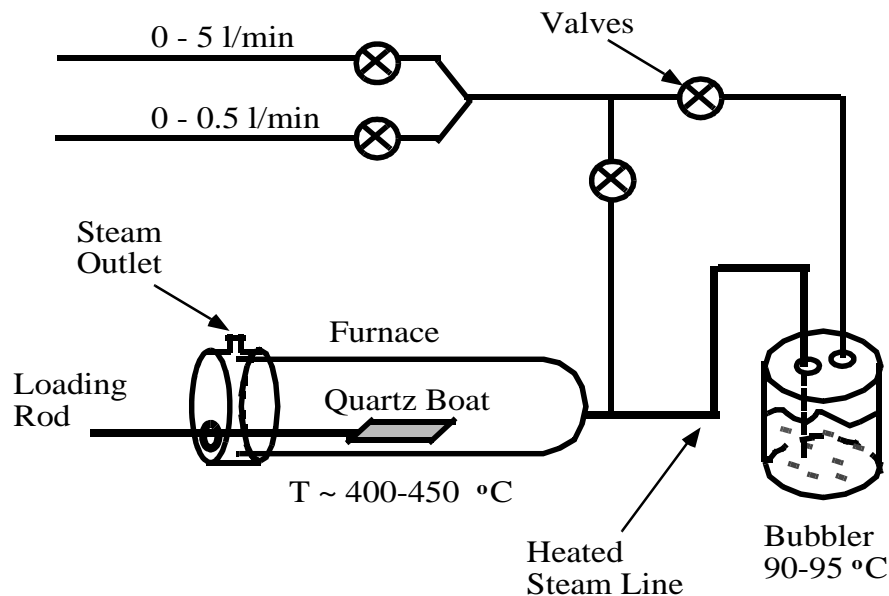


Figure 4.13: Schematic drawing of a typical AlGaAs oxidation furnace.

Fabrication of MTVCSSELS required oxidizing in 50 microns from a mesa and stopping within a one micron range. In order to achieve the required one percent control of the oxidation rate a number of steps had to be taken to insure repeatable oxidation results. Since the furnace was manually loaded, the load and unload feed rates had to be timed to

insure a repeatable amount of total oxidation time. The water vapor in the furnace had to be fully saturated, so a preconditioning process of flowing the carrier gas through the bubbler and furnace for 2 hours before loading the first sample insured that the furnace was fully saturated with water vapor and that all temperatures had stabilized. This process also had the important side benefit of reducing the dissolved oxygen in the water. Other researchers have observed that less than a one percent flow of oxygen in the carrier gas can slow and even stop the oxidation process [48]. Following nitrogen through the heated water will reduce the amount of dissolved oxygen in it and produce the stale water needed for repeatable oxidation results. Since the oxidation is a thermally activated process with the typical exponential dependence on temperature the temperature profile of the furnace was mapped and the samples were consistently loaded at the point of maximum temperature and lowest slope. It was impossible due to limitations in the design of furnace to achieve a flatter temperature profile than the measured results shown in Figure 4.14.

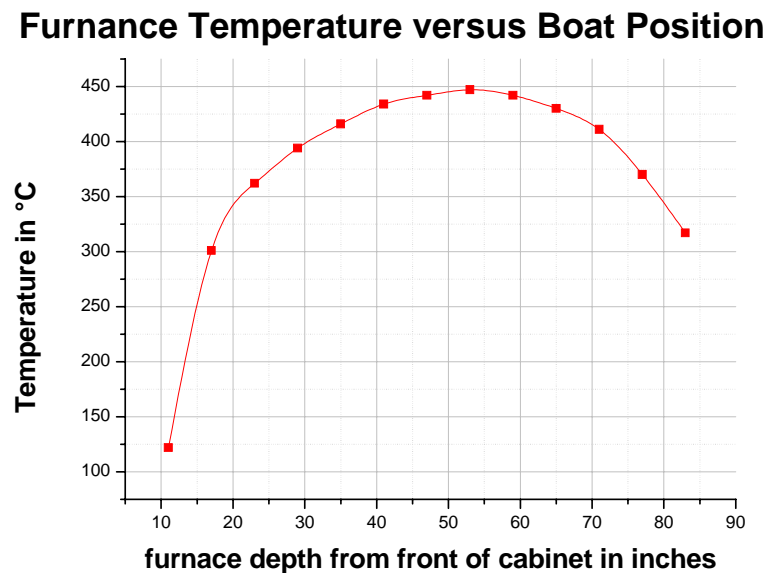


Figure 4.14: Furnace temperature versus position.

The previous oxidation furnace setup had not been tested for water vapor saturation and in fact the oxidation rate was limited by the arrival of water vapor at the surface and not the reaction temperature. A series of runs were done in the rebuilt oxidation system to insure that the carrier gas flow rate was high enough to saturate the reaction with water vapor. The results of this experiment shown in Figure 4.15 where the oxidation distance for a fixed time is plotted versus carrier gas flow rate. The results show that a carrier gas flow of about 2 slpm will saturate the oxidation rate. The previous carrier gas flow rate had been about 0.5 slpm which was too small and the reaction that occurred was similar to the atmospheric degradation process in AlGaAs resulting a weak porous oxide.

Oxidation Distance versus N₂ Flow at 438°C

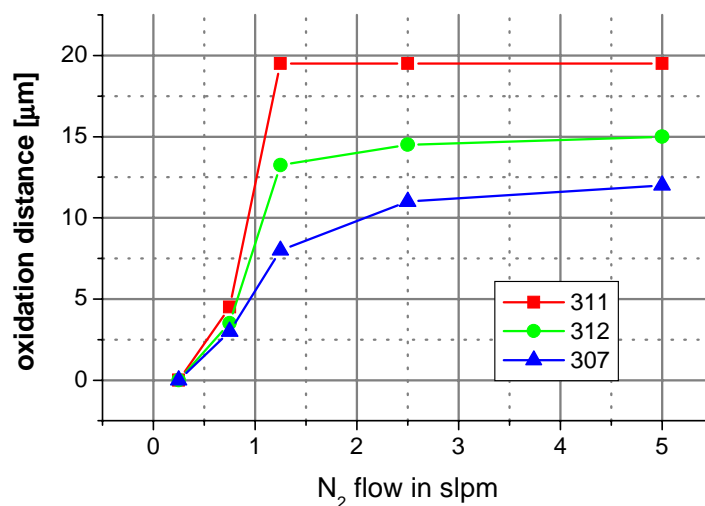


Figure 4.15: Oxidation distance versus carrier gas flow rate.

The oxide formed at low flow rates under diffusion limited conditions had an irregular oxidation front due to local variations in the etched surface and was mechanically weak to the point that it failed the scotch tape test and often peeled during subsequent processing. The oxide formed at higher flow rates under reaction rate limited conditions had a much smoother front and was mechanically stronger. It survived the scotch tape test, additional

processing and mechanical contact from the electrical probes. The scotch tape test is a simple test of layer adhesion where a piece of clear tape is attached to the surface and removed. If the layer peels off with the tape then the adhesion is too weak to for additional processing.

In the reaction rate limited regime the oxidation rate was only a function of the material composition of the AlGaAs layer and the thickness of the layer. Therefore reaction rate limited oxidation rate did not vary from day to day. The oxidation rate for the diffusion limited case could vary several percent from day to day. Example test oxidation samples from the diffusion and reaction rate limited are shown in Figure 4.16. The results here confirm the known facts that oxides formed under diffusion limited conditions such as those in the old furnace or in atmospheric degradation are weak and unstable, but that an oxide grown under reaction rate limited conditions can be used in active devices.

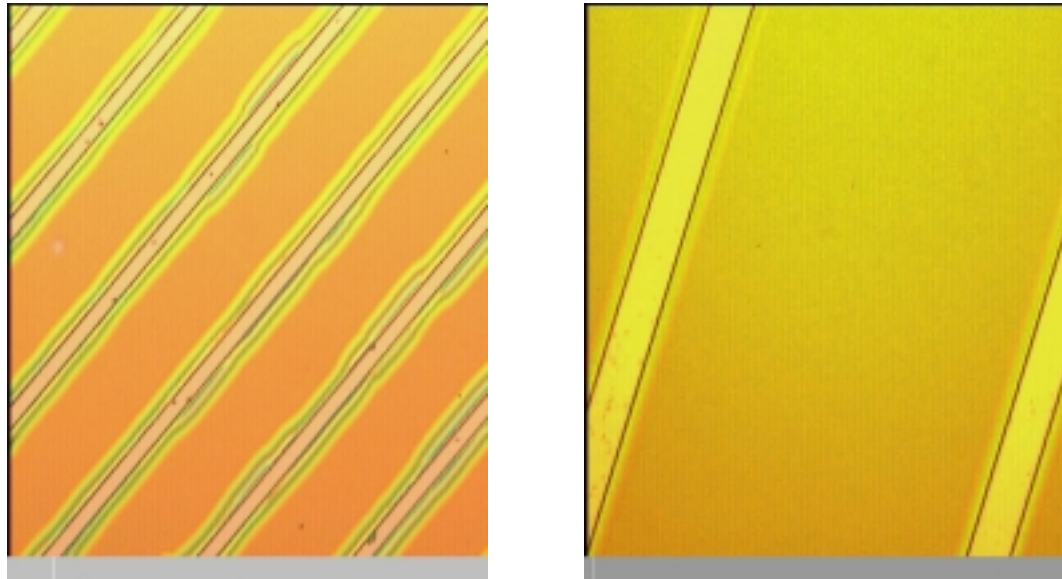


Figure 4.16: Oxidized Samples of AlGaAs, Diffusion Limited (Left), Reaction Limited (Right).

The original oxides where formed from AlAs, which is unstable to additional thermal processing. In our experiments the AlAs oxidation always occurred in the diffusion rate

limited regime. The addition of a few percent of Gallium to the oxidation layer slows the reaction rate such that the oxide always forms in the reaction rate limited regime. Other researchers have also suggested that adding a few percent Gallium greatly reduces the stress in the oxide. Device lifetimes are significantly longer for oxides containing a few percent Gallium [48]. The only remaining challenge in designing an oxide aperture for the MTVCSSEL is to model the oxidation rate as a function of thickness and temperature for the chosen AlGaAs composition.

4.2.1.2 Oxidation Rate

A study of oxidation rate as function of layer thickness was done at the University of Santa Barbara by Naone and Coldren for AlAs layers[61]. However the scale of the results may not be directly applicable to AlGaAs with a few percent of Ga as the stress in the oxide is much lower and that is known to change reaction kinetics [65]. The reaction rate will decrease rapidly below a certain thickness due to the capillary effect. This thickness may depend on the stress level in the material. A series of runs of different thicknesses of $\text{Al}_{0.97}\text{Ga}_{0.03}\text{As}$ were done for different times at different temperatures to extract a model of the oxidation rate. The first step was to extract the oxidation rate for a given thickness and temperature as shown in Figure 4.17

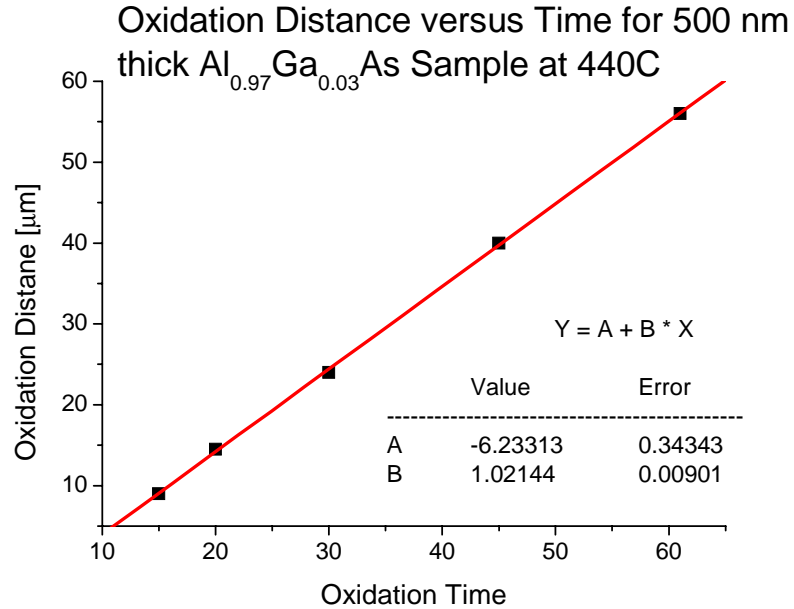


Figure 4.17: Oxidation rate for a 500 nm layer of $\text{Al}_{0.97}\text{Ga}_{0.03}\text{As}$ at 440°C.

The results for all of the samples of this experiment are shown in Table 4.1.

Oxidation Rate $\mu\text{m}/\text{min}$	Temperature			
	380°C	400°C	425°C	440°C
Layer Thickness				
12.5 nm	0.0248	0.0450	0.167	0.267
25 nm	0.0589	0.122	0.425	0.747
50 nm	0.0883	0.185	0.575	1.021
100 nm	0.0917	0.192	0.581	1.032

Table 4.1: Oxidation rate for $\text{Al}_{0.97}\text{Ga}_{0.03}\text{As}$ versus temperature and layer thickness.

The results from Table 4.1 were fit using Naone's model [61] to obtain the activation energies and reaction rate coefficients for $\text{Al}_{0.97}\text{Ga}_{0.03}\text{As}$. The results for the activation energy are shown in Figure 4.18 and for the reaction rate coefficient are shown in Figure 4.19.

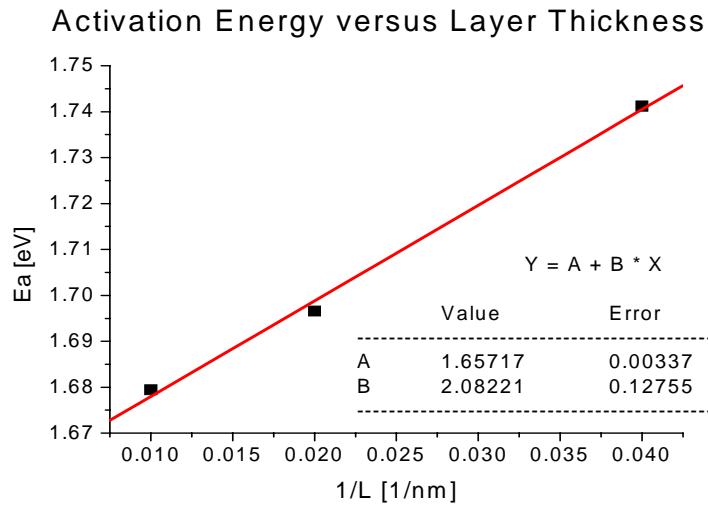


Figure 4.18: Activation energy versus layer thickness.

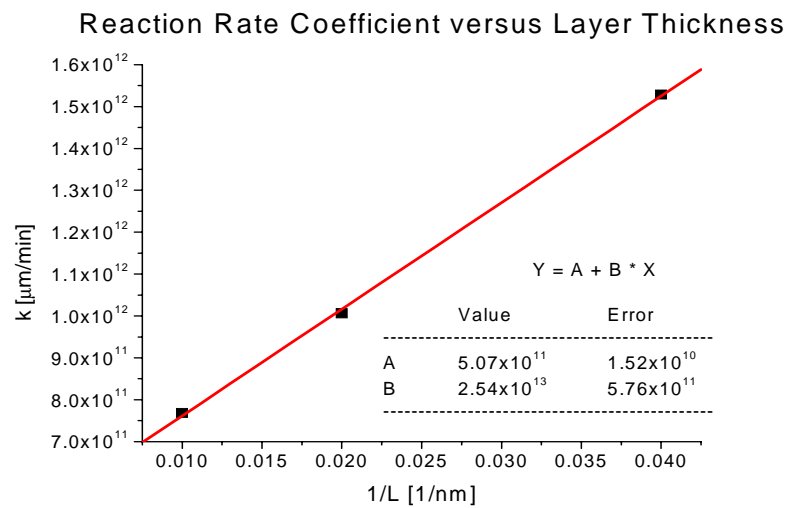


Figure 4.19: Reaction rate coefficient versus layer thickness.

The model from [61] shows that both the reaction rate coefficient and the activation energy show a dependence on the layer thickness. The reaction rate in $\mu\text{m}/\text{min}$ is given Equation (4.1) for a layer thickness L in nm and a temperature kT in eV .

$$R(T, L) = \left(5.07 \cdot 10^{11} + \frac{2.54 \cdot 10^{13}}{L} \right) \exp \left(\frac{-\left(1.657 + \frac{2.082}{L} \right)}{kT} \right) \quad (4.1)$$

Plotting the data of Table 4.1 versus the model of Equation (4.1) produces Figure 4.20.

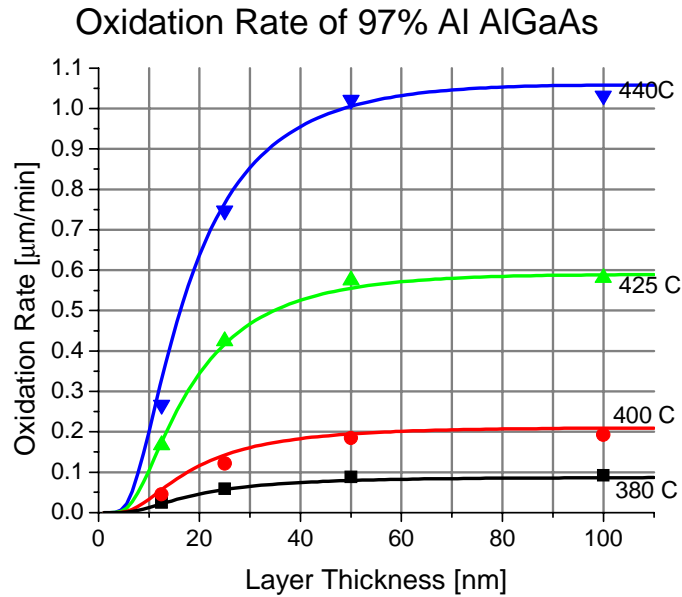


Figure 4.20: Oxidation rate in $\text{Al}_{0.97}\text{Ga}_{0.03}\text{As}$.

The model allows us to design an oxidation layer thickness that is compatible with the rest of our processing requirements. In particular the furnace has a limited run time before it runs out of water in the bubbler, approximately 8 hours, and it is desirable to run calibration samples before running the final samples. Additionally, we have observed evidence of degradation in the adhesion between the Silicon Nitride layer and the GaAs surface after long oxidation runs of greater than 1 hour. The degradation was probably due to pin-

holes in the Silicon Nitride. The result is usually a discolored circular spot at each pinhole and after 4 hours of oxidation at 440°C the circles start to overlap significantly which greatly reduces the adhesion between the PECVD film and the GaAs surface. Therefore we prefer to use an oxidation time in the region of one hour or less to prevent an excessive area of defects from building up. The shortest oxidation time is defined by the loading time of the furnace and that takes approximately 1 minute, so the shortest reasonable oxidation time is approximately 10 minutes. The highest temperature used was 440°C because at 460°C the GaAs surface exposed in the trenches started to show significant degradation and the oxidation distances were no longer a linear function of time indicating that the reaction was again diffusion limited and would produce poor quality oxides.

4.2.2 Stress control in PECVD Silicon Nitride and Silicon Dioxide

Since the PECVD deposited layers of Silicon Nitride and Silicon Dioxide form a significant portion of the micromachined membrane layer's thickness it is important to control the stress in them to insure an overall tensile stress state in the membrane to prevent collapse during the wet etch release step. The purpose of the top membrane in the MTVCSSEL is to form a high reflectance DBR mirror. In order to accurately deposit quarter wave layers the index of refraction and the growth rate have to be controlled. Additionally, it is desirable to have a low density of pinhole defects in the material, however that seems to be primarily a function of cleanliness in the chamber.

PECVD deposited films contain a significant amount of Hydrogen, often in the region of 10%, so the material deposited is not stoichiometric Silicon Nitride or Silicon Dioxide. The materials deposited in a PECVD process are usually referred to as $\alpha\text{:Si}_x\text{N}_y$ and $\alpha\text{:Si}_x\text{O}_y$. All references in this work to either Silicon Nitride or Silicon Dioxide refer to PECVD deposited films. In a porous polycrystalline film like the ones deposited by PECVD many variables can affect the material's properties. A Surface Technology Systems PC-310 PECVD reactor was used to deposit all of the films. The PC-310 allows control over the following variables in the reaction: gas flow rates, chamber pressure, hot plate temperature, RF power and RF frequency either high or low.

Typically a Design of Experiment series is run to determine the optimum operating conditions for a process. However, it is always useful to reduce the number of variables as much as possible and six variables required too many experiments to complete a DOE in a feasible period of time on the shared equipment in the cleanroom. After consulting with STS [66] and others [67] it was determined that the primary variables of interest are temperature, pressure, and RF power. The other variables are fixed. The ratio of the reactant gas sets the chemistry of the deposited layer. Changing the ratio could result in a non-stoichiometric film. Such a film which would not have a controlled index of refraction and may be optically absorbing. Both changes in the film's properties will reduce the reflectance of the top mirror. In Silicon Nitride it is known [68] that implantation of free reactants from the plasma drives the stress compressive, so it is clear that we want to use a high frequency RF source, one that oscillates faster than the ions in the plasma can respond. This will minimize their kinetic energy. For Silicon Dioxide the choice is not as clear, so both high and low frequencies were tested.

4.2.2.1 Silicon Nitride

PECVD deposited Silicon Nitride can be either tensile or compressive, it is desirable to produce as high of tensile stress as possible for the membrane release. PECVD Silicon Nitride is deposited in a 3 dimensional form as shown in Figure 4.21. The four zones in order from plasma, surface, condensation to bulk film represent the phases of Silicon Nitride deposition. The surface of the film is a rough scaffolding of Silicon Nitride with some of the Silicon and Nitride atoms still attached to their precursor gases. In the condensation zone, the precursor gases evaporate and the crosslinking between Silicon and Nitrogen atoms forms the bulk film. The condensation zone is the important zone for stress control. After the gases evaporate from the condensation zone the new bonds that form between Silicon and Nitrogen atoms are in tensile strain because they must stretch to cover the region previously occupied by the precursor gases. Therefore the natural state of PECVD deposited Silicon Nitride would be in tensile strain. However, there is very little material in the surface zone to shield the condensation zone from the plasma. A low

energy Silicon or Nitrogen atom can be implanted from the plasma into the space previously occupied by the precursor gas in the condensation zone. The implanted atom will now form compressively strained bonds since it is occupying a region that is smaller than desired. The stress state of PECVD deposited Silicon Nitride is therefore highly dependant on the plasma conditions.

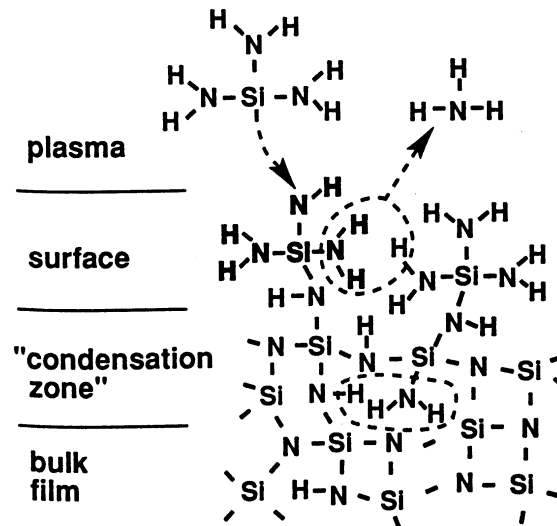


Figure 4.21: Growth regions in PECVD Silicon Nitride [68].

For PECVD of Silicon Nitride in the STS PC 310 the results showed that decreasing the pressure and RF power increased the tensile stress. Changing the temperature had no effect on the stress. The vacuum pumps on the system did not have a high enough pumping speed to reach process pressures below 600 mT, however by reducing both reactant gas flow rates the system was about to reach 450 mT. Below 500 mT the tensile stress did not increase significantly so that was the pressure used. As RF power was reduced below 11 Watts the plasma did not start reliably and the deposition rate was very low even when it did start, so 11 Watts was chosen for the RF power. As a note, the autotuning algorithm on the STS PC 310 is not very robust prior to plasma ignition. During startup, the tuning elements are simply scanned from the specified setting to a lower setting until a decrease in reflected power is detected. Therefore, it is important to set the tuners to a value close to

but slightly higher than the optimum tuning point. Choosing a good starting point for the auto tuner is especially important at low RF powers as the plasma will not ignite if the tuning is significantly mismatched. The results of this work was an increase of tensile stress from 125 MPa to 240 MPa, while all of the other material measured parameters were unchanged.

4.2.2.2 Silicon Dioxide

PECVD deposited Silicon Dioxide is usually compressive. Silicon Dioxide is deposited in a layer by layer fashion rather than the 3 dimensional fashion of Silicon Nitride, so it is not expected that the stress state will be as easily controlled. Recently there have been some reports of very low stress PECVD Silicon Dioxide, but they require novel reactor chamber geometries [72-73]. So the goal for this process development was to reduce the stress as much as possible. Again pressure effected the stress level. However, temperature, RF power and frequency had no effect. As the pressure was increased the compressive stress decreased. Above 800 mT the films showed a significant bull's-eye pattern due to non uniformities in the plasma, increasing the flow rate of the reactant gases while keeping the same ratio allowed the pressure to be increased to 850 mT but the Siliane MFC was set at it maximum value and further increases where not possible. These improvements decreased the compressive stress from 420 MPa to 280 MPa.

Chapter

5

Micromachined Tunable VCSELs

As discussed in Chapter 3, VCSELs have a very short cavity compared to other semiconductor lasers making it possible to tune them over a broad range just by changing the length of the cavity. The length is controlled by moving the top mirror which is mounted on a micromachined membrane. For the MTVCSEL as well as most other integrated semiconductor lasers the mirrors form a planar-planar optical resonator. The optical mode in a planar-planar resonator is metastable and in such resonators it is usually necessary to place an aperture in the cavity to achieve single mode operation. The oxidized $\text{Al}_{0.97}\text{Ga}_{0.03}\text{As}$ layer is used as a dielectric aperture in the MTVCSEL to produce the desired single mode operation for use in a WDM system.

5.1 Design

5.1.1 Aperture

The effect of intracavity apertures have been studied by many [74-88]. The results of Coldren et al show that a thin oxidized layer does more than serve as a mode size limiting aperture. Because of the radial variation of refractive index in the oxidized layer it also functions as a lens [74]. This is especially true in the case of thin layers where the capillary effect causes the profile of the oxidation front to be rounded. Others [76] have numerically simulated the properties of an ideal intracavity aperture and its effects on the threshold of the lowest order mode and the next highest. These results are very useful when designing a device for single mode operation.

The results show that there is a significant difference between the case of a thin aperture located at an antinode versus a node in the standing wave field pattern of the optical mode. Figure 5.1 shows the aperture at a node and Figure 5.2 shows the aperture at an antinode in the standing wave field [76].

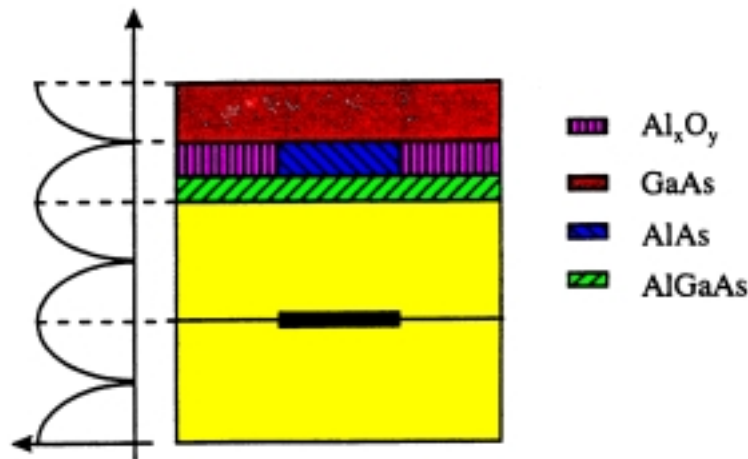


Figure 5.1: Aperture at a node in the standing wave pattern [76].

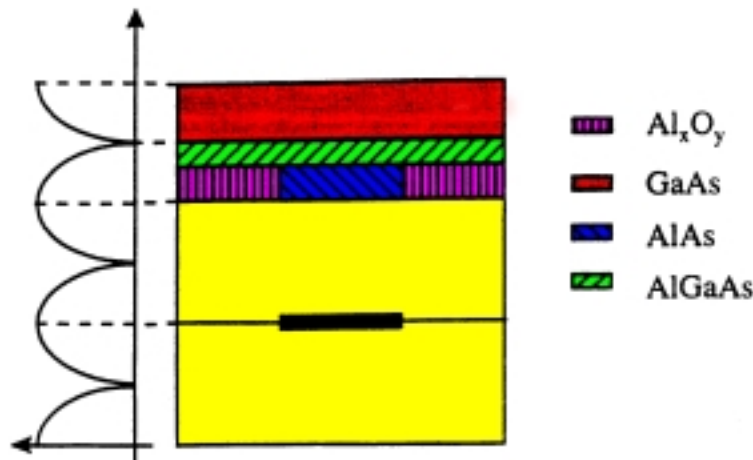


Figure 5.2: Aperture at an antinode in the standing wave pattern [76].

Single mode operation occurs when the threshold for the lowest order mode is lower than that of any higher order modes. The difference between the thresholds of the lowest and next highest order mode will then determine the side mode suppression ratio. For

VCSELs there is very little selection between transverse modes from the gain medium so any selectivity has to be created by differences in loss for the modes. In fact the gain profile may favor higher order modes because of current crowding. This effect is worse in intracavity contacted devices like the MTVCSSEL. An oxide located at a standing wave antinode has a large overlap with the electric field and functions as a very strong lens whose focusing compensates for diffractive losses caused by the aperture [74]. An aperture located at a standing wave node has less overlap with the electric field and forms a weaker lens. In this case higher order modes will suffer from significantly higher losses than the fundamental mode. Figure 5.3 [76] shows the difference in gain between the fundamental and the next highest order mode for both cases for a 5 μm aperture. The results indicate that the aperture should be placed at a node in the standing wave field and that it should be thinner than 50 nm.

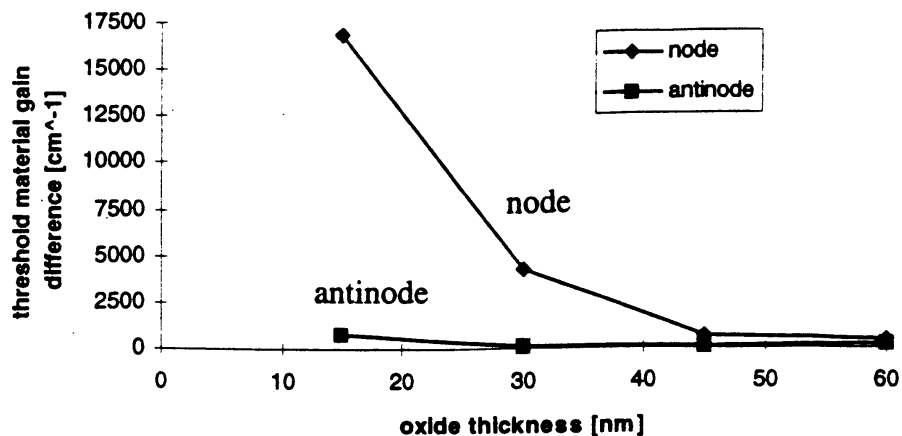


Figure 5.3: Difference in threshold gain between the fundamental mode and the next higher order mode for a 5 μm in diameter aperture [76].

The total length of the gain region in VCSELs is just the thickness of the quantum wells, so it is important not to introduce too much excess loss or the single mode device can easily become a no mode device. Figure 5.4 [76] shows the threshold gain versus the thickness of the oxide layer and the diameter. The results suggest that oxide thicknesses below 30 nm and aperture diameters below 4 μm start to show excessively high threshold

gains. In the final design we chose a 50 nm thick oxide layer and a 5 μm diameter aperture to achieve low threshold single mode operation. The oxide was slightly thicker than would be desired due to processing considerations as explained in Chapter 4.

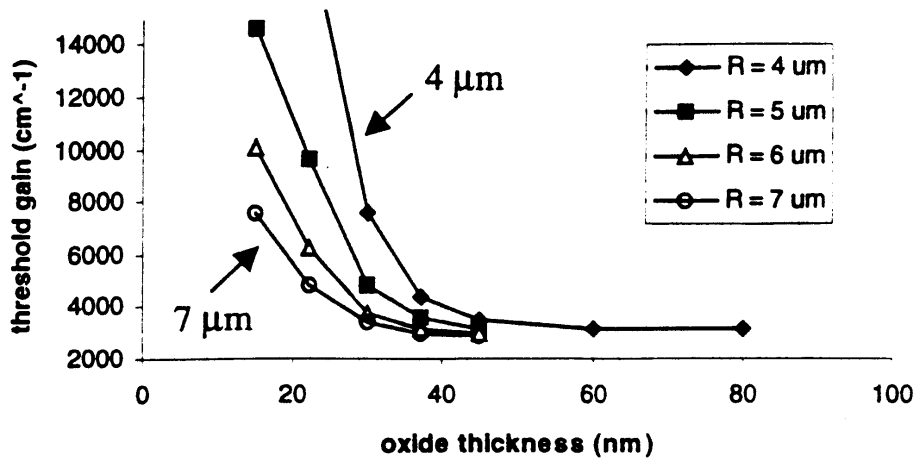


Figure 5.4: Threshold gain for an oxide aperture at a node [76].

5.1.2 Optical and Epitaxial Layers

Figure 5.5 is a schematic of the MTVCSSEL optical design, it is a cross section through the center of the membrane.

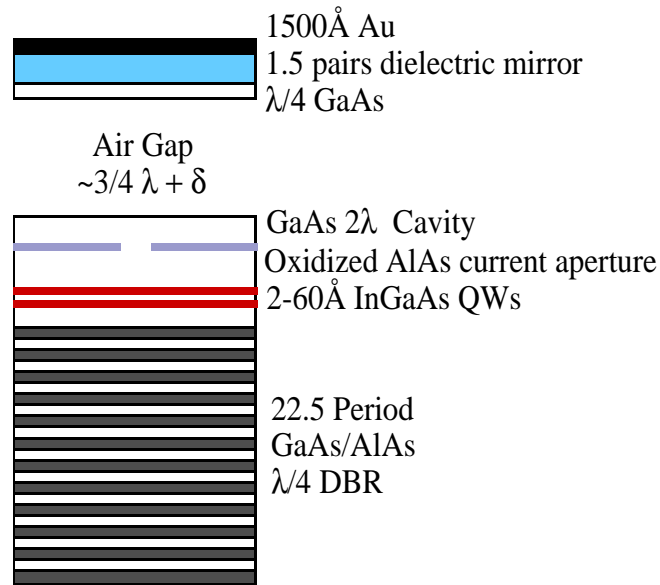


Figure 5.5: Optical layers in the MTVCSSEL.

The final epitaxial and optical design of the MTVCSSEL are shown in Table 5.1 below.

Thickness	Material	Index	Comment
250 nm	Au	0.24-i6.59	
142.74 nm	SiO ₂	1.46	$\lambda/4$ -phase match to Au
118.29 nm	Si ₃ N ₄	2.05	$\lambda/4$
166.1 nm	SiO ₂	1.46	$\lambda/4$
473.17 nm	Si ₃ N ₄	2.05	λ
206.04 nm	GaAs	3.53	$3\lambda/4$
870 nm	Al _{0.85} Ga _{0.15} As		$3\lambda/4 + \delta$, sacrificial layer
161.3 nm	GaAs	3.53	p type
34.5 nm	Al _{0.33} Ga _{0.67} As	3.35	p type
50 nm	Al _{0.97} Ga _{0.03} As	2.98	oxide layer, p type
167.7 nm	Al _{0.33} Ga _{0.67} As	3.35	p type
12.97 nm	GaAs	3.53	
6 nm	In _{0.2} Ga _{0.8} As		quantum well

Table 5.1 Epitaxial and Optical Design of MTVCSSEL

Thickness	Material	Index	Comment
10 nm	GaAs	3.53	
6 nm	In _{0.2} Ga _{0.8} As		quantum well
12.97 nm	GaAs	3.53	
120.4 nm	Al _{0.33} Ga _{0.67} As	3.35	n type
81.93 nm	AlAs	2.97	$\lambda/4$, 24 times, n type
68.68 nm	GaAs	3.53	$\lambda/4$, 24 times, n type
81.67 nm	AlAs	2.97	$\lambda/4$, n type
300 nm	GaAs	3.53	buffer layer, n type
500 nm	GaAs	3.53	wafer, n type
118.29 nm	Si ₃ N ₄	2.05	$\lambda/4$ antireflection layer

Table 5.1 Epitaxial and Optical Design of MTVCSSEL

The layers with an index are used in the thin film simulation of the MTVCSSEL. The sacrificial layer will be air in the MTVCSSEL so it has a refraction index of 1 in the simulation. The thin film simulation of the optical structure is a plane wave calculation used to insure that the quantum wells are located at a standing wave maximum and that the aperture is located at a standing wave minimum as shown in Figure 5.6.

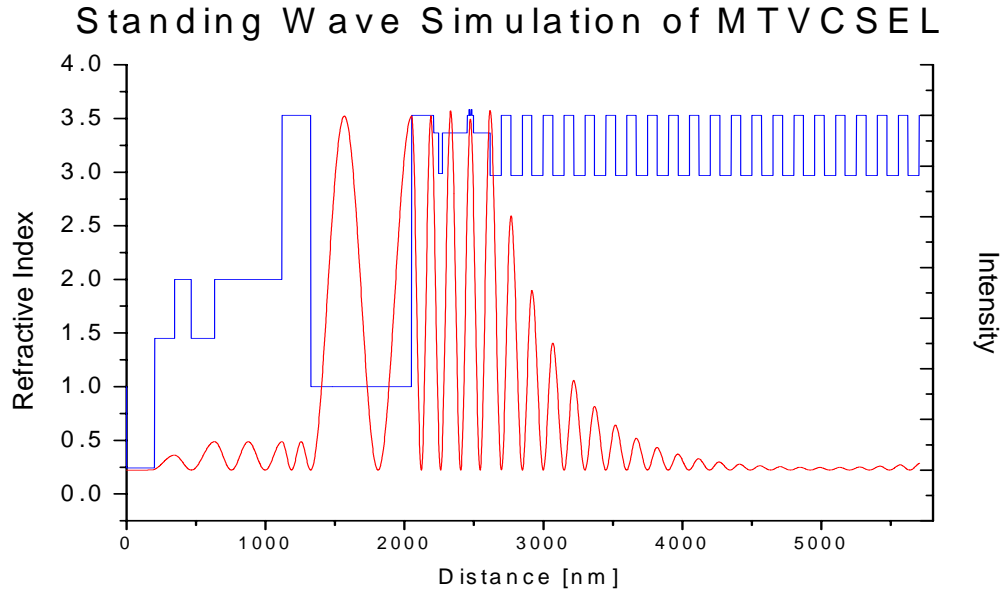


Figure 5.6: Standing wave simulation of the MTVCSSEL.

5.2 Results

5.2.1 Output Power, Voltage, Current

The optical output power and the diode forward voltage are plotted versus the diode current in Figure 5.7. The result is a typical curve and all of the devices with a 5 μm aperture show approximately the same performance. The threshold current of 0.45 mA represents a threshold current density of 2.2 kA/cm^2 . The high voltage drop across the diode is likely due to a combination of high contact resistance in the non-alloyed P contact and losses from current spreading. The ripple on the output power may be due to thermal tuning of the wavelength across the parasitic cavity formed by the reflections off the back surface of the wafer.

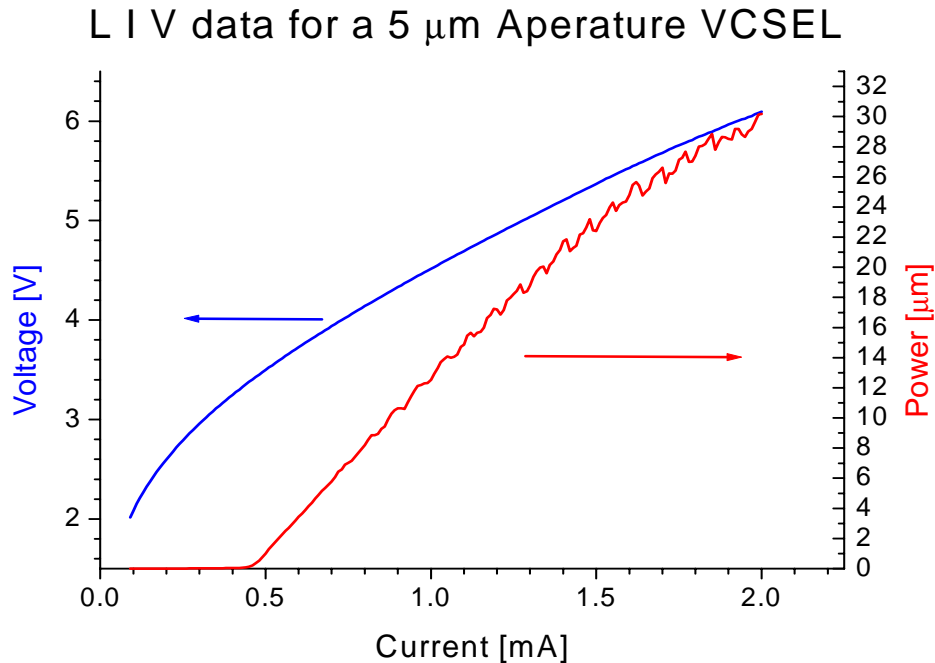


Figure 5.7: L I V data for MTVCSSEL.

5.2.2 Tuning

The MTVCSSEL is tuned by applying a bias between the membrane and the top surface of the wafer. For the tuning experiments and the Frequency Locked Loop setup the best technique for driving the three terminal device was to ground the top surface of the wafer and bias the membrane relative to that. The only drawback to this technique was that the diode drive current had to be sunk out of the backside contact and through the wafer carrier, which due to its large capacitance precluded making pulsed measurements. The lasing output was coupled into a multimode GRIN fiber and feed into an HP optical spectrum analyzer. Figure 5.8 shows an overlay of optical spectra for different membrane biases. The plot shows a tuning range of 17 nm for a 44 volt membrane bias. The largest

tuning range measured was 23 nm. The lasing wavelength versus tuning bias is plotted in Figure 5.9 for the data measured in Figure 5.8.

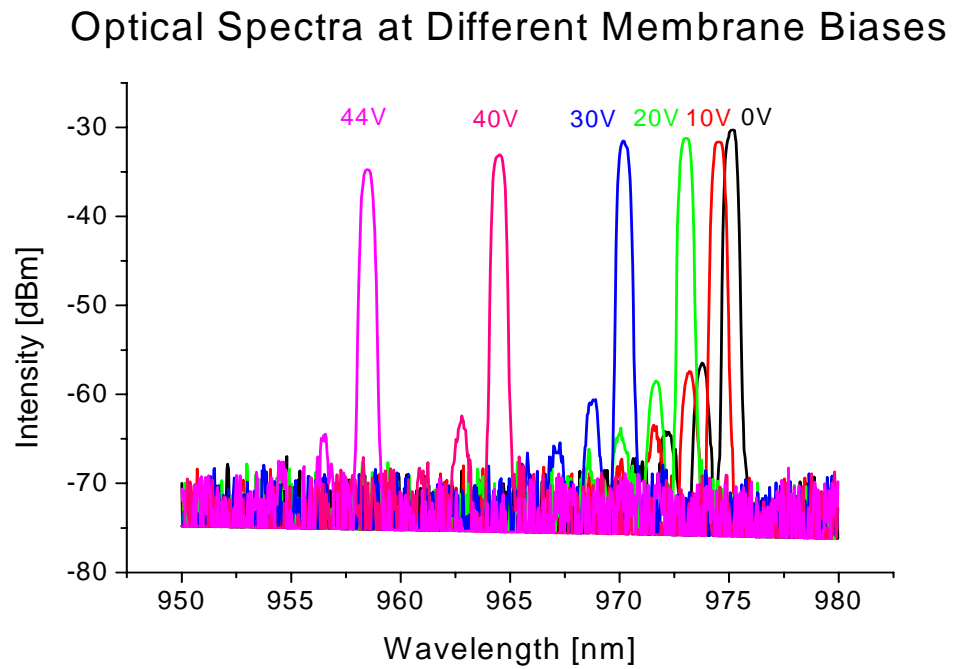


Figure 5.8: Optical Spectra of the MTVCSSEL at different membrane biases.

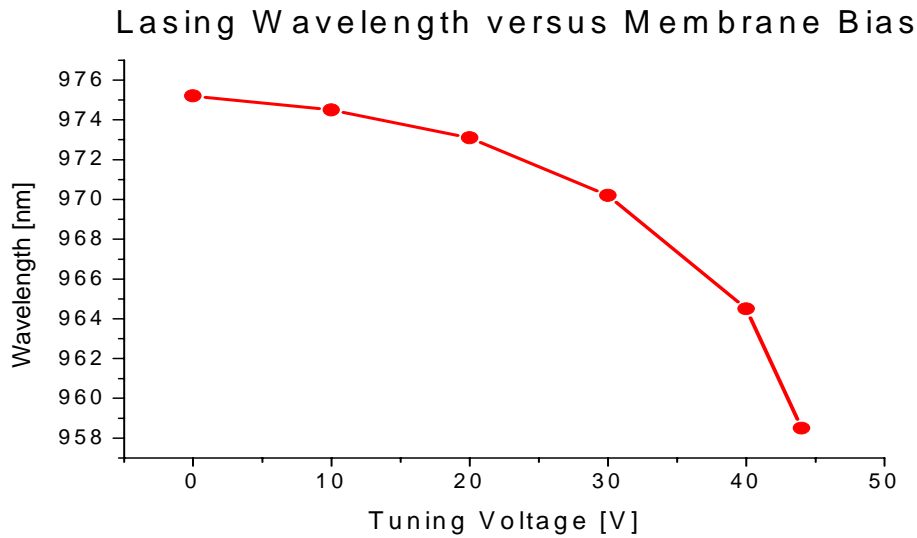


Figure 5.9: Lasing wavelength versus membrane bias.

The spectra show that the device is single mode and that the side mode suppression is better than 25 dB across the entire tuning range. The side mode suppression ratio, SMSR, is an important parameter for lasers that will be used in a WDM system. Lasing power in any additional modes represent noise in the system. Figure 5.10 shows the best case measured SMSR of 38 dB. The SMSR of a device depends highly on the mechanical flatness of the top mirror. The devices are tested on wafer and electrical contact with the membrane and top side p contact is made with needle probes. The process of putting a probe on the membrane can damage its mechanical structure, which reduce the SMSR of the device. The device in Figure 5.10 was tested without contacting the membrane so that the maximum SMSR could be determined.

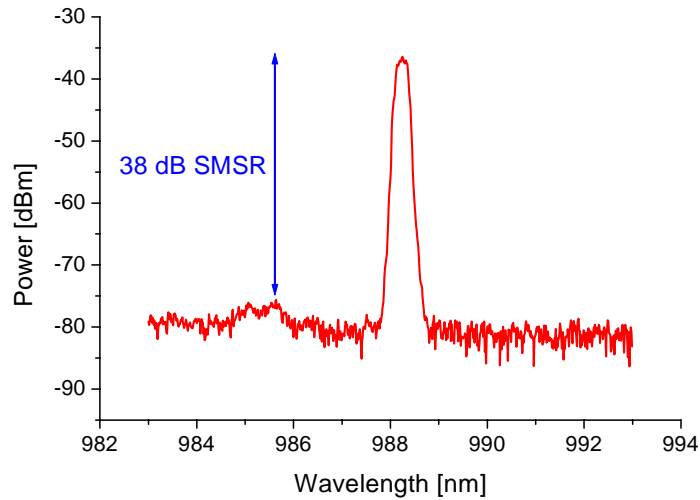


Figure 5.10: Side Mode Suppression Ratio.

The rate at which the wavelength can be tuned is an important parameter in WDM systems. In a previous work Figure 5.11 was measured for the temporal response of the lasing wavelength versus time when a step in membrane bias is applied [7]. The results show that the tuning rate is limited by the membrane response which shows a 1 microsecond response and 2 microseconds of ringing.

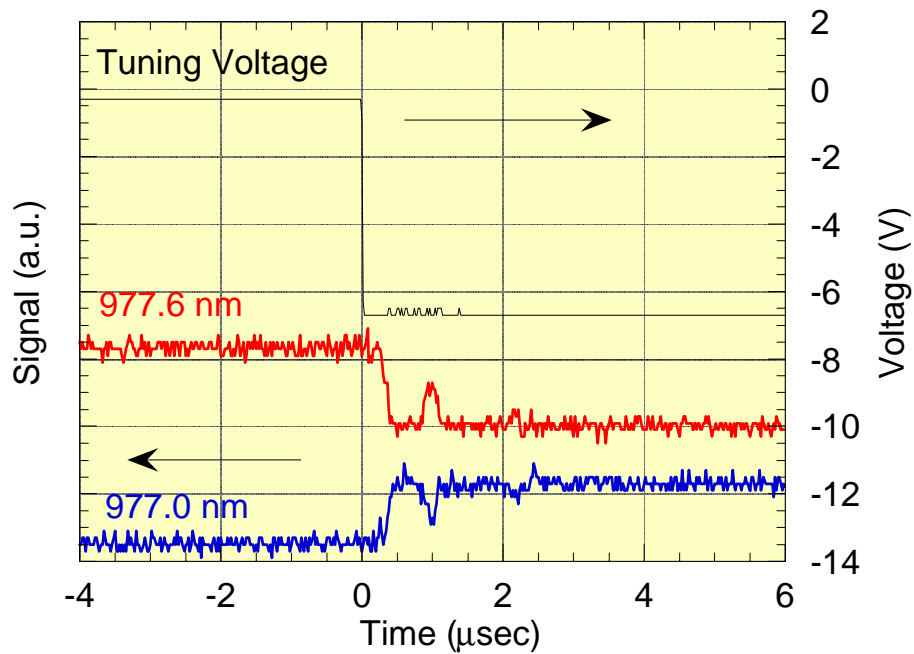


Figure 5.11: Wavelength tuning versus time [7].

5.2.3 Linewidth

Linewidth is important for any laser to be used in a communications system as the wider the linewidth the larger the effect of dispersion. Linewidth can be especially important in a dense wavelength division multiplexing, DWDM, system as it may limit the spacing between channels. To measure the linewidth, fiber coupled light from the MTVCSEL was connected to a Burleigh scanning Fabry-Perot Interferometer. Figure 5.12 shows the measured linewidth of the MTVCSEL to be approximately 2.1 GHz.

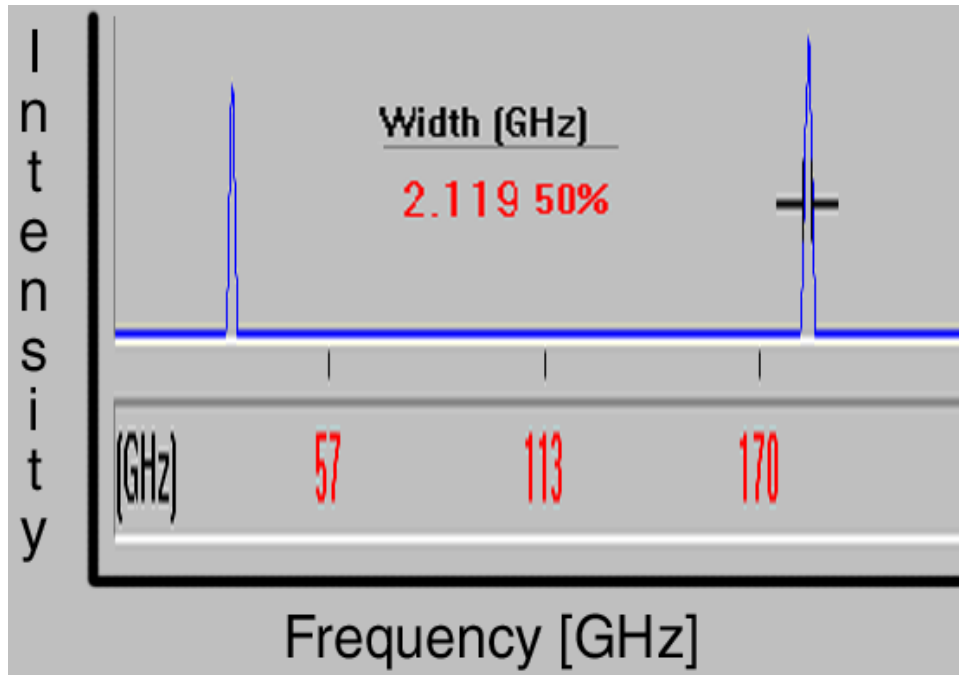


Figure 5.12: Lasing linewidth.

Figure 5.13 is a waterfall plot of the linewidth measured at 1 second intervals for 1 minute to demonstrate the short term stability of the laser linewidth and wavelength.

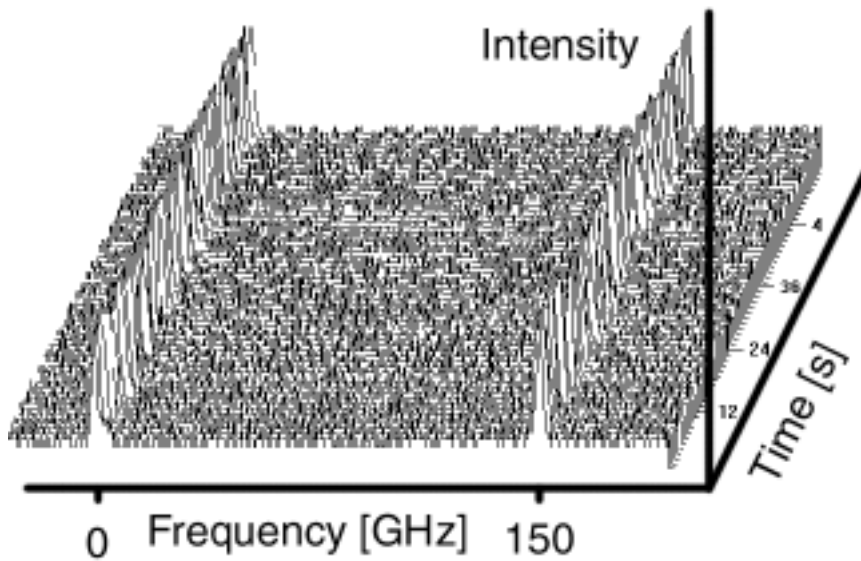


Figure 5.13: Linewidth and Wavelength stability.

The linewidth versus output power was measured to determine the limits on device performance. As is shown in Figure 5.14 the linewidth of the MTVCSSEL decreases at low powers and saturates at approximately 2 GHz for higher output powers. All of the previous measurements, Figure 5.12 and Figure 5.13 were taken at a high laser output power.

The Schalow-Townes formula is the quantum limit for the minimum linewidth of a laser considering only spontaneous emission noise. However there are various thermal noise sources such as carrier noise and oscillation of the cavity length that can increase the linewidth. In the Schalow-Townes limit, linewidth is proportional to the inverse of the output power so that when the output power increases the linewidth decreases as long as the laser remains single mode.

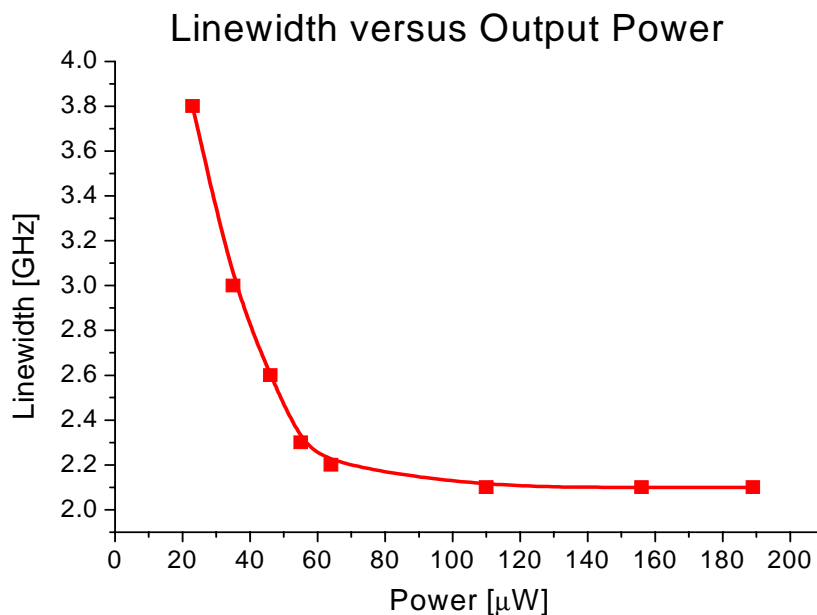


Figure 5.14: Linewidth versus output power.

The standard Schalow-Townes equation is modified for the case of semiconductor laser diodes. In semiconductors the relaxation oscillations that follow a spontaneous emission event change the refractive index of the semiconductor and this produces a linewidth

broadening parameter α for which the linewidth is increased by a factor $(1+\alpha^2)$ [89]. The linewidth in a semiconductor laser is given by Equation (5.1) [89].

$$\Delta f = \frac{v_g^2 \hbar \omega g n_{sp} \alpha_m (1 + \alpha^2)}{4\pi P_o} \quad (5.1)$$

In the equation there are several parameters that have to be quantified; v_g is the group velocity of light in the active region, g is the gain of the laser, n_{sp} is the spontaneous emission factor, α_m is the loss rate through the mirrors and P_o is the output power. The group velocity is $8.5 \cdot 10^7$ m/s, the threshold gain is 560 cm^{-1} , n_{sp} is 3, α_m is 3.3 cm^{-1} , and α is 3.4. The result is that the linewidth should be 4 GHz at $20 \text{ }\mu\text{m}$, and 2 GHz at $40 \text{ }\mu\text{m}$ in line with the observed results. However, the saturation of linewidth narrowing with increased output power cannot be explained by spontaneous emission noise. A standard VCSEL with integrated mirrors of a design similar to that used for the MTVCEL also shows a saturation of linewidth decrease for increasing output powers, so the saturation effect is likely due to carrier noise effects or limitations of the linewidth measurement system. The resolution of the scanning Fabry-Perot interferometer was rated to be better than 1 GHz, but that could be degraded by optical alignment.

Chapter

6

Frequency Locked Loops for WDM systems

WDM systems have enabled a great increases in the bandwidth of fiber optic communications systems. By allowing the reuse of a scare resource, buried or installed fiber, WDM has also significantly reduced the cost of a given amount of bandwidth in a fiber optics communications system. The application of WDM to any transmission technology requires significant improvements in the transmitter performance. WDM fiber optics communications systems have therefore required improved lasers. Specifically the wavelength of the laser must be controlled to very tight tolerances and long term drift must be eliminated through improved laser design and/or feedback control. The design of the MTVCSSEL produces a continuously tunable laser for which there is no obvious way to effect wavelength control other than feedback from an external wavelength reference.

6.1 FLL Concept

Frequency locked loops are simply phase looked loops with one less integrator and are perfectly capable of controlling the wavelength of a tunable laser like the MTVCSSEL. Since the phase of an optical oscillator cannot be easily measured because photodetectors measure optical intensity, not electrical field, a FLL is more appropriate than a PLL. Additionally for a PLL to operate the loop bandwidth must be greater than the laser linewidth

which is not possible in this case as the laser has a linewidth of 2 GHz and the tuning membrane which would be part of the PLL loop has a bandwidth of ~ 1 MHz.

The basic concept of a FLL as applied to wavelength control for the MTVCSSEL is show in Figure 6.1.

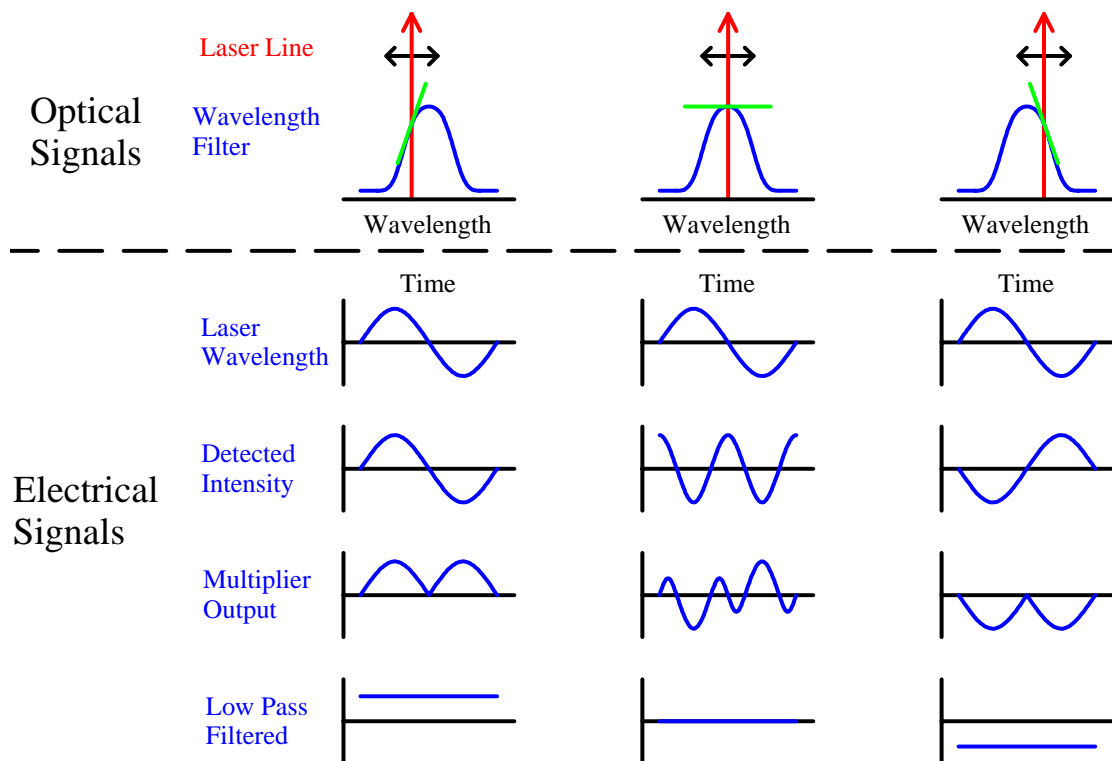


Figure 6.1: FLL Concept.

The FLL is built from the MTVCSSEL, a wavelength selective bandpass filter, a photodetector and the feedback electronics. The wavelength selective bandpass filter is made from an optical spectrometer and a photodiode is used to measure the intensity of the light transmitted through the spectrometer. The left column of Figure 6.1 illustrates the case when the wavelength of the light produced by the MTVCSSEL is shorter than the peak transmission wavelength of the wavelength selective optical bandpass filter. If a sinusoidal dither signal is added to the tuning input of the MTVCSSEL the lasing wavelength

oscillates in phase with the dither signal and the detected intensity after the bandpass filter also oscillates in phase with the dither signal. If the dither signal is multiplied by the detected signal and low pass filtered the result is a positive DC signal that can be feedback to move the MTCSEL towards the desired operating wavelength. The right column of Figure 6.1 shows the case when the wavelength is shorter than the transmission maximum of the wavelength selective optical bandpass filter. In this case since the lasing wavelength is now on the other side of the transmission maximum the local slope of the wavelength selective optical bandpass filter has changed and the detected intensity at the photodiode is 180 degrees out of phase with the dither signal. Now when the dither signal is multiplied by the detected signal and low pass filtered the result is a negative DC signal that can be feedback to move the MTCSEL towards the desired operating wavelength. The final case when the FLL is locked on the desired wavelength is shown in the center column of Figure 6.1. Here when the dithered laser wavelength is passed through the wavelength selective optical bandpass filter the slope oscillates from positive to negative and back creating a frequency doubled signal. The product of two sinusoidal signals with different frequencies has no DC value and the feedback produces stable operation at the desired wavelength.

6.2 Linear FLL

6.2.1 Design

The design of a linear FLL is shown schematically in Figure 6.2. In the schematic, the MTCSEL is represented as a diode with a tuning input. The frequency selective filter is shown as the large black rectangle outside the dashed blue line. The frequency selective filter is in this case an arrayed waveguide grating, AWG, wavelength multiplexer. The AWG multiplexer is used to couple different wavelengths of light onto the same fiber with significantly less loss than a tree of Y branch waveguide combiners [99]. The second AWG shown is used as a demultiplexer to provide the feedback signal. Using this system a group of MTCSELS can be frequency locked to different channels of the AWG and

routed over the same fiber. The sinusoidal source is an HP function generator, and the multiplier is a gilbert cell based integrated circuit from Analog Devices. The rest of the devices in the figure are simple electronics implemented with op-amps and passive components including: a gain block, a bandpass filter, a low pass filter, an integrator with a stabilizing zero and a summing node.

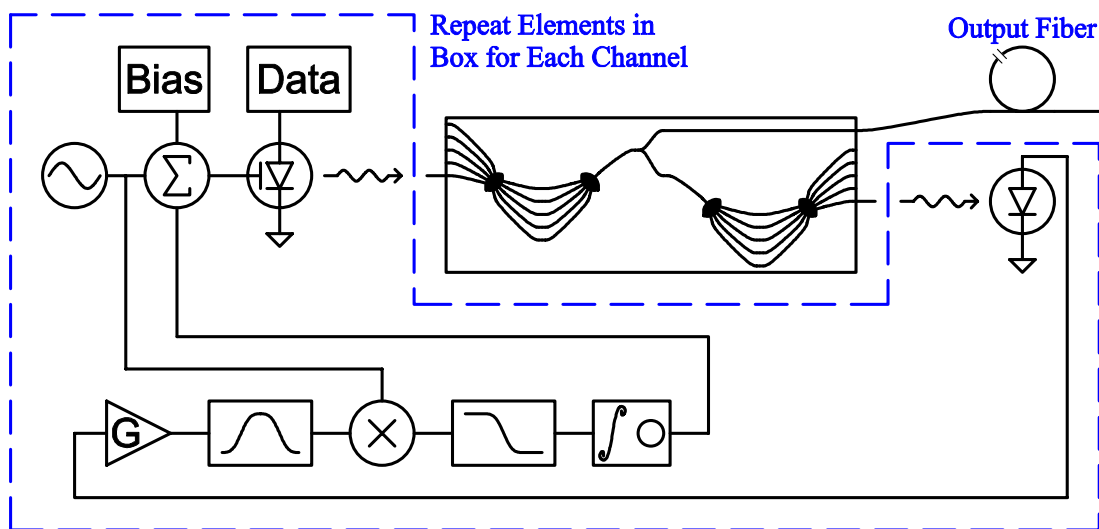


Figure 6.2: Linear FLL.

6.2.2 Simulation

The linear FLL system was simulated using models of the MTVCSSEL, the AWG and the electronics using Matlab. The simulation was discretized using the z transform and the operating point for the linear FLL was determined at each time step using a secant search. The system is setup in an initial condition with the tuning voltage 0.5 less than that desired for frequency locking and with the transmission maximum of the wavelength selective filter at 950 nm. The feedback voltage, V_c , quickly goes to the needed 0.5 volts in 0.35 milliseconds as shown in Figure 6.3. The wavelength moves to the required 950 nm and oscillates slightly about it due to the dither signal as shown in Figure 6.4. Figure 6.5 shows

that the power throughput of the wavelength selective filter, which represents the useful power of the laser, is greater than 99% in the locked condition.

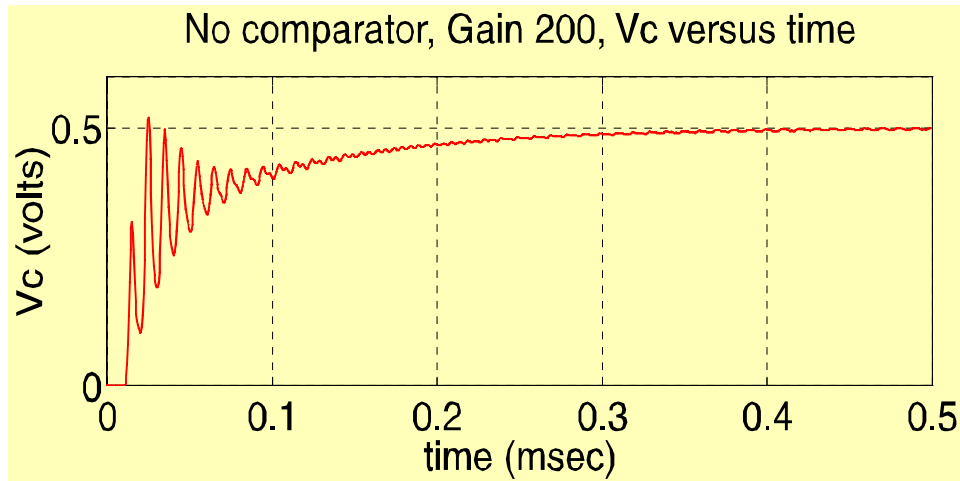


Figure 6.3: Linear FLL, V_c

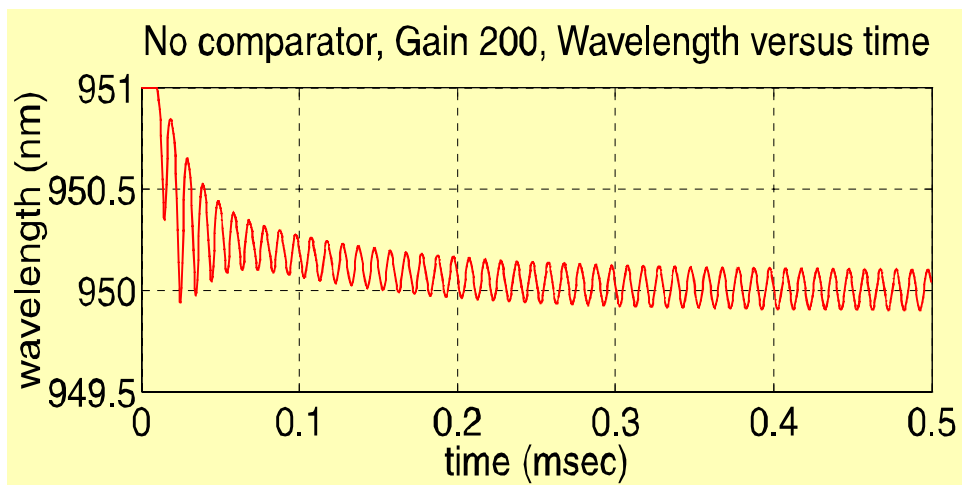


Figure 6.4: Linear FLL, Wavelength.

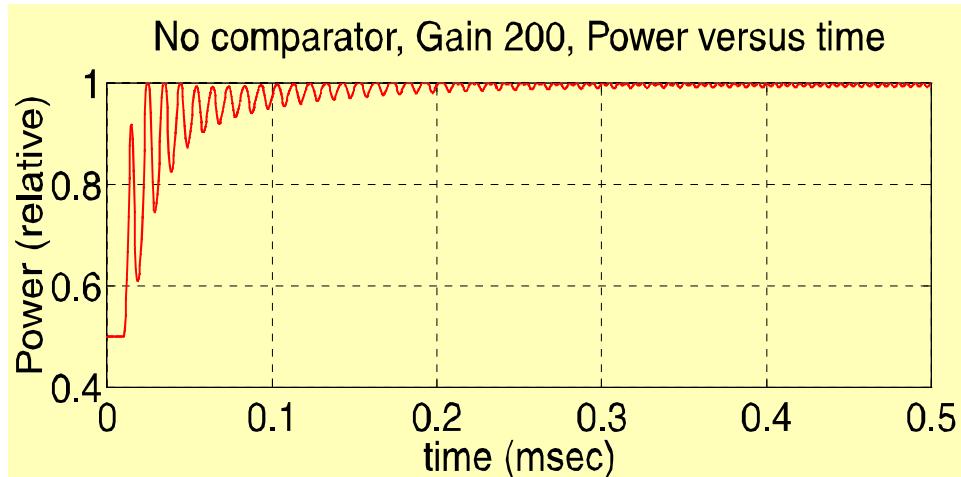


Figure 6.5: Linear FLL, Power.

The gain of the linear FLL system may change due to variety of reasons including but not limited to: modulation of the laser diode output by a data stream, aging of the membrane, aging of the device active layers, and imperfect coupling of the lasing mode into an output fiber. The change on the gain of a feedback system can change the response significantly. Figure 6.6 shows that as the gain is reduced the time to reach the frequency locked condition is increased. Figure 6.7 shows that as gain is increased the system rings with a highly underdamped response, but finally reaches frequency lock. For higher gains as in Figure 6.8 the system eventually becomes unstable.

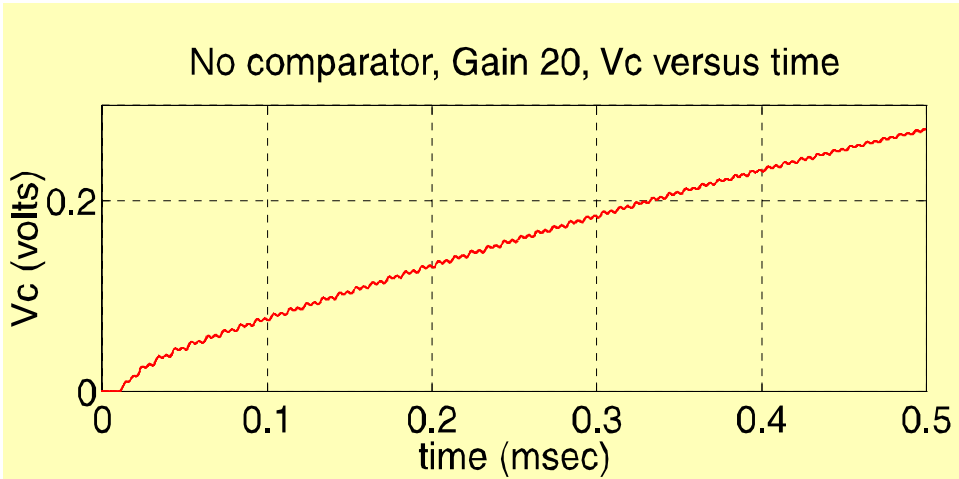


Figure 6.6: Linear FLL, V_c , gain $\div 10$.

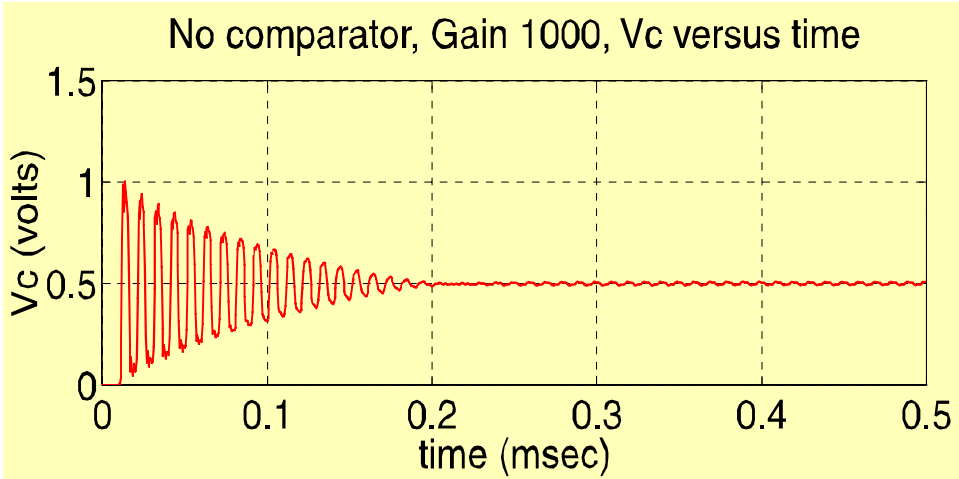


Figure 6.7: Linear FLL, V_c , gain $\times 5$.

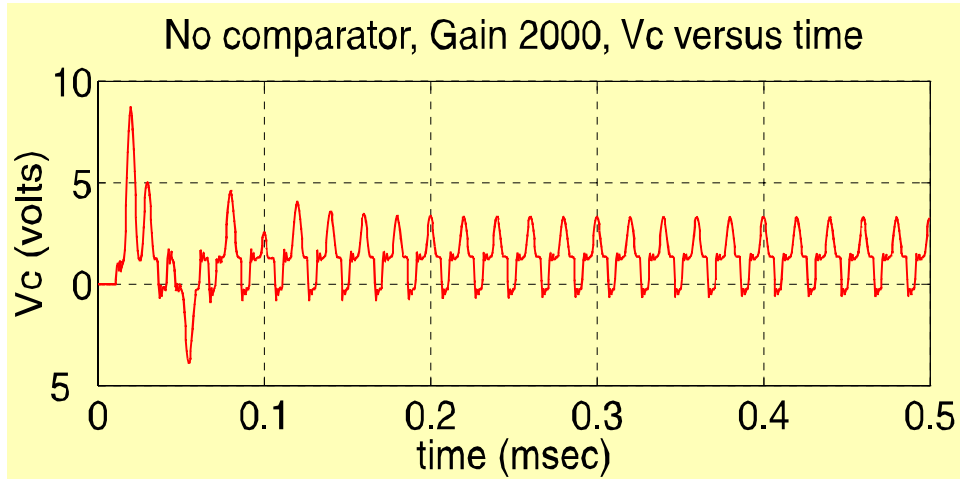


Figure 6.8: Linear FLL, V_c , gain $\times 10$.

6.3 Nonlinear FLL

The gain sensitivity of the linear FLL will prevent its use in real WDM systems. A method to make the system insensitive to gain changes in the optical system is needed to allow the use of the FLL in practical applications. Horowitz et. al. [104] have analyzed what they call an externally excited adaptive loop, EEAS, using quantitative feedback theory, QFT. The FLL is just one possible design of an EEAS.

6.3.1 Design

Figure 6.9 shows the schematic for the Nonlinear FLL where a relay element has been added after the bandpass filter. The placement of the relay element after the plant allows the system to be insensitive to the gain of the plant. All of the loop dynamics will be controlled by low speed electronic gain which is easy to control. Except for the addition of the relay element the design is exactly the same as the Linear FLL. When adding any nonlinear element to a circuit it should be added at a point of low noise or high SNR [109]. In this design the electrical bandpass filter will greatly reduce the bandwidth of the system

removing much of the out of band noise and producing a high SNR signal. Therefore it is better to place the relay element after the electrical bandpass filter.

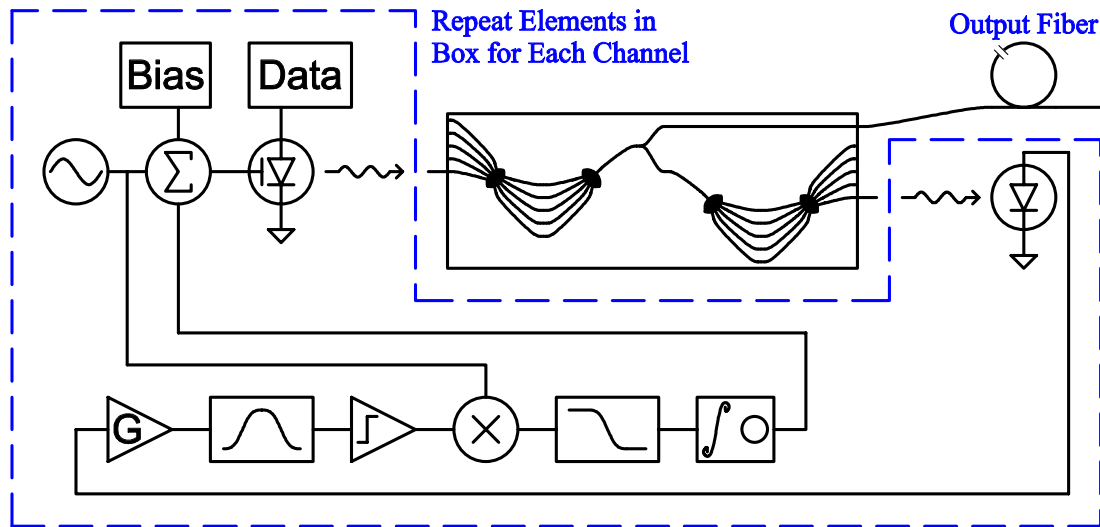


Figure 6.9: Adaptive Gain Nonlinear FLL.

6.3.2 Simulation

The Nonlinear FLL was simulated using the same techniques and models as the Linear FLL. However, with a relay element inside the loop it is impossible to determine a unique operating point at each time. The most expedient way to build the simulator was to use the brute force technique of decreasing the time step until the simulation results stopped changing. Although this simulation required more time than the Linear FLL simulation the maximum time required to run was still on the order of a few minutes on a 200 MHz UltraSPARC II based Sun workstation.

Figure 6.10 shows the feedback voltage versus time for the same case as the Linear FLL in Figure 6.3. The simulation results show that it takes slightly longer for the Nonlinear FLL to reach a frequency locked condition, 0.45 ms versus 0.35 ms and that the Nonlinear FLL shows no signs of being underdamped. Figure 6.11 is the wavelength and

Figure 6.12 is the power throughput for the nonlinear loop. The long term performance of the nonlinear FLL approximately equivalent to the linear design.

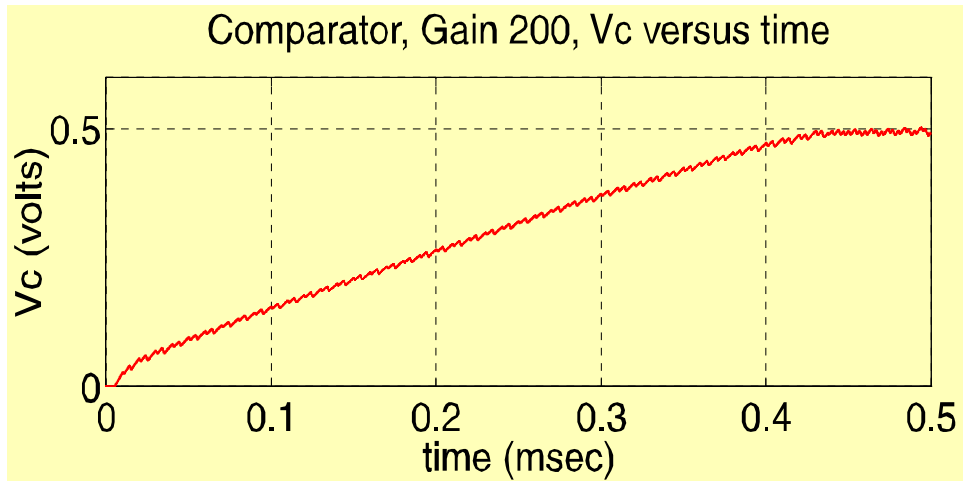


Figure 6.10: Nonlinear FLL, V_c .

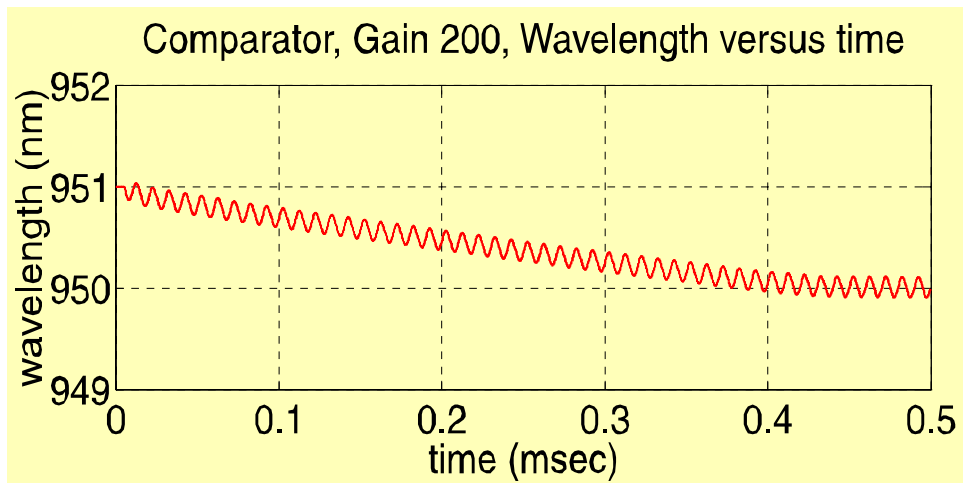


Figure 6.11: Nonlinear FLL, Wavelength.

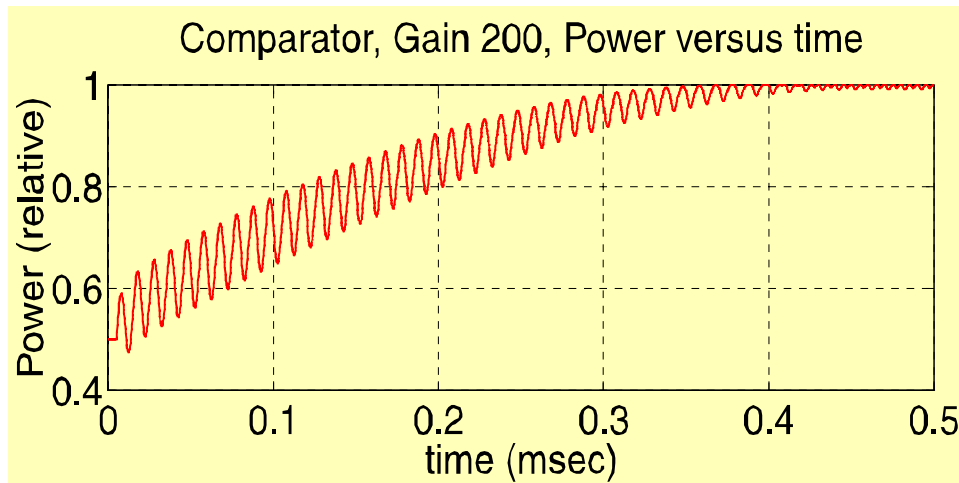


Figure 6.12: Nonlinear FLL, Power.

Figure 6.13 shows the feedback voltage and Figure 6.14 shows the power throughput for the case of a significantly reduced plant gain. The results are identical to those of the default gain case. Figure 6.15 shows the feedback voltage and Figure 6.16 the power throughput for the case of a significantly increased plant gain and as expected they are identical to the previous results. The relay element has provided the gain insensitivity needed to build robust FLLs.

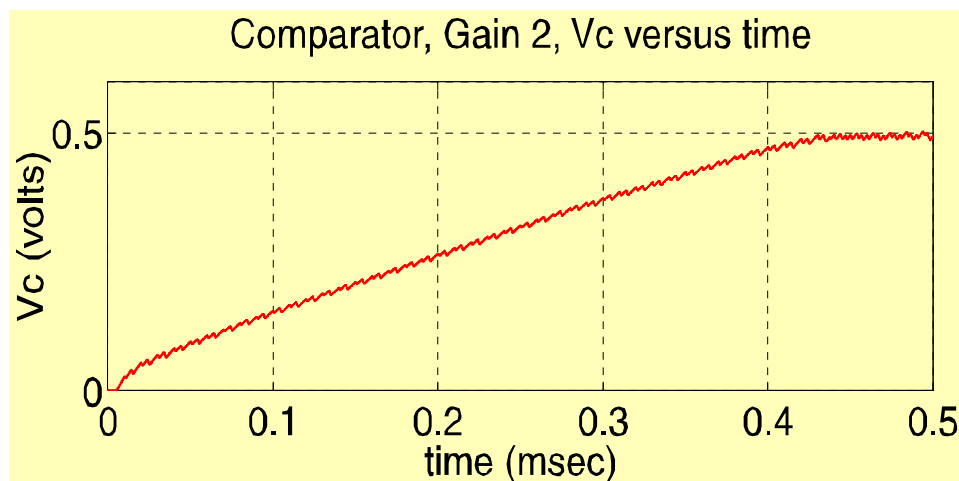


Figure 6.13: Nonlinear FLL, V_c , gain $\div 100$.

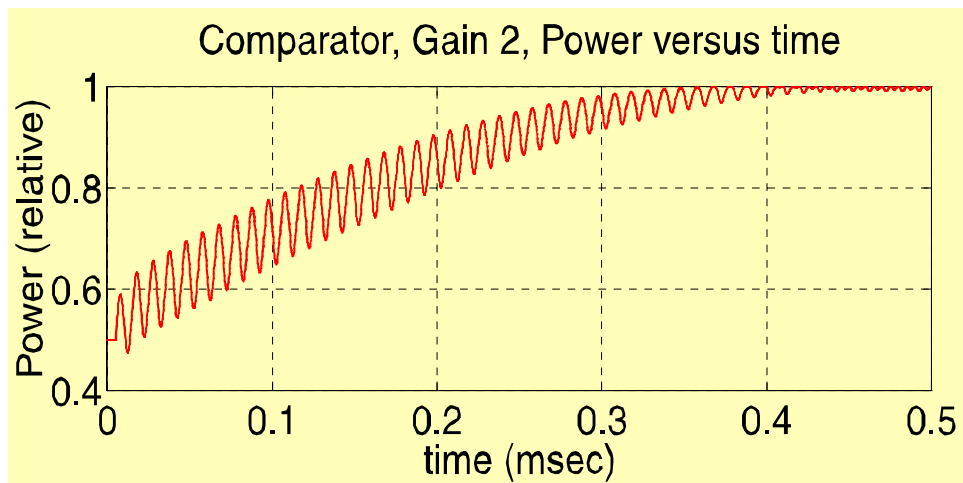


Figure 6.14: Nonlinear FLL, Power, gain $\div 100$.

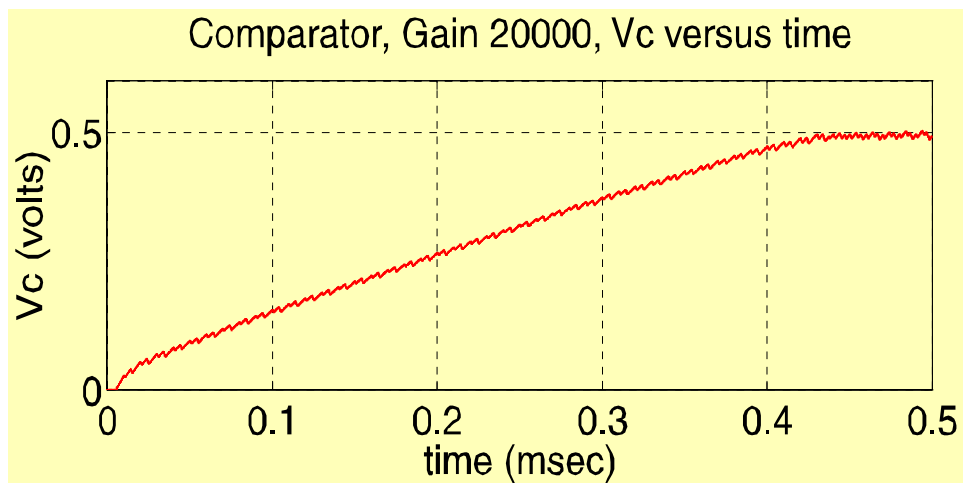


Figure 6.15: Nonlinear FLL, V_c , gain $\times 100$.

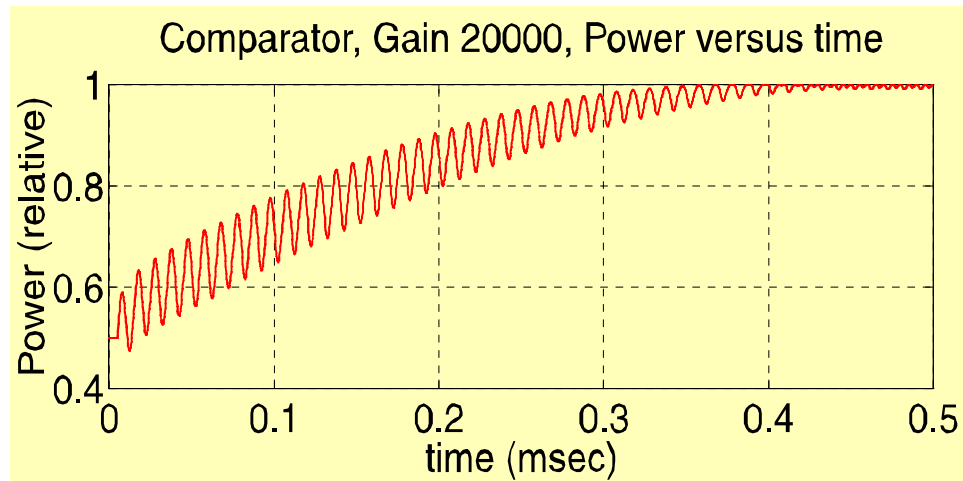


Figure 6.16: Nonlinear FLL, Power, gain $\times 100$.

6.3.3 Quantitative Feedback Theory

As mentioned before, QFT for the EEAS has previously been developed [104]. The Nonlinear FLL will be partitioned into blocks so that the results of the QFT can be applied. Figure 6.17 shows the Nonlinear FLL partitioned into the gain blocks of the QFT analysis.

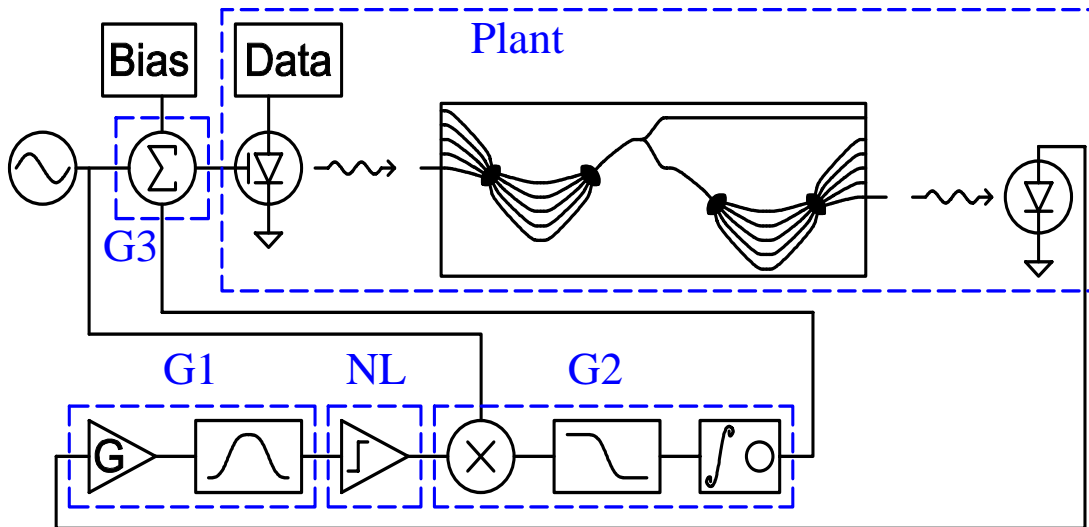


Figure 6.17: Nonlinear FLL gain blocks.

QFT uses describing functions to analyze the behavior of the system [111]. The use of describing functions requires that the conditions for quasilinearity be met [104]. If the nonlinearity is a pure relay element the conditions will always be met, if the nonlinearity is other than a relay element the magnitude of dither signal at the input of the nonlinear element will have a minimum required value. This system uses a pure relay element so quasilinearity is assured for all operating conditions, but even with a small deadzone due to hysteresis the amplitude requirements are smaller than the dither signal amplitude used in this system due to empirically determined signal to noise requirements.

The results of QFT produces two requirements on the loop gain of the system. The first, Equation (6.1) prevents a parasitic limit cycle oscillation from occurring by insuring that the magnitude of the loop gain is less than unity at the frequency where the loop has a 180 degree phase shift. The second, Equation (6.2) ensures that the system maintains quasilinear operation under the most extreme operating conditions given the limited swing range of any real electronic implementation. In the equations, G_1 , G_2 , and G_3 are the gains in the different blocks. K_1 is minimum gain and K_2 is the maximum gain of the plant under control and P is the frequency response of the plant. The amplitude of the relay out-

put is M , m is the maximum voltage swing of the electronics, and α is 3 from the quasilinearity requirements. The most extreme conditions that the plant must continue to function under are Z_e and $(b + j\omega)$ is the dominate pole in the response of the plant.

$$|L(\omega_\pi)| = \frac{M}{A} |G_1 G_2 G_3 K P(\omega_\pi)| < \rho = 1 \quad (6.1)$$

$$|L(\omega_o)| \geq \frac{2\alpha K_2}{m K_1} |(b + j\omega_o) Z_e(\omega_o)| \quad (6.2)$$

The limit cycle condition is easily meet by the present system. The limited swing range condition requires some more detailed consideration. The most extreme requirements for operation are the Telcordia shock and vibration specifications which specify a 10 G operating vibration test. Additionally the laser power output may be modulated by 40 dB to send data over the fiber. Applying both inputs and plotting the results as a function of frequency produces Figure 6.18.

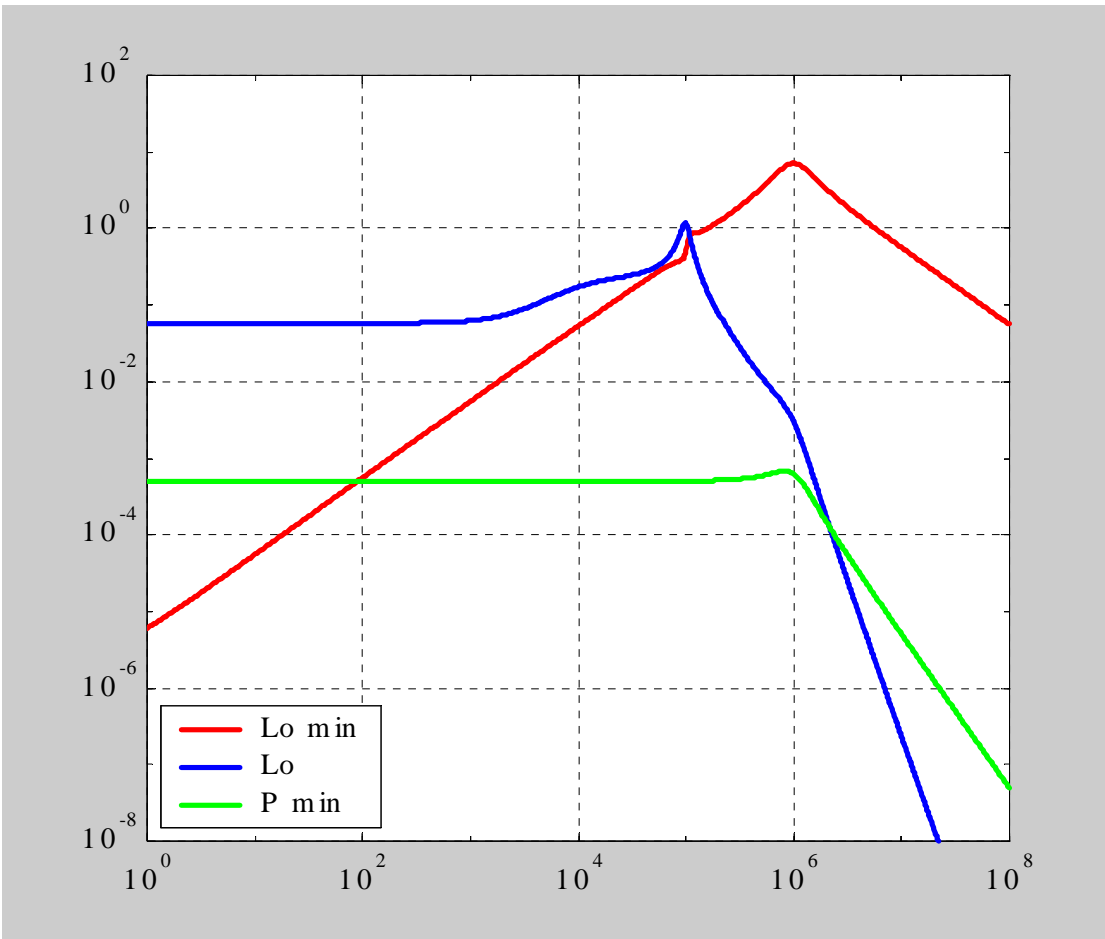


Figure 6.18: QFT for the nonlinear FLL.

The loop gain is just larger than the requirement at the dither frequency, ω_o , so the system will meet the specifications. Unfortunately the required loop gain for any dither frequency will always be larger than the plant gain due the impulse nature of the shock disturbance. This means that there will always be some band of frequencies where the loop gain is larger than the plant gain producing an amplification of the sensor noise. More complicated control solutions can be implemented with multiple loops to compensate for the gain and phase of the plant. The data dependent gain of the system can easily be compensated for in a model system which will reduce the required gain from the modulation level, which is assumed to be 40 dB down to a only few dB as needed to allow for ageing,

device variation and the fundamental nonlinearity of the micromachined wavelength tuning response. A control loop for phase compensation will allow the use of higher dither frequencies beyond the resonance frequency. A capability that could be very useful in real world systems. Micromachined membranes typically have a weakly underdamped response in air, however the primary damping force is from the displacement of air. Vacuum packaged micromachined membranes have a highly underdamped response and demonstrate a strong tendency to ring at the resonance frequency. This membrane oscillation will create side modes off of the main lasing mode which increases the effective linewidth of the source and may cause crosstalk in DWDM systems. A system with a dither frequency higher than the membrane resonance could be used to suppress the ringing and reduce the crosstalk between channels in the DWDM system.

6.4 Results

The experimental setup used to test the system is shown as a schematic diagram in Figure 6.19. The device is electrically contacted using a pair of needle probes on the top-side and through the substrate on the bottom side. A CCD camera coupled through a microscope is used to align the probes. The laser diode is biased by current source from a semiconductor parameter analyzer. The laser output is emitted through the bottom of the structure. The lasing output is collimated by another microscope objective and a beam splitter produces two streams, one for analysis and one for feedback. The analysis beam is coupled into a HP optical spectrum analyzer for real time information about the lasing spectrum. The other beam is coupled into a tunable optical grating spectrometer. A photodiode on the exit port of spectrometer senses the intensity of the light and the feedback electronics uses that signal to frequency lock the MTVCSSEL.

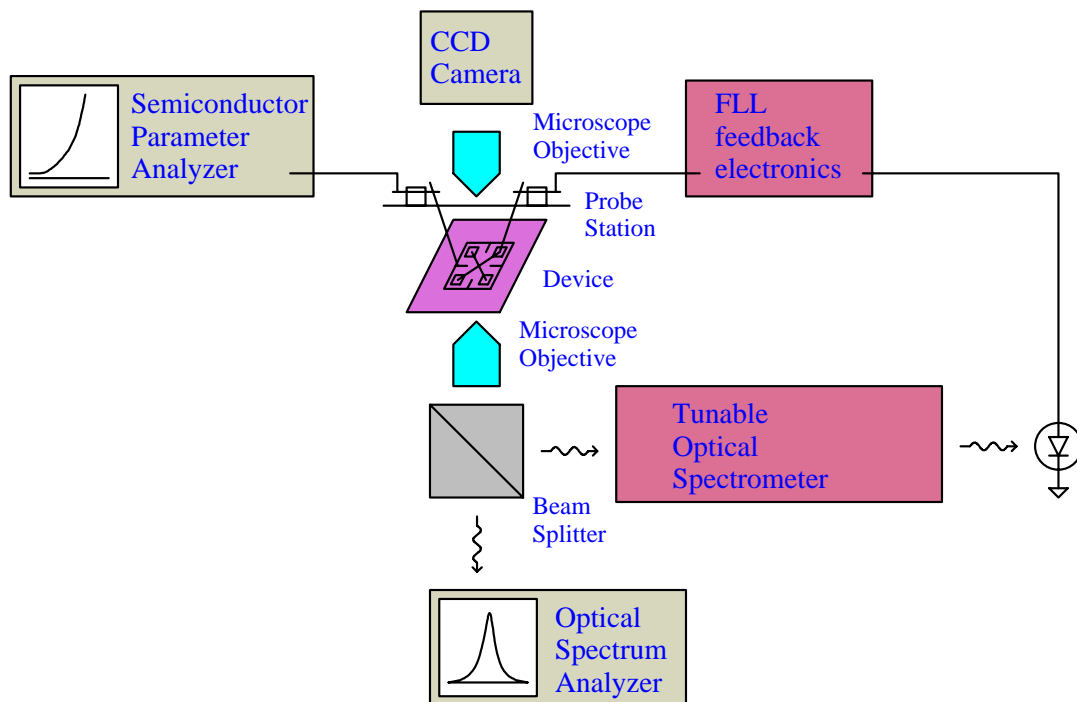


Figure 6.19: Schematic of FLL measurement setup.

The results of the frequency locking experiments are shown in Figure 6.20. The traces are a display of the MTVCSEL tuning bias voltage versus time for three different wavelength settings of the spectrometer. As expected the curves look qualitatively like those shown for the system in the frequency locked condition, next to bottom plot, center column of Figure 6.1. Quantitatively the plots show a larger DC bias voltage for the shorter wavelengths. Note that due to the grounding setup for the device the membrane zero bias point was actually -22 volts on the scale shown on Figure 6.20.

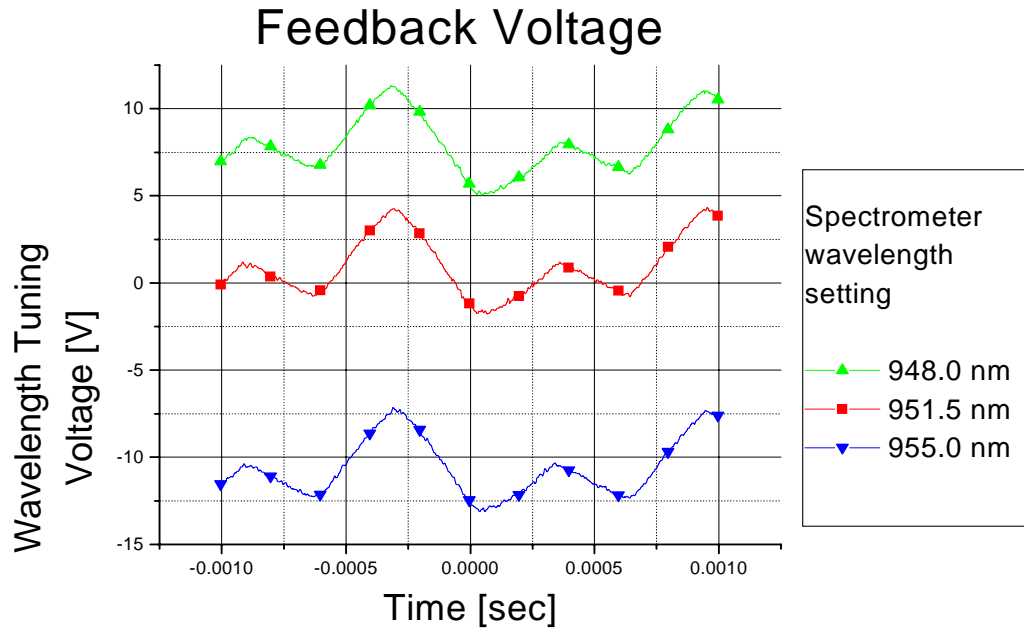


Figure 6.20: Measured V_c of FLL for different wavelength settings.

The frequency locking system as shown in Figure 6.20 is using too large of a dither voltage and a loop gain that is too high. Future implementations of the system would allow for better control of the gain in the different subblocks. This will allow the feedback system to be better optimized. Even so, the system achieved frequency lock and showed an 11 nm tracking range. The tracking range was tested by tuning of the optical spectrometer. The tracking range was only limited by the output swing range of the electronics used to implement the FLL.

Chapter
7

Summary and Future Work

7.1 Summary

WDM has established itself in the long haul telecommunications market. However the current implementations are primarily simple point to point solutions and fall far short of the promise of an all optical network. Presently most WDM systems use temperature controlled DFB lasers. Each laser is grown and fabricated for a specific wavelength. The increasingly large number of wavelengths creates significant inventory and sparing problems. Many tunable laser solutions including: micromachined VCSELs, multisection DFBs, external cavity lasers and few other designs are competing for the sparing market.

Shorter distance communications systems such as Metro and LAN can also benefit from WDM but are much more cost sensitive. The price sensitivity may limit the competitiveness of any micromachined device in this market, but there are few other tunable solutions available that have the potential to be low cost.

The next goal beyond WDM is an optically switched network in which the laser wavelength can be changed to another channel faster than the data packet rate to allow for optical routing of signals. This will require a rapidly tunable source. There are even fewer options in this market than there are in the low cost market. The current MTVSEL is too slow, but with improvements to the membrane design it may become useful in wavelength switching systems.

This thesis has described my work in fabricating MTVSELs and frequency locking them to an external optical filter. Chapter 2 covers the basic laser theory needed to under-

stand the design of the MTVCSSEL. Chapter 3 reviews the design of the membrane tunable VCSELs. Chapter 4 describes the extensive work on fabrication needed to create MTVCSSELs including measurements and modeling of the oxidation rate in $\text{Al}_{0.97}\text{Ga}_{0.03}\text{As}$ layers and the development of controlled stress PECVD Silicon Nitride and Silicon Dioxide films. Chapter 5 presents the results of measurements on the operating MTVCSSELs including the first measurements of their lasing linewidth which was 2 GHz. The lasers had a threshold current of 0.45 mA, an SMSR of 25 dB, and tuned over a 17 nm range. Chapter 6 discusses the application of frequency locked loops to MTVCSSELs and WDM systems. The FLL system demonstrated frequency locking and tracking over an 11 nm range.

7.2 Future Work

There are many companies trying to commercialize some of the different approaches to tunable lasers and there is a large amount of research activity in this area now, but there are a few ideas related to MTVCSSELs that have not been well studied.

7.2.1 Membrane Design

The design of micromachined membranes has been improved through a variety of approaches, including a couple of designs that enable a larger range of motion before membrane collapses [119,120]. However a design is needed that increases both rate and range of tuning while remaining easy to fabricate. A possible solution is the build the membrane in a silicon micromachining process and then wafer bond or solder bump bond the membrane mirror to a VCSEL without a top mirror. This design would allow for much more flexibility in the design of the optical layers. Additionally if the membrane was situated between the Silicon wafer and the GaAs wafer it may possible to drive the membrane in both directions with a voltage. That design decouples the membrane stiffness from the tuning rate.

7.2.2 Alternative Wavelengths

The recent success of growing GaInNAs on GaAs for long wavelength devices opens up the 1.3 micron band for device development. The characteristics of quantum wells formed out of GaInNAs are still being researched, so the project may present some challenges, but the same process as used here in fabricating 980 nm devices can be utilized since the same type of GaAs substrates will be used. To get to wavelengths longer than the 1.3 micron band, the materials systems that can be grown on InP substrates are needed. The use of InP based materials would require the development of a new fabrication process for MTVCSSELs. In particular there is no good high Al content layer that can be easily oxidized for current confinement, although a few ideas have been tested [122,124]. In fact in the InP materials system the best VCSEL results have been obtained by using current confinement apertures that are defined by selective wet etching [125].

7.2.3 Systems Demonstrations

The ability to fabricate a wafer of reliable devices will enable further systems demonstrations. Frequency locking is just a first important step down the road to an optically routed WDM system. This works development of controlled membrane stress and robust oxidation apertures has enabled the reliable fabrication of MTVCSSELs. The device needs to be slightly redesigned to allow for the wire bonding and packaging needed to utilize multiple devices in the same system. Presently each device has to be probed individually which prevents the fabrication of a multichannel system. Such a system would enable the further study of FLL electronics systems including their influence on the lasers behavior and their impact on performance of a WDM system.

7.2.4 Reliability

The electronic reliability of the laser should be similar to other intracavity contacted 980 nm lasers. The use of intracavity contacts and the VCSEL structure makes the problem slightly harder than the standard edge-emitting 980 nm laser. However, the real

challenge lies in the reliability of the micromachined membrane. Little has been published on the reliability of micromachined devices, but some the research so far suggests that there is a lot of work to do [126,127]. The primary result is that polycrystalline materials under stress exhibit creep. This will change the tension in the membrane and can cause the mirror to tilt or deform which would disturb the lasing mode or prevent lasing altogether. For increased reliability it is desirable to form the membrane legs out of single crystal material and to deposit polycrystalline material selectively as needed to form high reflectivity DBRs.

Bibliography

- [1] G. Moore, "Progress in Digital Integrated Electronics," *International Electron Devices Meeting*, Washington, DC, pp. 11-12, 1975.
- [2] Semiconductor Industry Association, *The National Technology Roadmap for Semiconductors: Technology Needs*, 1997 Edition, Semitech INC., 1997, see also <http://www.semichips.org/>
- [3] J. Bowers, UCSB.
- [4] G. Gilder, "The Intel of the Telecom," Gilder Technology Report, vol. 3, no. 5, May 1998, <http://www.gildertech.com>.
- [5] Currently 10 Gbs electronics systems are standardized and available for optical transmission. 40 Gbs systems are in development and standardization.
- [6] M. S. Borella, J. P. Jue, D. Banerjee, B. Ramamurthy, and B. Mukherjee, "Optical Components for WDM Lightwave Networks," *Proceedings of the IEEE*, vol. 85, no. 8, pp. 1274-1307, August 1997
- [7] M. C. Larson, *Microelectromechanical Wavelength-Tunable Vertical-Cavity Light-Emitters and Lasers*, Ph.D. Dissertation, Stanford University, May 1996.
- [8] F. J. Sugihwo, *Design and Fabrication of Wavelength Tunable Optoelectronic Devices*, Ph.D. Dissertation, Stanford University, August 1998.

- [9] V. Jayaraman, Z.-M. Chuang, and L. A. Coldren, "Theory, Design, and Performance of Extended Tuning Range Semiconductor Lasers with Sampled Gratings," *IEEE Journal of Quantum Electronics*, vol. 29, no. 6, pp. 1824-1834, June 1993.
- [10] H. Ishii, F. Kano, Y. Yoshikuni, H. Yasaka, "Mode stabilization method for superstructure-grating DBR lasers," *Journal of Lightwave Electronics*, vol. 6, no. 3, pp. 433 -442. March 1998.
- [11] M. G. Peters, D. B. Young, F. H. Peters, J. W. Scott, B. J. Thibeault, and L. A. Coldren, "17.3% peak wall plug efficiency vertical-cavity surface-emitting lasers using lower barrier mirrors," *Photonics Technology Letters*, vol. 6, no. 1, pp. 31-33. January 1994.
- [12] E. R. Hegblom, N. M. Margalit, A. Fiore, L.A. Coldren, "High-performance small vertical-cavity lasers: a comparison of measured improvements in optical and current confinement in devices using tapered apertures," *Journal of Selected Topics in Quantum Electronics*, vol. 5, no. 3, pp. 553-560. May/June 1999.
- [13] Y. Inoue, A. Kaneko, F. Hanaw, H. Takahashi, K. Hattori, "A thermal silica-based arrayed-waveguide grating (AWG) multiplexer," *11th International Conference on Integrated Optics and Optical Fibre Communications 23 European Conference on Optical Communications*, Edinburgh, UK, vol. 5, p. 33-36, 1997.
- [14] C. Fabry and A. Perot, "Theorie et applications d'une nouvelle method de spectroscopie interferentielle," *Ann. Chim. Phys.* vol. 16, pp. 115-144, 1899.
- [15] A. E. Siegman, *Lasers*, University Science Books, Mill Valley, California, 1986.
- [16] S. Adachi, "Materials parameters for use in research and device applications," *Journal of Applied Physics*, vol. 58, pp. R1-R29, 1 August 1985.
- [17] J. Talghader and J. S. Smith, "Thermal Dependence of the Refractive Index of GaAs and AlAs Measured Using Semiconductor Multilayer Optical Cavities," *Applied Physics Letters*, vol. 66, no. 3, pp. 335-337, 16 January 1995.
- [18] S. M. Lord, *Growth of High In content InGaAs on GaAs substrates for Optical Applications*, Ph.D. dissertation, Stanford University, June 1993.
- [19] J. W. Matthews and A.E. Blakeslee, "Defects in Epitaxial Multilayers 1. Misfit Dislocations," *Journal of Crystal Growth*, vol. 27, p. 118. 1974.

- [20] H. Kroemer, "Semiconductor heterojunctions at the Conference on the Physics and Chemistry of Semiconductor Interfaces: A device physicist's perspective," *Journal of Vacuum Science and Technology*, vol. 11, no. 4, pp. 1354-1361, July/August 1993.
- [21] J. Singh, *Physics of Semiconductors and their Heterostructures*, McGraw-Hill, Boston, 1993.
- [22] R. F. Kopf, M. H. Herman, M. L. Schones, C. Colvard, "Band offset determination in parabolic and triangular quantum wells of GaAs/AlGaAs and GaInAs/AlInAs," *Journal of Vacuum Science and Technology B*, vol. 11, no. 3, pp. 813-816, May/June 1993.
- [23] L. A. Coldren and S. W. Corzine, *Diode Lasers and Photonic Integrated Circuits*, John Wiley & Sons, 1995.
- [24] C Kittel, H. Kroemer, *Thermal Physics*, W. H. Freeman, New York, 1980.
- [25] B. E. A. Saleh and M. C. Teich, *Fundamentals of Photonics*, John Wiley & Sons, New York, 1991
- [26] M. A. Afromowitz, "Refractive Index of $\text{Ga}_{1-x}\text{Al}_x\text{As}$," *Solid State Communications*, vol. 15, pp. 59-63. 1974.
- [27] H. Soda, K. Iga, C. Kitahara, and Y. Suematsu, "GaInAsP/InP Surface Emitting Injection Lasers," *Japanese Journal of Applied Physics*, vol. 18, no. 12, pp. 2329-2330, December 1979.
- [28] J. L. Jewell, J. P. Harbison, A. Scherer, Y. H. Lee, and L. T. Florez, "Vertical-Cavity Surface-Emitting Lasers: Design, Growth, Fabrication, Characterization," *IEEE Journal of Quantum Electronics*, vol. 27, no. 6, pp. 1332-1346, June 1991.
- [29] S. W. Corzine, R. S. Geels, J. W. Scott, R. H. Yan, and L. Coldren, "Design of Fabry-Perot Surface-Emitting Lasers with a Periodic Gain Structure," *IEEE Journal of Quantum Electronics*, vol. 25, no. 6, pp. 1513-1524, June 1989.
- [30] L. A. Coldren, E. Hegblom, E. Strzelecka, J. Ko, Y. Alulova, and B. Thibeault, "Recent advances and important issues in vertical-cavity lasers," *Proceedings of the SPIE*, vol. 3003, p. 2-12, 1997.
- [31] H. A. MacLeod, *Thin Film Optical Filters*, Macmillan, New York, 1986.
- [32] D. K. Cheng, *Field and Wave Electromagnetics*, Addison-Wesley, Reading, Massachusetts, 1990.

- [33] K. L. Bacher, *Improvements Toward High-Efficiency Vertical-Cavity Surface-Emitting Lasers*, Ph.D. Dissertation, Stanford University, June 1995.
- [34] D. I. Babic, and S. W. Corzine, "Analytic Expressions for the Reflection Delay, Penetration Depth, and Absorptance of Quarter-Wave Dielectric Mirrors," *IEEE Journal of Quantum Electronics*, vol. 28, no. 2, pp. 514-524, February 1992.
- [35] G. T. A. Kovacs, *Micromachined Transducers Sourcebook*, McGraw-Hill, Boston, 1998 and references therein.
- [36] Dr. E. K. L. Chan, personal communication.
- [37] FSM instruments, *Stress Gauge Manual*, 1993.
- [38] B. Pezeshki and J. S. Harris, Jr., U.S. Patent 5 291 502, September 4, 1992.
- [39] M. C. Larson and J. S. Harris, Jr., "Wide and continuous wavelength tuning in a vertical cavity surface emitting laser using a micromachined deformable membrane mirror," *Applied Physics Letters*, vol. 68, no. 7, pp. 893-3, 12 February 1996.
- [40] D. Vakhshoori, P. Tayebati, Chih-Cheng Lu, M. Azimi, P. Wang, Jain-Huai Shou, and E. Canoglu, "2mW CW singlemode operation of a tunable 1550 nm vertical cavity surface emitting laser with 50 nm tuning range," *Electronics Letters*, vol. 35, no. 11, pp. 900-901, 27 May 1999.
- [41] M. C. Larson, B. Pezeshki, and J. S. Harris, Jr., "Vertical Coupled-Cavity Microinterferometer on GaAs with Deformable-Membrane Top Mirror," *IEEE Photonics Technology Letters*, vol. 7, no. 4, pp. 382-384, April 1995.
- [42] M. C. Larson and J. S. Harris, Jr., "Broadly-Tunable Resonant-Cavity Light-Emitting Diode," *IEEE Photonics Technology Letters*, vol. 7, no. 11, pp. 1267-1269, November 1995.
- [43] F. Sugihwo, M. C. Larson, and J. S. Harris, Jr., "Simultaneous Optimization of Membrane Reflectance and Tuning Voltage for Tunable Vertical Cavity Lasers," *Applied Physics Letters*, vol. 72, no. 1, pp. 10-12, January 1998.
- [44] Fabrication experiment conducted by C. C. Lin and myself.
- [45] The reflection off of the air/substrate interface and the backside of the bottom DBR forms an etalon. The etalon can significantly alter the effective reflectivity that the laser sees from the bottom DBR and has a free spectral range of ~ 0.5 nm.
- [46] Prof. J. McVittie, personal communication.

- [47] Recipe courtesy of Dr. F. Sugihwo.
- [48] K. D. Choquette, K. M. Geib, C. I. H. Ashby, R. D. Twesten, O. Blum, H. Q. Hou, D. M. Follstaedt, B. E. Hammons, D. Mathes, and R. Hull, "Advances in Selective Wet Oxidation of AlGaAs Alloys," *IEEE Journal of Selected Topics in Quantum Electronics*, vol. 3, no. 3, pp. 916-26, June 1997.
- [49] J. M. Dallesasse, N. Holonyak, Jr., A. R. Sugg, T. A. Richard, and N. El-Zein, "Stability of AlAs in AlGaAs-AlAs-GaAs quantum well heterostructures," *Applied Physics Letters*, vol. 56, no. 24, pp. 2436-38, 1990.
- [50] J. M. Dallesasse, N. Holonyak, Jr., A. R. Sugg, T. A. Richard, and N. El-Zein, "Hydrolyzation Oxidation of $\text{Al}_x\text{Ga}_{1-x}\text{As}$ -AlAs-GaAs Quantum Well Heterostructure and Superlattices," *Applied Physics Letters*, vol. 57, no. 26, pp. 2844-2846, December 1990.
- [51] A. R. Sugg, N. Holonyak, Jr., J. E. Baker, F. A. Kish, and J. M. Dallesasse, "Native Oxide Stabilization of AlAs-GaAs Heterostructure," *Applied Physics Letters*, vol. 58, no. 11, pp. 1199-1201, March 1991.
- [52] J. M. Dallesasse and N. Holonyak, Jr. "Native-Oxide Stripe-Geometry $\text{Al}_x\text{Ga}_{1-x}\text{As}$ -GaAs Quantum Well Heterostructure Lasers," *Applied Physics Letters*, vol. 58, no. 4, pp. 394-396, January 1991.
- [53] D. L. Huffaker, D. G. Deppe, K. Kumar, and T. J. Rogers, "Native-Oxide Defined Ring Contact for Low Threshold Vertical-Cavity Lasers," *Applied Physics Letters*, vol. 65, no. 1, pp. 97-99, July 1994.
- [54] R. D. Twesten, D. M. Follstaedt, K. D. Choquette, and R. P. Schneider, Jr., "Microstructure of Laterally Oxidized $\text{Al}_x\text{Ga}_{1-x}\text{As}$ Layers in Vertical-Cavity Lasers," *Applied Physics Letters*, vol. 69, no. 1, pp. 19-21, July 1996.
- [55] K. L. Lear, S. P. Kilcoyne, R. P. Schneider, Jr., and J. A. Nevers, "Life-Testing Oxide Confined VCSELs: Too Good to Lost?," *Proceedings of the SPIE*, vol. 2683, pp. 114-122, 1996.
- [56] J. A. Kash, B. Pezeshki, F. Agahi, and N. A. Bojarczuk., "Recombination in GaAs at the AlAs Oxide-GaAs Interface," *Applied Physics Letters*, vol. 67, no. 14, pp. 2022-2024, October 1995.
- [57] F. A. Kish, S. A. Maranowski, G. E. Hofler, N. Holonyak, Jr., S. J. Caracci, J. M. Dallesasse, and K. C. Hsieh, "Dependence on Doping Type (P/N) of the Water Vapor Oxidation of High-Gap $\text{Al}_x\text{Ga}_{1-x}\text{As}$," *Applied Physics Letters*, vol. 60, no. 25, pp. 3165-67, June 1992.

- [58] K. J. Knopp, R. P. Mirin, D. H. Christensen, K. A. Bertness, and A. Roshko, "Optical Constants of $(\text{Al}_{0.98}\text{Ga}_{0.02})_x\text{O}_y$ native oxides," *Applied Physics Letters*, vol. 73, no. 24, pp. 3512-3514, 14 December 1998.
- [59] B. Weigl, M. Grabherr, C. Jung, R. Jager, G. Reiner, R. Michalzik, D. Sowada, K. J. Ebling, "High-Performance Oxide-Confined GaAs VCSEL's," *IEEE Journal of Selected Topics in Quantum Electronics*, vol. 3, no. 2, pp. 409-14, April 1997.
- [60] A. R. Massengale, *Collector up AlGaAs/GaAs heterojunction bipolar transistors using oxidized AlAs for current confinement*, Ph.D. Dissertation, Stanford University, 1998.
- [61] R. L. Naone, and L. A. Coldren, "Surface energy model for the thickness dependence of the lateral oxidation of AlAs," *Journal of Applied Physics*, vol. 82, no. 5, pp. 2277-80, 1 September 1997.
- [62] B. E. Deal and A. S. Grove, "General Relationship for the Thermal Oxidation of Silicon," *Journal of Applied Physics*, vol. 36, no. 12, pp. 3770-3778, December 1965.
- [63] C. I. Ashby, M. M. Bridges, A. A. Allerman, B. E. Hammons, and H. Q. Hou, "Origin of the time dependence of wet oxidation of AlGaAs," *Applied Physics Letters*, vol. 75, no. 1, pp. 73-75, 5 July 1999.
- [64] K. D. Choquette, K. M. Geib, H. C. Chui, B. E. Hammons, H. Q. Hou, and T. J. Drummond, "Selective Oxidation of Buried AlGaAs versus AlAs Layers," *Applied Physics Letters*, vol. 69, no. 10, pp. 1385-1387, September 1996.
- [65] D. B. Kao, J. P. McVittie, W. D. Nix, and K. C. Saraswat, "Two-Dimensional Silicon Oxidation Experiments and Theory," *IEDM Technical Digest*, Paper 14.6, pp. 388-391, 1985.
- [66] Graham Wheeler, STS engineer, personal communication
- [67] T. Flannery, C. Storum, E. Sigari, STS users, personal communication
- [68] D. L. Smith, A. S. Alimonda, C-C Chen, S. E. Ready, and B. Wacker, "Mechanism of SiNH Deposition from $\text{NH}_3\text{-SiH}_4$ Plasma," *Journal of the Electrochemical Society*, vol. 137, no. 2, pp.614-23, February 1990.
- [69] W. A. P. Claassen, W. G. J. N. Valkenburg, M. F. C. Willemsen, and W. M. v. d. Wijgert, "Influence of Deposition Temperature, Gas pressure, Gas Phase Composition, and RF Frequency on Composition and Mechanical Stress of Plasma Silicon Nitride Layers," *Journal of the Electrochemical Society*, vol. 132, no. 4, pp. 893-898, 1985.

- [70] W. A. Pliskin, "Comparison of properties of dielectric films deposited by various methods," *Journal of Vacuum Science and Technology*, vol. 14, no. 5, September/October 1977, pp 1064-1081.
- [71] A. Stoffel, A. Kovacs, W. Kronast, and B. Muller, "LPCVD against PECVD for micromechanical applications," *Journal of Micromechanics and Microengineering*," vol. 6, no. 1, 1996, pp. 1-13.
- [72] C. Charles, and R. W. Boswell, "Stress reduction in silicon dioxide layers by pulsing an oxygen/silane helicon diffusion plasma," *Journal of Applied Physics*, vol. 84, no.1, pp. 350-4, 1 July 1998.
- [73] D. Poitras, P. Leroux, J. E. Klemberg-Sapieha, S. C. Gujrathi, L. Martinu, "Characterization of homogeneous and inhomogeneous Si-Based optical coatings deposited in dual-frequency plasma," *Optical Engineering*, vol. 35, no. 9, pp. 2693-9, September 1996.
- [74] L. A. Coldren, B. J. Thibeault, E. R. Hegbloom, G. B. Thompson, and J. W. Scott, "Dielectric apertures as intracavity lenses in vertical-cavity laser," *Applied Physics Letters*, vol. 68, no. 3, pp. 313-315, 15 January 1996.
- [75] E. R. Hegbloom, D. I. Babic, B. J. Thibeault, L. A. Coldren, "Scattering Losses from Dielectric Apertures in Vertical-Cavity Lasers," *IEEE Journal of Selected Topics in Quantum Electronics*, vol. 3, no. 2, pp. 379-389, April 1997.
- [76] B. Demeulaenaere, P. Bienstman, B. Dhoedt, and R. G. Baets, "Detailed Study of AlAs-Oxidized Apertures in VCSEL Cavities for Optimized Modal Performance," *IEEE Journal of Quantum Electronics*, vol. 35, no. 3, pp. 358-367, March 1999.
- [77] A. E. Bond, P. D. Dapkus, J. D. O'Brien, "Aperture Placement Effects in Oxidized Defined Vertical-Cavity Surface-Emitting Lasers," *Photonics Technology Letters*, vol. 10, no. 10, pp. 13621-1364, October 1998.
- [78] P. A. Roos, J. L. Carlsten, D. C. Kilper, K. L. Lear, "Diffraction from oxide confinement apertures in vertical-cavity lasers," *Applied Physics Letters*, vol. 75, no. 6, pp. 754-756, 9 August 1999.
- [79] B. J. Thibeault, E. R. Hegblom, P. D. Floyd, R. Naone, Y. Akulova, and L. A. Coldren, "Reduced Optical Scattering Loss in Vertical-Cavity Lasers using a Thin (300Å) Oxide Aperture," *IEEE Photonics Technology Letters*, vol. 8, no. 5, pp. 593-595, May 1996.

- [80] B. J. Thibeault, K. Bertilsson, E. R. Hegblom, E. Strzelecka, P. D. Floyd, R. Naone, and L. A. Coldren, "High Speed Characteristics of Low-Optical Loss Oxide Apertured Vertical-Cavity Lasers," *IEEE Photonics Technology Letters*, vol. 9, no. 1, pp. 11-13, May 1996.
- [81] R. L. Naone and L. A. Coldren, "Tapered Air Apertures for Thermally Robust VCL Structures," *IEEE Photonics Technology Letters*, vol. 11, no. 11, pp. 1339-1341, November 1996.
- [82] E. R. Hegblom, R. L. Naone, N. M. Margalit, and L. A. Coldren, "Comparison of Tapered Apertures in Vertical Cavity Lasers," *Proceedings of LEOS 1997*, vol. 2, pp. 350-351, November 1997.
- [83] R. L. Naone, E. R. Hegblom, B. J. Thibeault, and L. A. Coldren, "Oxidation of AlGaAs layers for tapered apertures in vertical-cavity lasers," *Electronics Letters*, vol. 33, no. 4, pp. 300-301, 13 February 1997.
- [84] E. R. Hegblom, B. J. Thibeault, R. L. Naone, and L. A. Coldren, "Vertical cavity lasers with tapered apertures for low scattering loss," *Electronics Letters*, vol. 33, no. 10, pp. 869-870, 8 May 1997.
- [85] K. L. Lear, K. D. Choquette, R. P. Schneider, Jr., S. P. Kilcoyne, and K. M. Geib, "Selectively Oxidized Vertical Cavity Surface Emitting Lasers with 50% Power Conversion Efficiency," *Electronics Letters*, vol. 31, no. 3, pp. 208-209, February 1995.
- [86] K. D. Choquette, W. W. Chow, G. R. Hadley, H. Q. Hou, and K. M. Geib, "Scalability of Small-Aperture Selectively Oxidized Vertical Cavity Lasers," *Applied Physics Letters*, vol. 70, no. 7, pp. 823-825, February 1997.
- [87] E. R. Hegblom, D. I. Babic, B. J. Thibeault, and L. A. Coldren, "Estimation of Scattering Losses in Dielectrically Apertured Vertical Cavity Lasers," *Applied Physics Letters*, vol. 68, no. 13, pp. 1757-1759, March 1996.
- [88] E. R. Hegblom, N. M. Margalit, B. J. Thibeault, L. A. Coldren, and J. E. Bowers, "Current Spreading in Apertured Vertical Cavity Lasers," *Proceedings of the SPIE*, vol. 3003, pp. 176-180, 1997.
- [89] C. H. Henry, "Theory of Linewidth of Semiconductor Lasers," *IEEE Journal of Quantum Electronics*, vol. 18, no. 2, pp. 259-264, February 1982.
- [90] B. Moller, E. Zeeb, U. Fiedler, T. Hackbarth, and K. J. Ebeling, "Linewidth Enhancement Factor of Vertical-Cavity Surface-Emitting Laser Diodes," *IEEE Photonics Technology Letters*, vol. 6, no. 8, pp. 921-923, August 1994.

- [91] C. H. Henry, "Phase Noise in Semiconductor Lasers," *Journal of Lightwave Technology*, vol. 4, no.3, pp. 298-311, March 1986.
- [92] C. H. Henry, "Theory of Spontaneous Emission Noise in Open Resonators and its Application to Lasers and Optical Amplifiers," *Journal of Lightwave Technology*, vol. 4, no.3, pp. 288-297, March 1986.
- [93] C. H. Henry, "Theory of the Phase Noise and Power Spectrum of a Single Mode Injection Laser," *IEEE Journal of Quantum Electronics*, vol. 19, no. 9, pp. 1391-1397, September 1983.
- [94] L. Goldberg, H. F. Taylor, A. Dandridge, J. F. Weller, R. O. Miles, "Spectral Characteristics of Semiconductor Lasers with Optical Feedback," *IEEE Transactions on Microwave Theory and Techniques*, vol. 30, no. 4, pp. 401-409, April 1982.
- [95] M. Yamanishi, Y. Lee, "Phase Dampings of Optical Dipole Moments and Gain Spectra in Semiconductor Lasers," *IEEE Journal of Quantum Electronics*, vol. 23, no. 4, pp. 367-370, April 1987.
- [96] J. A. Armstrong, "Theory of Interferometric Analysis of Laser Phase Noise," *Journal of the Optical Society of America*, vol. 56, no. 8, pp. 1024-1031, August 1966.
- [97] F. Koyama, K. Morito, and K. Iga, "Intensity Noise and Polarization Stability of GaAlAs-GaAs Surface Emitting Lasers," *IEEE Journal of Quantum Electronics*, vol. 27, no. 6, pp. 1410-1416, June 1991.
- [98] T. Ohtoshi, N. Chinone, "Linewidth Enhancement Factor in Strained Quantum Well Lasers," *Photonics Technology Letters*, vol. 1, no. 6, pp. 117-119, June 1989.
- [99] S. Turley, "Exploring the New Communications Landscape," *Photonics Spectra*, pp. 152-157, March 1998.
- [100] J. C. Chen, and C Dragone, "A Proposed Design for Ultralow-Low Waveguide Grating Routers," *Photonics Technology*, vol. 10, no. 3, pp. 379-381, March 1998.
- [101] H. Takahashi, K. Oda, H. Toba, Y. Inoue, "Transmission Characteristics of Arrayed Waveguide N x N Waveguide Multiplexer," *Journal of Lightwave Technology*, vol. 13, no. 3, pp. 447-455, March 1995.
- [102] K. Okamoto, K. Syuto, H. Takahashi, and Y. Ohmori, "Fabrication of 128-channel arrayed-waveguide grating multiplexer with 25 GHz channel spacing," *Electronics Letters*, vol. 32, no. 16, pp. 1474-1475, 1 August 1996.

- [103] S. Suzuki, "Recent progress on silica-based planar lightwave circuits," *Proceedings of the SPIE*, vol. 3666, pp. 122-131, 1999.
- [104] I. M. Horowitz, J. W. Smay, and A. Shapiro, "A Synthesis Theory for the Externally Excited Adaptive System (EEAS)," *IEEE Transactions on Automatic Control*, vol. 19, no. 2, pp. 101-107, April 1974.
- [105] I. M. Horowitz, J. W. Smay, and A. Shapiro, "A Synthesis Theory for Self-Oscillating Adaptive Systems (SOAS)," *Automatica*, vol. 10, pp. 381-392, 1974.
- [106] I. M. Horowitz, and A. Shapiro, "A synthesis theory for multiple-loop oscillating adaptive systems," *International Journal of Control*, vol. 29, no. 6, pp. 963-979, 1979.
- [107] O. Yaniv, I. M. Horowitz, and S. Oldak, "Disturbance attenuation in single-loop oscillating dithered adaptive systems," *International Journal of Control*, vol. 48, no. 1, pp. 179-192, 1988.
- [108] I. M. Horowitz, S. Oldak, and A. Shapiro, "Extensions of dithered feedback systems," *International Journal of Control*, vol. 54, no. 1, pp. 83-109, 1991.
- [109] Prof. T. H. Lee, personal communication
- [110] T H. Lee, *The Design of CMOS Radio Frequency Integrated Circuits*, Cambridge University Press, Cambridge, UK, 1998.
- [111] A. Gelb, W. E. Vander, *Multiple-Input Describing Functions and Nonlinear System Design*, McGraw-Hill, New York, 1968.
- [112] Fred Sugihwo, Michael Larson, Chien-chung Lin, Wayne Martin, James S. Harris, Jr., "Micromachined Tunable Vertical Cavity Laser with a 25nm Wavelength Tuning Range," 55th Annual Device Research Conference Digest, pages 108-9, Fort Collins, CO, 23-25 June 1997.
- [113] James S. Harris, Jr., Chien-chung Lin, Wayne Martin, Fred Sugihwo, Michael Larson, Barbara Paldus, "Micromachined Optoelectronics Devices for Spectroscopic Applications," *Advanced Semiconductor Lasers and Their Applications*, Santa Barbara, California, 21-23 July 1999.
- [114] James S. Harris, Jr., Chien-chung Lin, Wayne Martin, Fred Sugihwo, Michael Larson, Barbara Paldus, "Micromachined Optoelectronics Devices for Spectroscopic Applications," *OSA Trends in Optics and Photonics Vol. 31, Advanced Semiconductor Lasers and Their Applications*, Leo Hollberg and Robert J. Lang eds. (Optical Society of America, Washington, DC 2000) pp.130-134.

- [115] Wayne Martin, Fred Sugihwo, James S. Harris, Jr., "Frequency Locking of a Micromachined Tunable VCSEL for WDM Optical Interconnects," OSA Annual Meeting / ILS-XIII, Long Beach, California, 12-17 October 1997.
- [116] Wayne Martin, Chien-chung Lin, Fred Sugihwo, James S. Harris, Jr., "Frequency Locking of Micromachined Tunable VCSELs to External Wavelength Selective Filters," IEEE/LEOS Summer Topical Meeting, Aventura, Florida, 24-28 July 2000
- [117] Chien-chung Lin, Wayne A. Martin, James S. Harris, Jr., and Edward Chan, "A New Al₂O₃/GaAs Deformable Mirror for Tunable Optoelectronic Devices," IMECE MEMS Symposium, Orlando, Florida, 5-10 November 2000.
- [118] Chien-chung Lin, Wayne A. Martin, James S. Harris, Jr., "Modeling of MEMS Tunable Optoelectronic Device Mirror," IEEE/LEOS Conference on Optical MEMS, Kauai, Hawaii, 21 - 24 August 2000.
- [119] E. K. L. Chan, *Characterization and modeling of electrostatically actuated polysilicon micromechanical devices*, Ph.D. Dissertation, Stanford University, 2000.
- [120] C. J. Chang-Hasnain, "Tunable VCSEL," IEEE Journal of Selected Topics in Quantum Electronics, vol. 6 no. 6, pp. 978-987, November/December 2000.
- [121] J. M. Waite, C. F. R. Mateus, S. Chase, and C. J. Chang-Hasnain, "Torsional Micromechanical red-shifting tunable vertical cavity filter," Optical Society of America Annual Meeting, Providence, RI, October 2000.
- [122] H. Gebretsadik, K. Kamath, W. D. Zhou, P. Bhattacharya, C. Caneau, R. Bhat, "Lateral oxidation of InAlAs in InP-based heterostructures for long wavelength vertical cavity surface emitting laser applications," Applied Physics Letters, vol. 72, no. 2, pp. 135-137, 12 January 1998.
- [123] D. Pulver, C. W. Wilmsen, D. Niles, R. Kee, "Thermal Oxides of In_{0.5}Ga_{0.5}P and In_{0.5}Al_{0.5}P," Journal of Vacuum Science and Technology B, vol. 19, no. 1, pp. 207-214, January/February 2001.
- [124] B. Koley, F. G. Johnson, O. King, S. S. Saini, M. Dagenais, "A method of highly efficient hydrolyzation oxidation of III-V semiconductor lattice matched to indium phosphide," Applied Physics Letters, vol. 75, no. 9, pp. 1264-1266, 30 August 1999.

- [125] S. Nakagawa, E. Hall, G. Almuneau, J. K. Kim, D. A. Buell, H. Kroemer, and L. A. Coldren, "88°C, continuous-wave operation of apertured, intracavity contacted 1.55 μm vertical-cavity surface-emitting lasers," *Applied Physics Letters*, vol. 78, no. 10, pp. 1337-1339, 5 March 2001.
- [126] M. Hornung, O. Brand, O. Paul, and H. Baltes, "Long-term stability of membrane transducers for proximity sensing," *Proceedings of the SPIE*, vol. 3514, pp. 251-259, 1998.
- [127] A. M. Fitzgerald, R. H. Dauskardt, and T. W. Kenny, "Fracture Toughness and Crack Growth Phenomena of Plasma-Etched Single Crystal Silicon," *Sensors and Actuators: A*, vol. 83, no. 1-3, pp. 194-199, 2000.